

Contents

1	The human eye	5
1.1	Exercises	8
2	Celestial coordinate systems	9
2.1	Definitions	9
2.2	Altitude – azimuth	12
2.3	Some spherical trigonometry	13
2.4	Declination – hour angle	15
2.5	The standard geocentric celestial sphere	16
2.6	Right ascension and declination	16
2.7	The earth's orbit	17
2.8	Celestial latitude and longitude	19
2.9	Mean solar time	19
2.10	Sidereal time	20
2.11	Ephemeris and Universal time	22
2.12	Terrestrial Time and Barycentric Coordinate Time	22
2.13	The sidereal year and the tropical year	22
2.14	The Besselian year	23
2.15	The Julian date	23
2.16	The 3d dimension; distance	23
2.16.1	The astronomical unit	24
2.16.2	Stellar parallax	24
2.17	Exercises	25
3	Detectors	27
3.1	Detector parameters	27
3.2	Semiconductors	28
3.3	The photoelectric effect	30
3.4	CCDs	34
3.5	A simplified three-phase CCD lay-out	34
3.5.1	Other types of clocking	36
3.6	The surface channel MOS capacitor	37
3.7	The buried channel MOS capacitor	39
3.7.1	Potential well	40
3.7.2	Depletion	41
3.7.3	Storage capacity	43

3.8	The charge transfer process	44
3.9	Charge measurements	45
3.10	Dark currents	45
3.11	CCD summary, problems and corrections	47
3.12	Other types of detectors for visible light	47
3.12.1	Photomultipliers	47
3.12.2	Superconducting tunnel junction detectors (STJs)	48
3.12.3	Photovoltaic cells	48
3.12.4	Thermocouples	49
3.12.5	Phototransistors	49
3.13	Infrared detectors	49
3.13.1	Photoconductive cells	50
3.13.2	Bolometers	50
3.14	Noise	50
3.15	Exercises	51
4	Fourier analysis	53
4.1	Definitions	53
4.2	Properties	54
4.3	Sampling Theorem and Aliasing	55
4.4	FFTs	55
4.5	Exercises	57
5	Diffraction I	59
5.1	Helmholtz-Kirchhoff Integral	59
5.2	Diffraction by an aperture	61
5.3	Spreading of the wavefront	62
5.4	Fraunhofer diffraction	63
5.5	Diffraction of a single slit	63
5.6	Babinet's principle	64
5.7	Diffraction by a circular aperture	64
5.8	Exercises	65
6	Telescopes for visible light	67
6.1	Lenses, mirrors and geometric optics	67
6.1.1	Fermat's principle and Snell's law	68
6.1.2	Reflection and transmission coefficients	69
6.1.3	Reflection from a spherical surface	69
6.1.4	Refraction in lenses	70
6.1.5	Imaging properties	71
6.1.6	Simple telescopes	72
6.2	Optical Materials	73
6.3	Chromatic aberration	74
6.3.1	Schupmann achromat	75
6.4	Seidel Aberrations	77
6.4.1	Spherical aberration $\propto \rho^4$	78
6.4.2	Coma $\propto \rho^3 b \cos \phi$	79

CONTENTS	3
6.4.3 Astigmatism $\propto b^2 \rho^2 \cos^2 \phi$	79
6.4.4 Field curvature $\propto \rho^2 b^2$	80
6.4.5 Distortion $\propto \rho b^3 \cos \phi$	80
6.4.6 Zernike polynomials	80
6.5 Practical telescopes	82
6.5.1 Designs	84
6.5.2 Mountings	86
6.5.3 Telescopes in space	86
6.5.4 Observatory engineering	87
6.5.5 Future telescopes	88
6.6 Exercises	88
7 Diffraction II	89
7.1 Fresnel diffraction	89
7.2 Lunar occultation of a radio source	91
7.3 Circular Apertures	92
7.4 Seeing in the atmosphere	93
7.4.1 A simple model (with exercises)	93
7.4.2 Effects of the atmosphere (including better model)	93
7.4.3 Real time atmospheric compensation	95
7.5 Exercises	98
8 Radio, EUV and X-ray telescopes	101
8.1 Radio and microwave detection	101
8.2 Detectors and receivers	102
8.2.1 Heterodyne receiver	103
8.3 Radio telescopes	104
8.3.1 Spacecraft	107
8.3.2 Construction	107
8.4 X-ray and gamma-ray detection	107
8.4.1 Detectors	107
8.4.2 Imaging	111
8.4.3 Spectroscopy	113
9 Imaging	115
9.1 The inverse problem	115
9.1.1 De-convolution	115
9.2 Photography	117
9.3 Scanning	117
9.4 Interferometry	118
9.4.1 Michelson stellar interferometer	120
9.4.2 Michelson radio interferometer	122
9.4.3 Speckle interferometry	122

10 Spectroscopy	123
10.1 Diffraction gratings	123
10.1.1 Blazing	126
10.1.2 Shadowing	126
10.1.3 Rowland circle	126
10.1.4 Echelle gratings	127
10.1.5 Littrow spectroscopes	127
10.1.6 Ghosts and other anomalies	127
10.2 Prisms	127
10.3 Interferometers	128
10.3.1 Michelson interferometer	128
10.3.2 Fabry-Pérot interferometer	130
10.4 Exercises	134
11 Polarimetry	135
11.1 Stokes parameters	135
11.2 Optical components for polarimetry	136
11.2.1 Birefringence	137
11.2.2 Polarizers (or analysers)	137
11.2.3 Converters (retarders or phase plates)	138
11.2.4 Depolarizers	139
11.3 Polarimeters	139
11.4 Spectropolarimetry	139
11.5 Data reduction and analysis	139
11.6 Exercises	139
12 Photometry	141
12.1 A short history	141
12.2 The response function	142
12.2.1 Types of photometry	142
12.3 Magnitudes	143
12.3.1 Response function implementation	143
12.3.2 Response function description	144
12.3.3 Color indices	145
12.3.4 Line and feature index	146
12.4 Photometric systems	147
12.4.1 Common photometric systems	147
12.5 From source to telescope	148
12.5.1 Wavelength shifts	149
12.5.2 Absorption outside the atmosphere	150
12.5.3 Absorption by the atmosphere	150
12.6 Exercises	151

Chapter 1

The human eye

The human eye is not much in use as a professional tool of astronomy. On the other hand, it is of great interest to understand how it works and by doing so we may illustrate many of the principles and problems that we will meet later in the course.

Evolution has come up with different designs for eyes, but most (if not all) can be divided into two parts¹: *a lens*, or set of lenses, for focussing light onto a *receptor* which detects light and sends information of detection on to the brain or nervous system. There are many designs and materials used for the optical set up of the lens. For example trilobites, perhaps the first animals to develop eyes some 540 million years ago during the Cambrian, used lenses made of crystal, the mineral calcite. Calcite has many interesting optical properties, amongst which is the fact that they deflect light from all angles, except one privileged axis called the *c-axis*. Each eye facet in a trilobite had its own calcite lens directed so that light would pass in only one direction to the underlying retina. While there are many designs for lenses, all light detecting cells seem to be based on a single protein, or molecule, called *rhodopsin*, perhaps pointing to a common evolutionary source for all eyes extant throughout the animal kingdom².

The eye and brain work together, and the brain can correct for many of the aberrations suffered by the eye. Thus, for example, the brain compensates for the fact that the image on the retina is inverted, and for chromatic aberration.

Light is focussed on the retina, where there are two types of receptors: rods and cones. Cones for color reception, rods for black and white with higher sensitivity. For humans, rods and cones are arranged *backwards* so light must pass through the neuronal wires that send signals of light back to the brain. In contrast, octopus eyes, which otherwise are much as our own with a single lens in front and a light sensitive retina at the back, has the light sensitive parts of the retinal cells in front. This may be an accident of nature, or there may be good evolutionary reasons for the difference. Both designs are mimicked in CCD's used in astronomy, where *thinned, backlit* CCDs are used to avoid unwanted reflections from the electrodes used to drive them. The CCD in your camera or cell phone is more probably arranged in the same manner as your eye, with light having to pass through the electrodes lying on top of light sensitive doped silicon.

¹Some of the information here is gathered from the highly recommended book by Nick Lane *Life Ascending, the ten great inventions of evolution*, Richard Dawkins' *Climbing Mount Improbable* also contains a chapter on the evolution of the eye.

²Note that the design of light sensitive cells is roughly divided into two groups, where all the vertebrates share a similar design and the invertebrates another.

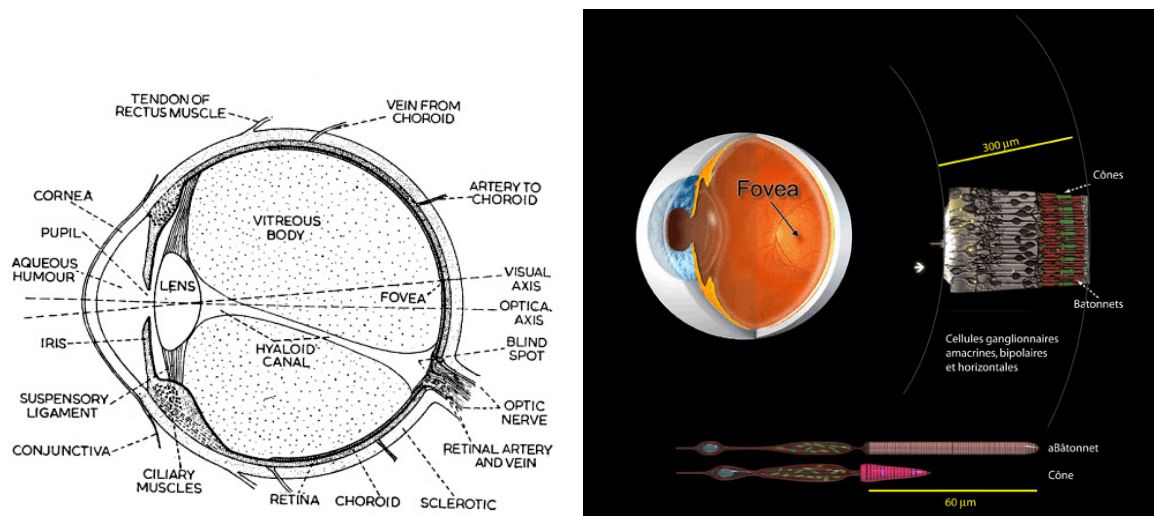


Figure 1.1: Cross section of the human eye (left), illustration of the eyes receptor cells; cones, used for color vision with the iodopsin layers arranged to the right, and rods with rhodopsin layers. Light enters these cells from the left before being absorbed by either iodopsin or rhodopsin.

In the rods a pigment known as rhodopsin absorbs radiation. A protein with a weight of some 40 000 amu, arranged in layers 20 nm thick and 500 nm wide. Under influence of light a small fragment, a chromophore, will split off. The chromophore is a vitamin A derivative called retinal (or retinaldehyde) with a molecular weight of 286 amu. The portion left behind is a colorless protein called opsin. The moment of visual excitation occurs during this break off process as the cell's electrical potential increases (for invertebrates on the other hand excitation occurs because the electrical charge across the membrane is removed). This change in potential can then propagate along nerve cells to the brain. The rhodopsin molecule is then (slowly) regenerated.

The response of cones is similar, but in this case the pigment is known as iodopsin which also contains the retinaldehyde group. Cone cells come in three varieties with different spectral sensitivities (see figure 1.2).

In bright light much of the rhodopsin is broken up into opsin and retinaldehyde, and the rod sensitivity is much reduced so that vision is primarily provided by the cones, even though their light sensitivity is only of order 1% of the rods. The three varieties of cones combine to give color vision. At low light levels only rods are triggered by the ambient radiation and vision is then in black and white.

Upon entering the dark from a brightly lit region rhodopsin will build up over a period of roughly 30 min, thus dark-adaptation takes this long and is based on rod cells. Somewhere between 1–10 photons are necessary to trigger an individual rod. However, several rods must be triggered in order to result in a pulse being sent to the brain, as many rods can be connected to a single nerve fibre. The total number of rods is of order 10^8 , of cones 6×10^6 , these must share some 10^6 nerve fibres. Thus there are roughly 100 visual receptors per nerve fibre, note that there can be many cross connections between groups of receptors. Cones are concentrated towards the fovea centralis, which is the region of most acute vision, while rods are most plentiful towards the periphery of the field of view. Weak objects are thus

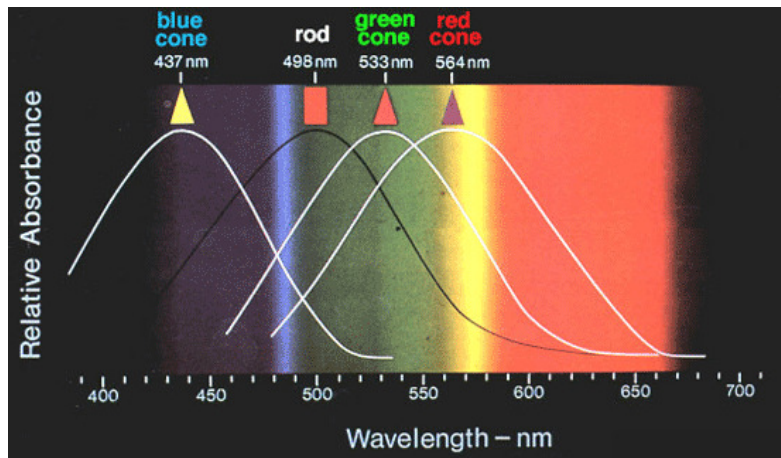


Figure 1.2: Absorption curves for the various types of cones, which combined give color vision, and for rhodopsin. Note that the peak sensitivity for rods (at 500 nm) and cones (at 555 nm) are at different wavelengths: this causes the sensitivity of the eye to shift towards blue at low light levels when the rods dominate.

most easily visible with averted vision, *ie* when it is not looked at directly. In sum with all these effects the eye is usable over a range of illuminations differing by a factor $10^9 - 10^{10}$. Note that in regions of high contrast the brighter region is often seen as too large, this is a phenomena known as *irradiation*. It arises from stimulated responses of unexcited receptors due to their cross connection with excited receptors. Eye fatigue occurs when staring fixedly at a source for an extended period due to depletion of the sensitive pigment.

The Rayleigh limit of the eye, roughly given by λ/D where λ is the wavelength of the observed light and D is the size of the observing aperture, is of order 20 arcsec when the iris has its maximum diameter of 5–7 mm. However, for two separate images to be distinguished, they must be separated by at least one unexcited receptor cell, so even on the fovea centralis resolution is limited in practice to between 1 arcmin and 2 arcmin. This is much better than elsewhere on the retina, since the fovea centralis is populated by small, tightly packed, singly connected cones. The average resolution of the eye lies between 5 arcmin and 10 arcmin for point sources. Linear sources such as an illuminated grating can be resolved down to 1 arcmin. The effect of granularity of the retina is countered by rapid oscillations of the eye through a few 10 arcsec with a frequency of a few Hz, so that several receptors are involved in the detection when averaged over time.

The response of the eye to changes in illumination is logarithmic; if two sources A and B are observed to differ by a given amount, and a third source C is seen to lie midway between them, then the energy from C will differ from A by the same factor as it differs from B . The faintest stars visible at a good site (magnitude 6^m) corresponds to a detection of approximately 3×10^{-15} W. Sensitivity will vary between individuals and decreases with age, the retina of a 60 year old person will receive some 30% of the light seen by a person of 30-years.

The system used by astronomers to measure the brightness of stars is a very old one, and is based on the sensitivity of the eye. Hipparchos' catalogue of stars divided the stars into six classes from the brightest, of the first rank or magnitude, to the dimmest of the sixth magnitude. The present day system is based on this after the work of Norman Pogson

put the magnitude scale on a firm basis in 1856. Pogson suggested a logarithmic scale that approximately agreed with earlier measurements: the difference between stars of magnitude m_1 and m_2 are given by

$$m_1 - m_2 = -2.5 \log \left(\frac{E_1}{E_2} \right)$$

where E_1 and E_2 are the energies per unit area at the surface of Earth for the two stars.

1.1 Exercises

1. What is the size, in kilometers, of the smallest crater that can be distinguished on the Moon with the naked eye (as seen from Earth)?
2. Vega has a magnitude of roughly 0.0, Polaris a magnitude of 2.0. Estimate the magnitudes of the stars in Orions belt as well as Betelgeuse, Rigel, and Bellatrix. What is the magnitude of the weakest star you can find in the sky?
3. Mizar and Alcor in Ursa Majoris are separated by some $11'$. Can you separate them and see both stars? Estimate their magnitudes as well. Mizar is itself a double star the components of which can be separated with a small telescope. Interestingly, all three stars are *spectroscopic binaries* as well, bringing the star total star count up to 6. The distance to these stars is some 83 ly while the distance between Mizar and Alcor is approximately 1 ly. All six stars are gravitationally bound and are members of the Ursa Major moving group.

Chapter 2

Celestial coordinate systems

In order to identify an object's position, one needs a system of coordinates. When the distance to the object is unknown, we can restrict ourselves to using two coordinates. On the other hand, since the Earth rotates around its own axis as well as around the Sun, the positions of stars and planets are continually changing. Hence, the measurement of *when* an object is in a certain place is as important as deciding *where* it is.

When setting up a coordinate system, one must first decide on the positions of the following:

1. The origin. *E.g.* one's own location, the center of the Earth, the center of the Solar System, the Galaxy, etc.
2. The fundamental plane ($x-y$ plane). This is often a plane of some physical significance such as the horizon, the equator, or the ecliptic.¹
3. Decide on the direction of the positive x -axis, also known as the “reference direction”.
4. And, finally, on a convention of signs of the $y-$ and $z-$ axes, *i.e* whether to use a left-handed or right-handed coordinate system.

For example Eratosthenes of Cyrene (c. 276 BC - c. 195 BC) was a Greek mathematician, elegiac poet, athlete, geographer, astronomer, and music theorist who invented a system of latitude and longitude. (According to Wikipedia he was also the first person to use the word *geography* and invented the discipline of geography as we understand it.). The origin of this coordinate system was the center of the Earth and the fundamental plane was the equator, which location Eratosthenes calculated relative to the parts of the Earth known to him.

In this text, we restrict ourselves to the use of spherical coordinates. We will generally differentiate between two types of coordinate systems: The **horizontal coordinate system** and the **equatorial coordinate system**. A big difference between these two types is the choice of the fundamental plane; respectively the horizon and the equator.

2.1 Definitions

When viewed from the surface of Earth, the sky above forms a hemisphere, and astronomical objects are seen to be projected onto this hemisphere. The hemisphere is part of the **celestial**

¹See later sections for definitions of these terms.

sphere. It is convenient to describe the location of the objects with two angular coordinates in the same manner as latitude and longitude are decided on the sphere of the earth. Note that the location of the origin of longitude for both the earth and the sky are not obvious. In any case, it is necessary to review a few aspects of trigonometry on a sphere in order to understand the use of these coordinate systems.

Any plane passing through the center of a sphere cuts the surface in a circle which is called a **great circle**. Any other plane that cuts the sphere, but that does not pass through the center is a **small circle**. When two great circles intersect at a point they are said to include a **spherical angle** which is defined between the tangents of the great circles at the point of their intersection. A spherical angle is only defined with respect to intersecting great circles. Given any three points on the surface of a sphere, the sphere can be bisected so that

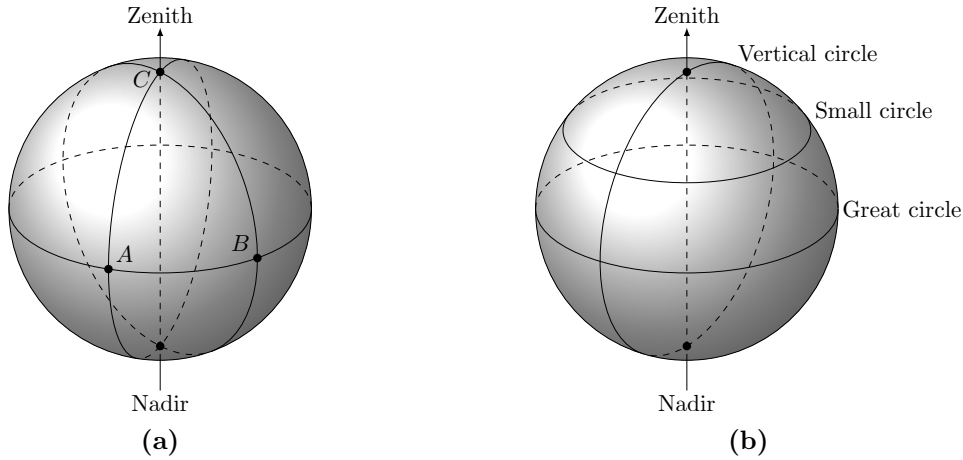


Figure 2.1: Figure (a) shows how three great circles can form a spherical triangle. Figure (b) illustrates some circle types.

all three points lie in the same hemisphere. Joining the points by great circle arcs all in this hemisphere defines a **spherical triangle**, as shown in Figure 2.1a. The length of a great circle arc is defined as the radius times the angle A formed between the two endpoints of the arc and the sphere's center measured in radians: $R \times A$. As discussed above there are several methods of specifying a given position on the celestial sphere, depending on which principal great circles are chosen as reference.

Let's get familiar with the celestial sphere. The choice of coordinate system depends on the choice of the fundamental plane. We first consider the horizontal coordinate system. We define the **zenith**, Z , to be the direction directly overhead, while the opposite direction is the **nadir**. The fundamental plane in this system is the horizon, and is the plane at a right angle to the zenith. The extended plane of the horizon that intersects the celestial sphere is the **celestial horizon**. The celestial horizon is then simply just an extension of Earth's horizon.

In the equatorial coordinate system, the equatorial plane is chosen as the fundamental plane. The extension of the plane of Earth's equator is the plane of the **celestial equator**, which intersects the celestial sphere. In this system, the z -axis is aligned with Earth's spin axis, i.e. the north pole (or south pole in the southern hemisphere). This axis intersects the celestial sphere in the **north celestial pole** and **south celestial pole**.

The angle ZP between the celestial horizon and the celestial equator is called the colatitude and depends on the observer's latitude ϕ . It's easy to see that the colatitude is then

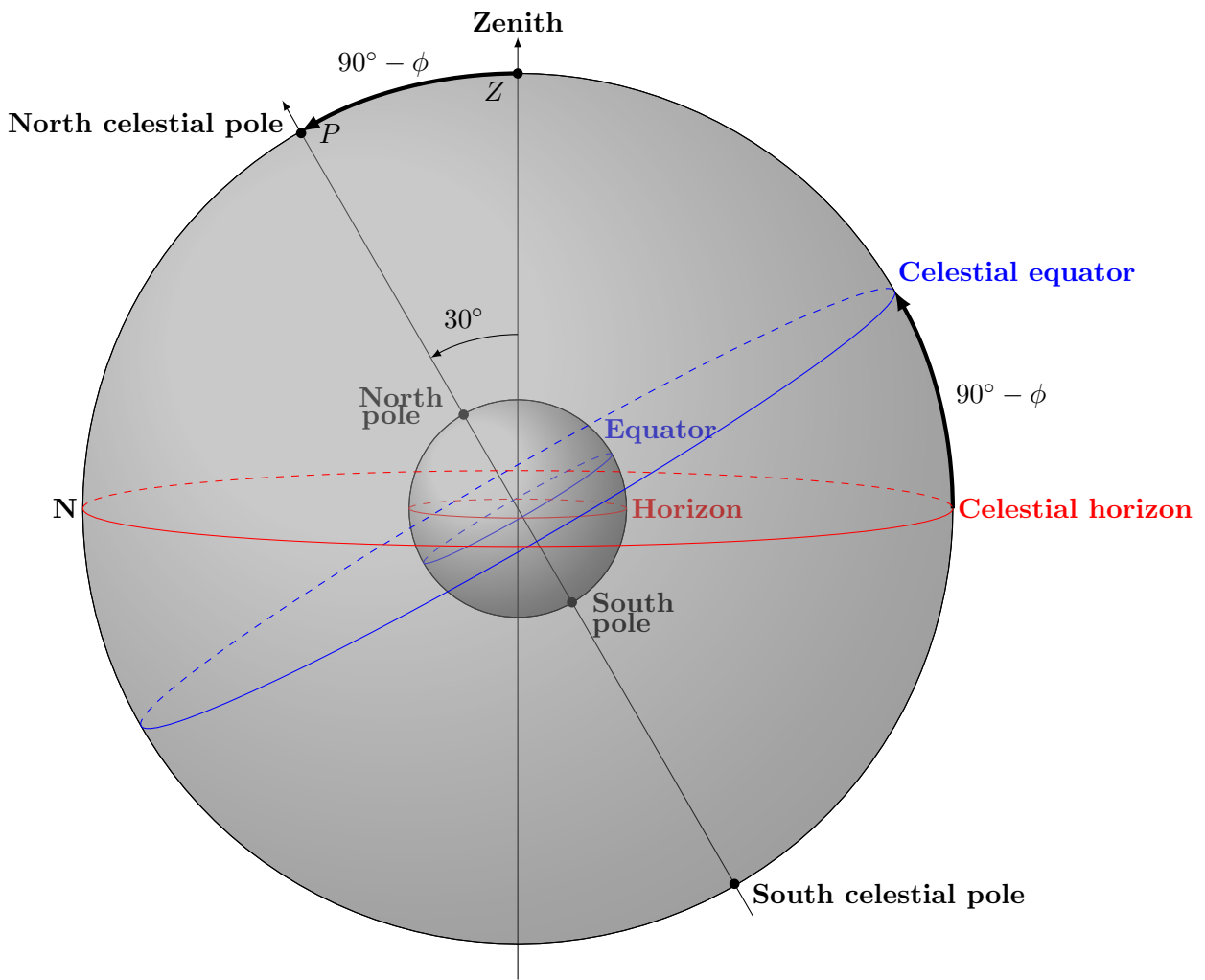


Figure 2.2: The relation between the horizon and the equator. The figure shows the celestial sphere as seen from Oslo ($\phi = 60^\circ$, since Oslo lies at 60° N).

defined as

$$ZP = 90^\circ - \phi.$$

When observing the night sky from any place on Earth, the zenith is always directly overhead, but the pole's angle above the horizon (altitude) is equal to the observer's latitude.

2.2 Altitude – azimuth

This coordinate system has the horizon as the fundamental plane, and is thus a horizontal coordinate system. With reference to figure 2.3 let O , the observer on the surface of the earth (supposed spherical), be the center of the celestial sphere. Let Z be the zenith. The path OZ

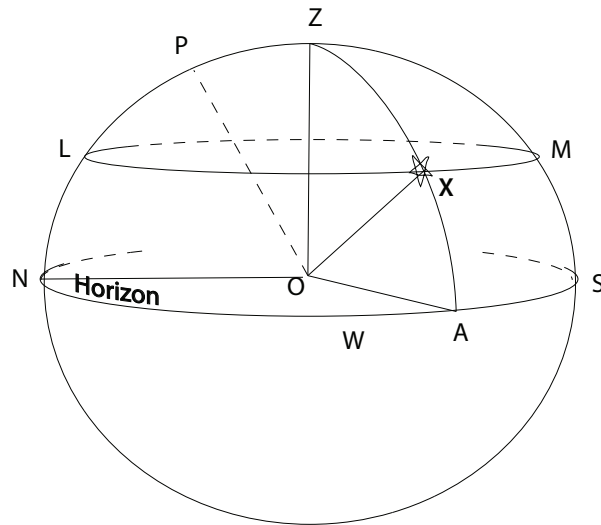


Figure 2.3: The altitude – azimuth coordinate system.

is thus the straight line joining the earth's center, O , and the zenith. The plane through O at right angles to OZ is the plane of the celestial horizon, cutting the celestial sphere in the great circle NAS .

Let X be the position of a star on the celestial sphere. Any great circle drawn through Z is a vertical circle; in particular, the vertical circle through X is ZXA . In the plane of ZXA , the angle AOX (or the great circle arc AX) is called the **altitude** denoted by a . Since OZ is perpendicular to the plane of the horizon, the great circle arc ZA is 90° ; hence $ZX = 90^\circ - a$. This angle, ZX , is called the **zenith distance** of the star X . Drawing LXM as a small circle through X parallel to the horizon, we get what is called the **parallel of altitude**.

In order to completely define a star's position on the celestial sphere, the particular vertical circle on which it lies must also be specified. Let OP be parallel to the axis about which the earth spins. On the northern hemisphere the position P is the north celestial pole. Due to this rotation the celestial sphere appears to rotate and the stars to continuously change altitude and direction. In the northern hemisphere, Polaris lies almost directly on OP and changes direction very little. Define the vertical circle through P that is ZPN as the principal vertical circle and the point N as the **north point of the horizon**.

The position of a star X on the celestial sphere at a given moment is given by reference to the horizon and the principal vertical circle ZPN . If the star is in the western part of the celestial sphere the spherical angle PZX or the great circle arc NA is called the *azimuth* (W).

2.3 Some spherical trigonometry

Both great circle angles and arcs are measured in radians (or degrees). By definition all angles and sides in a spherical triangle are less than π radians (180°). A spherical triangle is defined when we know three of its six sides or angles. The sum of the angles in a spherical triangle is greater than 180° , the difference between the sum of the angles and 180° is called the *spherical excess*.

Consider a spherical triangle, such as Figure 2.4, with corners A, B, C on a unit sphere². Assume that these corners follow each other in the positive sense. The sides a, b, c lie directly

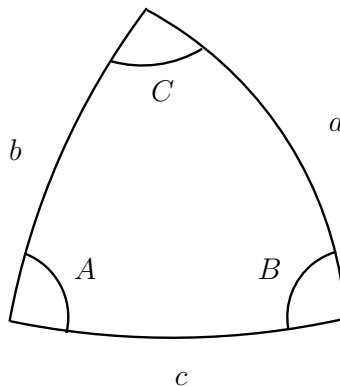


Figure 2.4: A spherical triangle. Each of its sides are part of separate great circles.

opposite these corners. Insert a right handed coordinate system x, y, z with origin at the sphere's center, let the z axis go through the point A , and the $x - z$ plane through the side c . The coordinates of the corner C are then

$$\begin{aligned} z &= \cos b \\ x &= \sin b \cos A \\ y &= \sin b \sin A. \end{aligned} \tag{2.1}$$

Now rotate the coordinate system around the y -axis until the z -axis goes through B . Call the new coordinate system x', y', z' (see figure 2.5). The corner C 's coordinates in the new system are then - since we see that the side a is equivalent to b in the old system and the angle $\pi - B$ is equivalent to A :

$$z' = \cos a$$

²Useful in the following:

$$\begin{aligned} \cos(\alpha \pm \beta) &= \cos \alpha \cos \beta \mp \sin \alpha \sin \beta \\ \sin(\alpha \pm \beta) &= \sin \alpha \cos \beta \pm \cos \alpha \sin \beta \end{aligned}$$

$$\begin{aligned}x' &= -\sin a \cos B \\y' &= \sin a \sin B.\end{aligned}\quad (2.2)$$

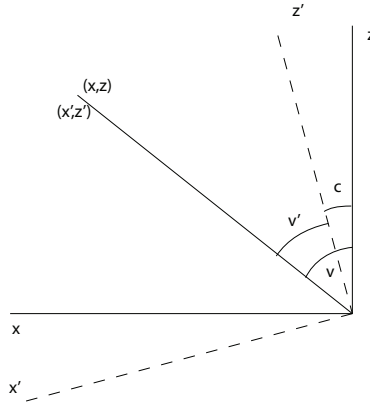


Figure 2.5: Two axis systems used to derive the basic formula of spherical trigonometry.

To find the relation between the marked and unmarked coordinates, put a plane through the $x - z$ axes. On rotation the y -coordinate is unchanged. With reference to figure 2.5 we see the following relations:

$$\begin{array}{lll}v' = v - c & z = \cos v & x = \sin v \\z' = \cos v' & & x' = \sin v'\end{array}$$

Now express z' and x' with the help of v and c

$$\begin{aligned}z' &= \cos v \cos c + \sin v \sin c \\x' &= \sin v \cos c - \sin c \cos v,\end{aligned}$$

setting in for z and x and remembering that y is unchanged gives

$$\begin{aligned}z' &= z \cos c + x \sin c \\x' &= x \cos c - z \sin c \\y' &= y.\end{aligned}\quad (2.3)$$

Setting in equations 2.1 and 2.2 in equation 2.3 gives the basic formulae of spherical trigonometry:

$$\cos a = \cos b \cos c + \sin b \sin c \cos A \quad (2.4)$$

$$\sin a \cos B = \sin c \cos b - \cos c \sin b \cos A \quad (2.5)$$

$$\sin a \sin B = \sin b \sin A \quad (2.6)$$

The first of these is the *cosine formula*, the second the *sine-cosine formula*, and the third the *sine formula*.

2.4 Declination – hour angle

Consider now again the celestial sphere as drawn in figure 2.6.

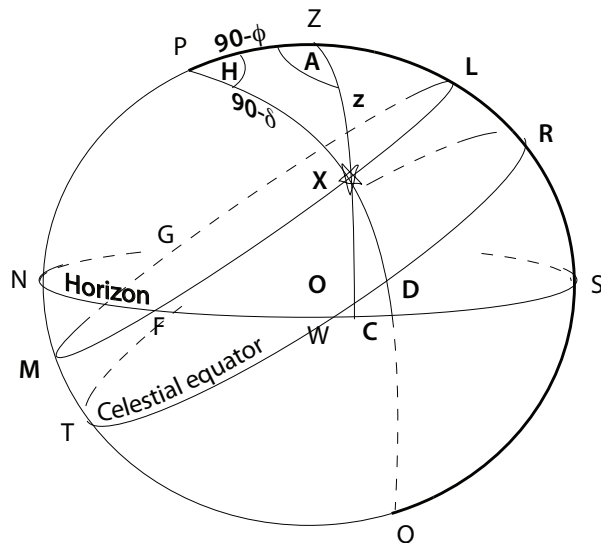


Figure 2.6: Relation between altitude – azimuth and declination – hour angle coordinates.

The great circle RWT whose plane is perpendicular to OP is the celestial equator and its plane is parallel to that of the earth's equator. The celestial equator and the horizon intersect in two points W and E . Now Z is the pole of the great circle NWS and P is the pole of the great circle RWT ; hence W is 90° from both Z and P and therefore 90° from all points on the great circle through the great circle through Z and P . This means that W is the pole of the great circle $NPZQ$; hence $NW = 90^\circ$ and $WS = 90^\circ$. Similarly $EN = 90^\circ$ and $ES = 90^\circ$. Thus W and E are the remaining **cardinal points**, in addition to N and S .

The rotation of the earth results in an apparent rotation of the celestial sphere from east to west about OP . As stars are *very* far from the earth, the angle between the straight line joining the observer at O to any particular star and the straight line OP remains unaltered. The earth's rotations makes the star X describe a small circle LXM , parallel to the celestial equator. Let $PXDQ$ be the semi-great circle through X and the poles of the celestial sphere. Then DX is called the **declination** of the star and is **north declination** if the star is between the celestial equator and the north pole. Denoting the stars declination DX by δ and $PX = 90^\circ - \delta$ is called the **north polar distance** of the star.

When we know the declination of a star, a small circle, the **parallel of declination**, is defined. In order to completely specify the stars position we need another great circle of reference. This is the semi-great circle $PZRSQ$ called the **observer's meridian**. When the star is at L on the observers meridian it is said to **transit** or **culminate** at which time it is at its greatest altitude. Afterward the star moves along the small circle LFM crossing the horizon at F , when it is said to **set** with an altitude of 0° . Eventually it will pass through its position of maximum depression at M before continuing on to G where the altitude again is 0° and is said to **rise**. At any moment the star's position on the parallel of declination is specified by the angle P between the observer's meridian and the meridian (PXQ) through

the star at this time; this angle is RPX or arc RD on the equator. This angle, denoted by H , is called the **hour angle** and is measured from the observer's meridian *westwards* from 0° (at L) to 360° (when the star returns to the observer's meridian), or more usually from 0^h to 24^h .

2.5 The standard geocentric celestial sphere

For stars, which are very far away, the position of the observer on the surface of the earth is irrelevant to the definition of the stars position. But when we are considering a relatively nearby object such as the moon, the sun, or a planet the definition of the north polar distance (and therefore of declination) previously given *is* dependent on position of the observer on the earth.

Accordingly, the center of the standard celestial sphere is taken to be at C the earth's center.

2.6 Right ascension and declination

In the hour angle and declination method of specifying a star's position on the celestial sphere only one coordinate, the declination, remains constant as the star travels across the sky.

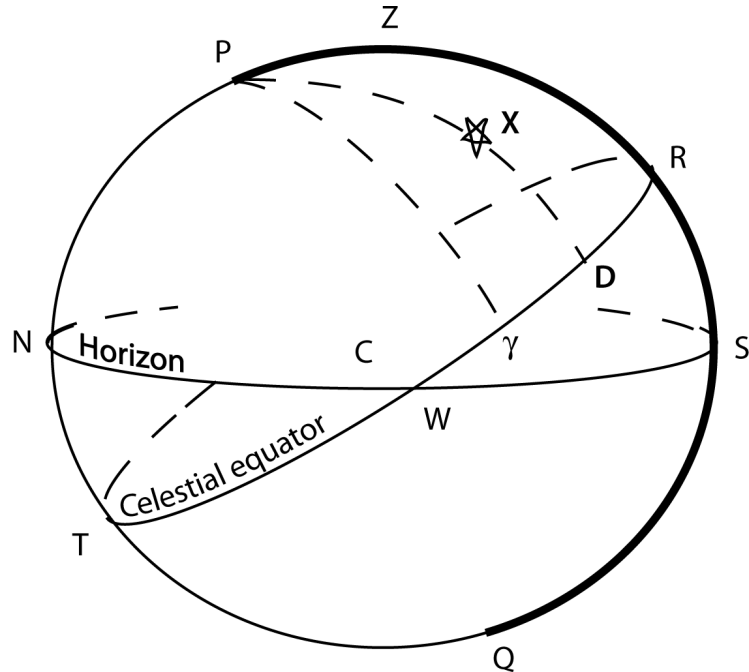


Figure 2.7: Definition of the right ascension – declination coordinate system.

Let us now pick a point Υ on the celestial equator and let the meridian through the star X cut the celestial equator at D .³ As the stars pass across the sky the declination DX remains

³The reference point Υ is not a random point, it is actually a point of intersection between the celestial equator and the ecliptic.

constant and that the relative configuration of the stars also remain constant. It follows that ΥD is constant. We regard Υ as a reference point on the celestial equator; we can then clearly specify the position of the star X by means of the great circle arc ΥD and the declination DX . The reference point chosen is called the **vernal equinox** or the **first point of Aries**. The arc ΥD is called the **right ascension** (R.A.) of the star X . It is denoted by α and is measured *eastward* from Υ from 0^h to 24^h , opposite to the direction the hour angle H is measured.

Note that $R\Upsilon = RD + \Upsilon D$. The hour angle of Υ is called the *sidereal time*⁴ (S.T.). We have accordingly

$$\text{S.T.} = H + \alpha$$

When Υ is on the observer's meridian, the hour angle of Υ is 0^h , i.e the sidereal time is 0^h . When Υ is next on the observer's meridian an interval of 24^h of sidereal time has elapsed. This interval is the same as is required for the complete revolution of the earth about its axis and is called a **sidereal day**.

2.7 The earth's orbit

According to Kepler's first law of planetary motion, the earth is a planet revolving around the sun in an elliptical path or orbit, and the sun is situated in a focus of the ellipse. Since our observations are made from Earth, then relative to the earth the sun appears to describe an elliptical path around the earth. In the course of a year the sun makes a complete circuit of the heavens against the background of the stars. The plane of the orbit is called the **plane of the ecliptic**, and the great circle in which this plane intersects the celestial sphere whose center is the earth is called the **ecliptic**. With reference to the stars, the plane of the ecliptic will be a particular great circle which is found by observations to be inclined at an angle of about 23.5° to the celestial equator.

In figure 2.8, the ecliptic and its inclination to the celestial equator, the **obliquity of the ecliptic**, is drawn. Relative to the earth, the sun appears to move on the celestial sphere along the ecliptic eastwards, in the direction as shown. Twice a year its position coincides with the intersections of the ecliptic and the celestial equator. The position Υ , at which the sun's declination changes from south to north (negative to positive), is the **vernal equinox**. It is in this way that the reference point Υ is obtained, from which the right ascension of stars is measured. From the figure, it is seen that the right ascension and declination of the sun are both changing continually. When the sun is at Υ , its right ascension and declination are both zero. This occurs roughly March 20. Following the sun's path, we reach June 20th, which is the **summer solstice**; the longest day of the year in the northern hemisphere. At this point, the right ascension is 6^h , and the declination is about 23.5° . The second intersection of the ecliptic and celestial equator is the **first point of Libra**, which is more commonly known as the **autumnal equinox**, and occurs roughly September 23. At this point, the declination and right ascension of the sun are zero again. December 21 marks the shortest day of the year in the northern hemisphere, and is called the **winter solstice**. At this point the sun's maximum elevation throughout the day is the lowest of the year. The sun then has a declination of -23.5° and right ascension 18^h .

⁴**sidereal:** of or with respect to distant stars.

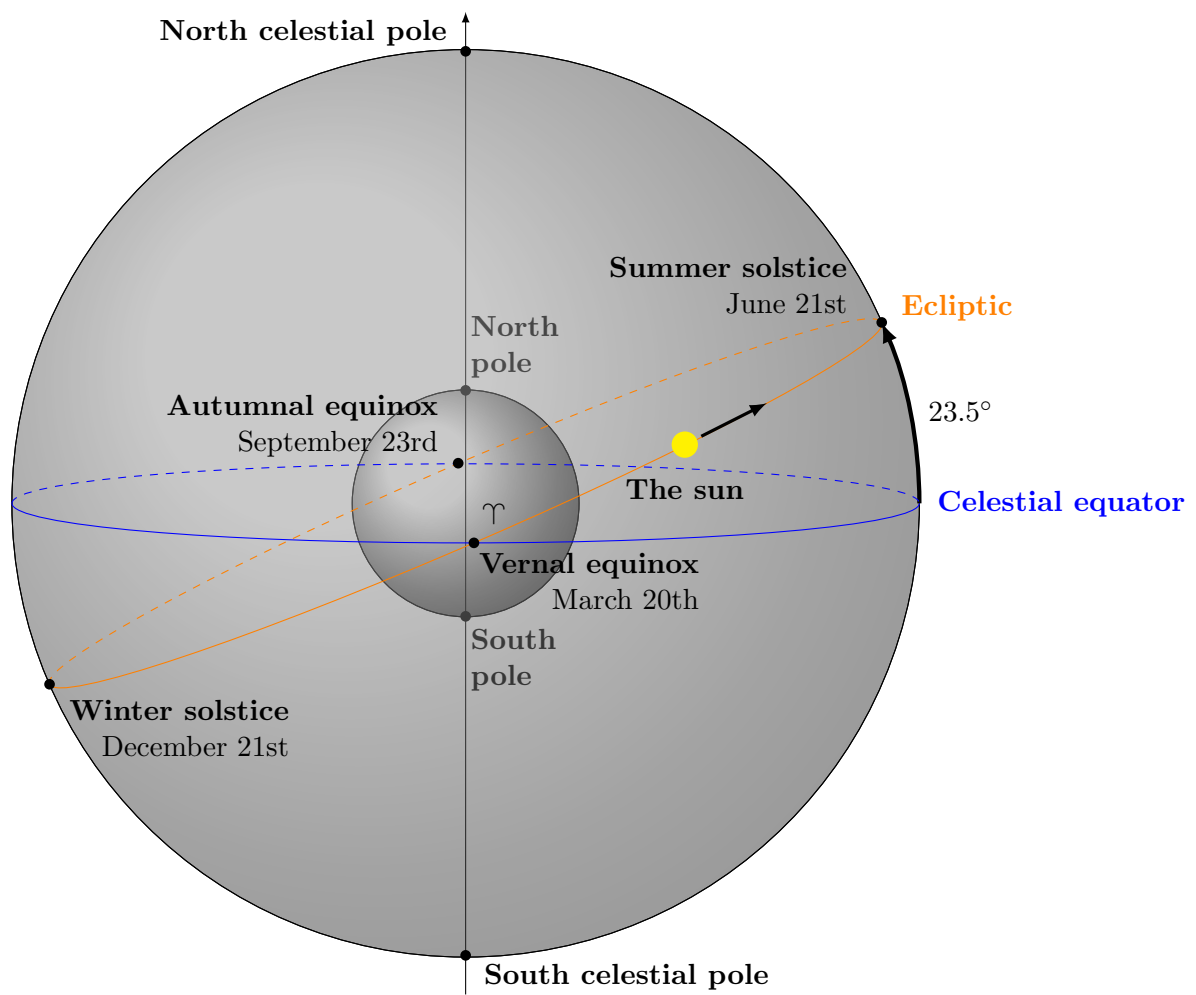


Figure 2.8: The path of the sun over the course of a year, as seen from Earth.

Please note that the situation is reversed for the southern hemisphere. When summer solstice occurs in the northern hemisphere, it is winter solstice in the southern hemisphere. The same applies to the vernal and autumnal equinox.

2.8 Celestial latitude and longitude

The position of a heavenly body can also be referred to the ecliptic as fundamental great circle and the vernal equinox Υ as principal reference point. E.g. in figure 2.9, K is the north pole of the ecliptic and KXA is a great circle arc passing through X and meeting the ecliptic in Λ . The arc $\Upsilon\Lambda$, measured from Υ along the ecliptic in the direction of the sun's annual motion (eastwards), is called the *longitude* of X and is measured from 0° to 360° round the ecliptic. The arc ΛX is the *latitude*, north is considered positive and south negative. Thus, if

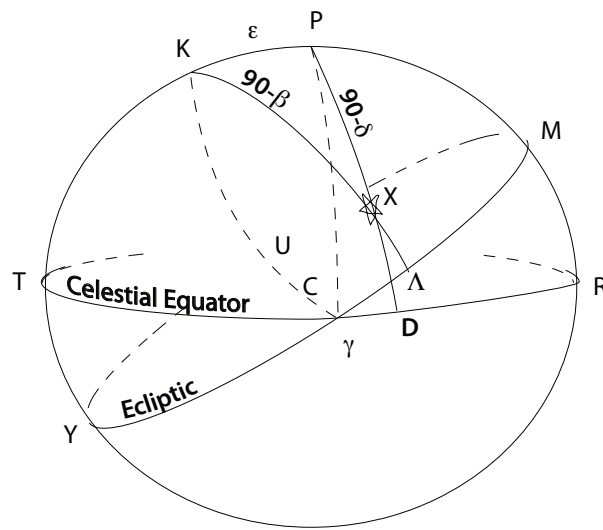


Figure 2.9: Celestial longitude and latitude.

one know a star's right ascension and declination it is possible to obtain its latitude (β) and longitude (λ) from the triangle KPX ; and vice versa.

2.9 Mean solar time

When the sun is on the meridian of a given place, it is **apparent noon** there; when the sun is next on the meridian, an **apparent solar day** has elapsed. An apparent solar day is not constant — due to the fact that the sun's apparent orbit around the earth is not a circle but rather an ellipse. In addition the sun moves along the ecliptic and not the celestial equator so it's right ascension does not increase uniformly. The average apparent solar day through the year is called a **mean solar day**. The mean sun is assumed to move in the celestial equator at a uniform rate around the earth. The rate is such that the mean sun completes its orbit in the same amount of time as the real sun needs to complete an orbit around the ecliptic.

Assume that the right ascension of the sun is known, then

$$\text{Sid.time} = \text{H.A.M.S.} + \text{R.A.M.S}$$

The mean sun is related to the true sun by certain principles that will be discussed later; for now let us define the difference as the *equation of time* E such that

$$E = \text{R.A.M.S} - \text{R.A.}\odot$$

E can be positive or negative and varies in a complicated manner.

When the mean sun is on the meridian of Greenwich, it is **Greenwich mean noon**. The hour angle of the mean sun at Greenwich is denoted G.M.A.T. (**Greenwich mean astronomical time**). Mean time reckoned from midnight at Greenwich is called **Greenwich Mean Time** (G.M.T.), now designated **Universal Time** (U.T.). Thus

$$\text{U.T.} \equiv \text{G.M.T.} = \text{G.M.A.T.} + 12^{\text{h}}$$

and similarly for any place keeping the mean time appropriate to its meridian.

2.10 Sidereal time

Sidereal time at Greenwich is given such that

$$\text{S.T. at Greenwich} = \text{S.T. at } l \pm \text{long. of } l$$

where l is the longitude of the observer with the + sign given when l is west of Greenwich and the – is given when l is east of Greenwich. The sidereal time at l is called the **local sidereal time** (L.S.T.).

Sidereal time, at any instant at a given place, is the hour angle of the vernal equinox. In section ?? the ecliptic and celestial equator were considered as fixed great circles on the celestial sphere, and thus the vernal equinox as a fixed point. However, there are both the phenomena of **precession** and **nutation**. Precession is the slow movement of the axis of a spinning body around another axis due to a torque acting to change the direction of the first axis. Nutation is a periodic variation in the inclination of a rotating object. The celestial equator can thus not be considered as a fixed great circle, and the position of the vernal equinox must be treated as a time varying quantity, slowly moving according to well established principles with reference to the background stars.

We will continue to assume the ecliptic as a fixed great circle. Owing to precession, the north celestial pole P describes a small circle about the pole K (see figure 2.9) of the ecliptic in a period of about 26 000 yr. At present P is within 1° of the star α Ursae Minoris (Polaris), but their relative positions are changing and in 12 000 yr P will be within a few degrees of Vega. It is the direction of the earth's axis that is altering continuously with reference to the background stars. Referring to figure 2.10, Υ is the vernal equinox for, say 1900.0 and Υ_1 the vernal equinox for 1901.0. The points Υ and Υ_1 are called the **mean equinoxes** at the dates in question, and the corresponding celestial equators are called the **mean equators**.

Assuming that owing to precession the north celestial pole moves uniformly along the small circle arc PP_1 and that the mean equinox moves uniformly backwards along the ecliptic from Υ to Υ_1 . It is found that the motion of Υ along the ecliptic is at the rate of 50.3 arcsec per annum.

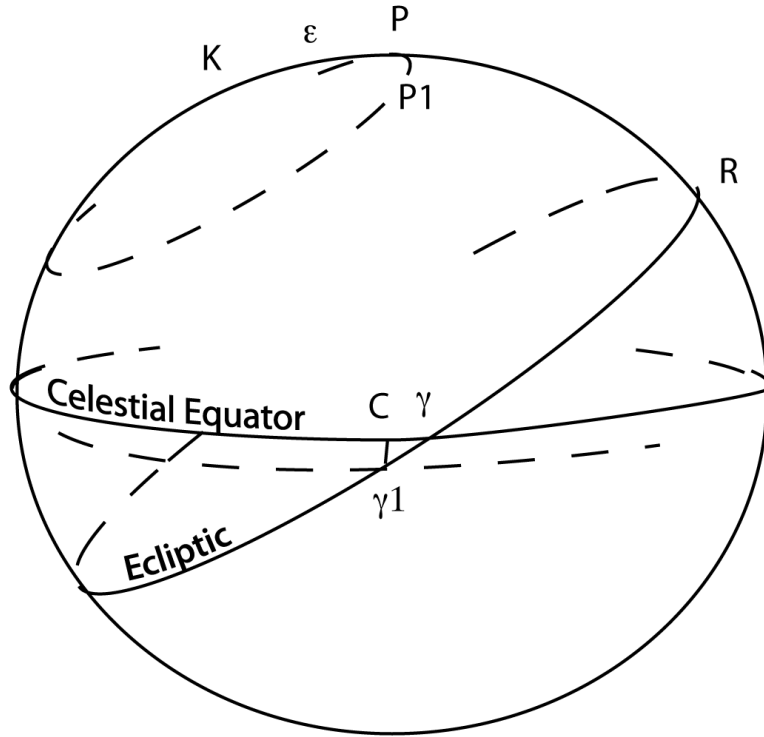


Figure 2.10: Definition of sidereal time and the effects of precession; motion of the vernal equinox.

When we define sidereal time in relation to the moving equinox, we can no longer regard the earth's rotational period to be the interval between two successive transits of the equinox. In figure 2.10 let $C\Gamma_1$ be a great circle arc drawn through Γ_1 perpendicular to the equator. Then the equinox at any given date is separating, in right ascension, from the equinox Γ for 1900.0 at a the annual rate measured by ΓC , given by the small triangle formula

$$\Gamma C = \Gamma\Gamma_1 \cos \varepsilon.$$

Hence, the mean equinox is separating, in right ascension, from Γ at the rate of 0.008 s per sidereal day. The direction of motion of the equinox is westward in the sky — opposite to that in which right ascension increases — and thus the interval between two successive transits of the moving equinox is 0.008 s less than the interval given by a fixed equinox. This first interval is a *sidereal day*, the second interval is the rotational period of the earth.

Owing to nutation the true equator at any instant is slightly different from the mean equation at that instant. Consequently the true equinox is displaced slightly along the ecliptic relative to the mean equinox; these displacements are periodic in nature (and due the effect of the moon), with a period of about 18 yr. The difference in right ascension between the true equinox and the mean equinox due this effect can amount to 1.2 s

One defines *mean sidereal time* to be associated with the moving mean equinox (only precession considered) and *apparent sidereal time* to be associated with the true equinox. The difference between these from day to day is so small in practice that generally the sidereal day is taken to mean the interval between two successive transits of the mean equinox.

2.11 Ephemeris and Universal time

There is a slight distinction between universal time, which is defined by the rotation of the earth and **ephemeris time** which is uniform and is defined by the gravitational dynamics of the solar system, independent of the earth's rotation.

When the movements of the equator and equinox due to precession are taken into account, the **fictitious mean sun** is defined to travel along the mean equator in such a way that its mean right ascension is always equal to the sun's mean longitude. This right ascension is, therefore, independent of the rotation of the earth's, and the fictitious mean sun is a suitable reference point for the definition of ephemeris time. To facilitate this an alternate meridian is defined called the ephemeris meridian which corresponds to the sidereal direction that the Greenwich meridian would have if the earth were rotating strictly uniformly. Ephemeris time is defined as

$$E.T. = 12^h + E.H.A.F.M.S.$$

where the last term of the right hand side is the ephemeris hour angle of the fictitious mean sun.

In contrast, a slightly different reference point, the mean sun, is used to define universal time. The mean sun also moves round the mean equator but at a rate that is directly proportional at each instant to the earth's angular velocity.

2.12 Terrestrial Time and Barycentric Coordinate Time

Astronomers stuck with ephemeris time until 1979, when they defined two new time scales that used the atomic second and that took into account relativity (velocity affects time). From 1 January 1984, these scales replaced ephemeris time in national ephemeris like the Nautical Almanac.

Terrestrial Dynamical Time (TDT) views time from the earth's position and motion. It was defined as being equal to TAI (Atomic time) plus 32.184 (atomic) seconds at the instant beginning 1 January 1977.

Barycentric Dynamical Time (TDB, from the French) is time at the center of mass of the solar system. TDB has various forms depending on the theory of relativity adopted.

By International Astronomical Union (IAU) Resolution A4 in 1991, Terrestrial Dynamical Time was renamed Terrestrial Time (TT). Recommendations III and V of the same resolution created Barycentric Coordinate Time (TCB) to take the place of Barycentric Dynamical Time, except in situations where maintaining continuity in ongoing work made retaining the old scale preferable.

In 2006 (Resolution B3)⁵, responding to the “multiple realizations of TDB” and other factors, the IAU defined TDB in terms of TCB. One result is that, within a few thousand years around the present, the difference between Terrestrial Time and Barycentric Dynamical Time on the surface of the Earth is less than 2 milliseconds.

2.13 The sidereal year and the tropical year

The time required by the sun to make a complete a complete circuit of the ecliptic is called a **sidereal year**.

⁵www.iau.org/static/resolutions/IAU2006_Resolution3.pdf

The **tropical year** is the average interval between two consecutive passages of the sun through the vernal equinox. Thus if Υ is the position of the equinox at a given time and Υ_1 the position of the vernal equinox one year later, the tropical year is the time taken by the sun to describe 360° less $\Upsilon_1\Upsilon$. From observations it is found to be 365.2422 days.

The relation between the sidereal year and the tropical year is then evidently

$$\text{Sid. year/trop. year} = 360^\circ / (360^\circ - 50.3'')$$

This gives a sidereal year of 365.2564 days.

During the course of a tropical year the R.A.M.S increases from 0° to 360° , that is at the rate of $360^\circ/365.2422$ or $59'8.33''$ per mean solar day. Let t_1 be the mean sidereal time when the hour angle of the mean sun at a given place is H_1 and let R_1 denote the corresponding value of the R.A.M.S.. Then

$$t_1 = H_1 + R_1$$

Let t_2 be the mean sidereal time one mean solar day later. The hour angle of the mean sun has increased by 360° and the R.A.M.S by $59'8.33''$. Hence,

$$t_2 = (H_1 + 24^h) + (R_1 + 3^m56.556^s)$$

when we convert these to time measure, so that

$$t_2 - t_1 = 24^h3^m56.556^s$$

This means that 24^h U.T. is equal to $24^h3^m56.556^s$ mean sidereal time. Note that this is equivalent to noting that during a year the earth has rotated about its axis 365.2422 times with respect with the mean sun and once more with respect to the equinox.

2.14 The Besselian year

It is the general astronomical practice to define the beginning of the tropical year (sometimes called the solar year) as the instant when the R.A. of the fictitious mean sun is exactly 18^h40^m or 280° . This instant falls near the beginning of the civil year and is usually called the **Besselian year**.

It is general practice to denote the beginning of any Besselian year by the notation e.g. 1975.0, 2008.0, etc.

2.15 The Julian date

In certain observations it is found convenient to express the instant of observations as so many days and fraction of a day after a definitive fundamental epoch. The epoch chosen is Greenwich mean noon of January 1, 4713 B.C., and for any given date the number of days which have elapsed since this epoch defines the **Julian Date** (J.D.) of the date in question.

2.16 The 3d dimension; distance

Determining the distance to astronomical objects is very difficult, and was for a very long time one of astronomy's largest unsolved problems. Hence, even today, the uncertainty in

measuring distance is enormous compared to uncertainties in direction. For example, the position of Alpha Centauri is uncertain in the ICRS (the International Celestial Reference System) by about 0.4 mas (milliarcsec), which amounts to 3 parts in 10^9 of a full circle, while its distance is uncertain by about one part in 2500.

2.16.1 The astronomical unit

Kepler's 3rd law gives the scale of planetary orbits

$$a = P^{2/3}$$

where P is the period measured in years, and a is the distance of a planet (or other object) measured in units of the average distance between object and the Sun which defines the astronomical unit; AU, or au. The presently accepted value for this length is

$$1 \text{ AU} = 1.495978 \times 10^{11} \text{ m}$$

with an uncertainty of one part in 10^6 .

2.16.2 Stellar parallax

Once the length of the astronomical unit has been established, one can measure the distances to the nearby stars through the observation of **stellar parallax**. As the Earth travels in its orbit, the apparent position of a nearby star relative very distant objects shifts. Compared to background objects, the nearby star appears to move around the perimeter of the parallactic ellipse, reflecting Earth's orbital motion. The parallax angle p is half the total angular shift in the star's position (the semi-major axis of the parallactic ellipse). From the right triangle formed by the Sun-star-Earth:

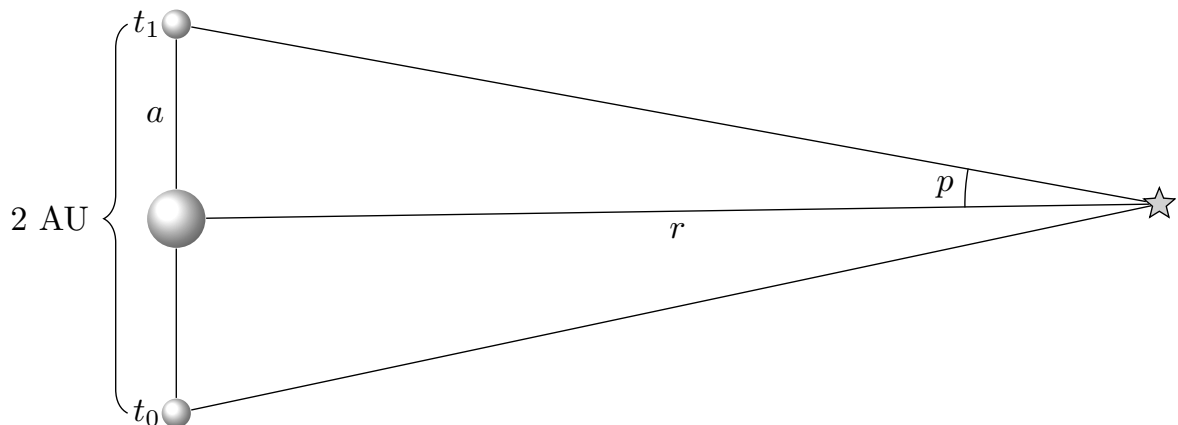


Figure 2.11: Schematic of how the parallax angle is measured. The position of a star on the sky is measured at times t_0 and t_1 (about six months apart) when the earth arrives at exactly opposite sides of the sun in its orbit. The total angular displacement of the star one measures is $2p$, but only the parallax angle p is used in calculating the distance to the star, r .

$$\tan p = \frac{a}{r}$$

where a is one AU and r is the distance to the star. Since p is very small, a very good approximation is

$$\tan p \simeq \sin p \simeq p$$

so that

$$p = \frac{a}{r}.$$

Usually one measures p in arcsec so that

$$p[\text{arcsec}] = 206\,265 \frac{a}{r}.$$

One degree equals to 60 arcminutes and one arcminute is equal to 60 arcseconds.

$$\begin{aligned} 1^\circ &= 60', \\ 1' &= 60''. \end{aligned}$$

To avoid very large numbers it is both convenient and traditional to define the unit parsec with the length

$$1 \text{ parsec} = 206\,265 \text{ AU} = 3.085\,678 \times 10^{16} \text{ m} = 3.261\,633 \text{ ly.}$$

The parsec (pc) is named as such because it is the distance of an object whose parallax is one arcsec. In the literature the parallax angle is often symbolized π instead of p .

Some history: James Bradley FRS (March 1693 - 13 July 1762) was an English astronomer the Astronomer Royal from 1742. He undertook to measure stellar parallax. Bradley could measure stellar positions with a precision of about 0.5 arcsec (500 mas). This was good enough to discover both the effects of aberration of light (1725 - 28), and the nutation of the Earth's axis (1728 - 48), but not good enough to measure the parallax of stars.

Some generations later Friedrich Bessel (1784 – 1846) studying Bradley's observations discovered that major advances in positional accuracy could be accomplished. He undertook a campaign to monitor the double star 61 Cygni along with two background stars. In 1838, after a 25 year effort(!), he succeeded in measuring its parallax to 320 mas, close to the modern value of 286 mas. Other scientists trying to measure stellar parallax at about the same time were William Struve in St. Petersburg who measured Vega, and Thomas Henderson in South Africa who measured Alpha Centauri; of these Bessel's measurement was the most accurate.

2.17 Exercises

1. Given the observers latitude ϕ , the declination δ and hour angle H of the heavenly body, calculate the zenith distance z and the azimuth A .
2. Given the observer's latitude ϕ , the stars zenith distance and azimuth, calculate the star's declination and hour angle.
3. Work out a stars latitude (β) and longitude (λ) given its declination (δ), right ascension (α) and the obliquity of the ecliptic (ε).
4. Use IDL or Matlab to produce a figure of altitude as function of hour angle for stars observed from Oslo with declinations of -30,-15,0,+15,+30,+45,+60 degrees (all in the same figure).

5. Use IDL or Matlab to produce a figure of altitude as function of azimuth for the same stars (also as observed from Oslo).

Chapter 3

Detectors

3.1 Detector parameters

The overall performance of a detector (CCD or other) is described in terms of different technical parameters. A short-list of such parameters include:

- The **quantum efficiency** (QE) is the ratio of the actual number of photons detected to the number of incident photons. This quantity varies with wavelength. In the range 300–900 nm typical values fall in the range 0.2–0.75 with maximum efficiency around 500 nm.
- The **spectral response** is the change in the output signal as a function of the wavelength of the input signal.
- The **charge transfer efficiency** (CTE) specifies the efficiency at which accumulated charge may be transferred from one pixel to the next. For a 1 % accuracy in the read-out process for a 10000 element detector a 99.9999 % transfer efficiency is required. Actual numbers as high as 99.99999 % have been quoted.
- The **dark current** represent the output from the non-illuminated detector. It is usually measured as a root-mean-square current.
- The **dynamic range** is the ratio of the saturation output to the dark current.
- The **noise equivalent power** (NEP) is the input radiative flux that gives a signal-to-noise ratio of unity. It may be given for monochromatic or black body radiation. It is usually measured in watts.
- The **detectivity** (D) is the inverse NEP value, that is, the signal-to-noise ratio for unity intensity input radiation.
- The **normalized detectivity** (D^*) is the detectivity normalized by multiplying with the square root of the product of the detector area and the electrical bandwidth of the measuring circuitry

$$D^* = \frac{(A\Delta f)^{1/2}}{NEP}. \quad (3.1)$$

The usual unit is $\text{cm Hz}^{1/2} \text{ W}^{-1}$.

The technical specifications for the CCD are improving year by year. Instead of dwelling further on such specifications or the practical challenges met with in the fabrication process of such devices, we will therefore turn to a discussion of the physical principles behind the working detector. This will require knowledge of basic properties of solid state conductors, insulators, and semi-conductors, the photo-electric effect, and the metal-oxide-semiconductor (MOS) capacitor.

3.2 Semiconductors

Many types of detectors base their properties on those of *semiconductors*. Thus, let us discuss these properties as a prerequisite to achieving an understanding of the detectors that employ them.

For a single many-electron atom the Pauli principle requires the electrons to occupy different electron states. This principle also applies to the total number of electrons in a solid block of material. Instead of the discrete energy levels of the single atom, the solid block displays a series of continuous energy bands available to the electrons. Energy bands for which every allowed electron state is occupied at zero temperature are called valence bands, energy bands that are only partially filled are called conduction bands.

From statistical mechanics the probability distribution function for finding a given energy level U occupied by an electron (of spin 1/2) is given by the Fermi-Dirac distribution function

$$f_{FD}(U) \sim \frac{1}{1 + \exp((U - U_F)/T)}, \quad (3.2)$$

where T is the temperature (in energy units, $T = \kappa T$ where κ is the Boltzmann constant and T temperature in degrees Kelvin) and U_F is the Fermi energy. The Fermi-Dirac distribution function (3.2) is displayed in figure ???. At $T = 0$ all energy levels up to U_F are occupied. At finite temperatures a definite variation of f_{FD} with U is found only for $|U - U_F|$ -values up to order T . We note that U_F represents the average energy acquired by an extra electron introduced to the material block under conditions of constant temperature. With the zero of the energy scale referred to the usual infinity of vacuum electrostatics, the Fermi energy is also referred to as the electro-chemical potential of the electron.

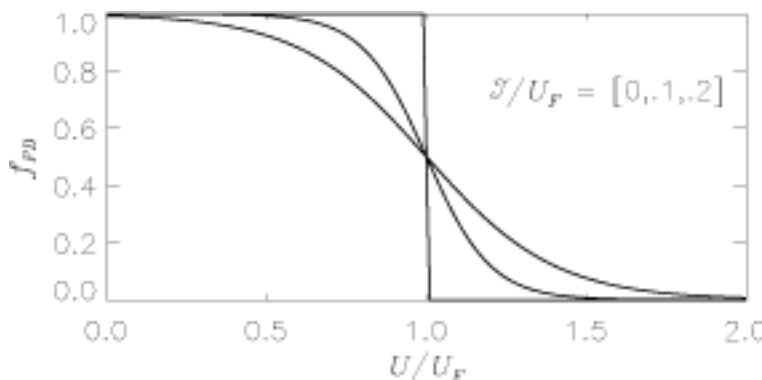


Figure 3.1: The Fermi-Dirac distribution function

If an electric field is imposed on the material, the electrons will tend to move. In this process the energy of the electron must increase, the extra energy later to be expended in

collisions with other electrons or sound generation, and leading to the Ohmic heating of the material. For an electron to increase its energy, however, a suitable empty local energy level must be available. In the absence of such energy levels the electron is not allowed to move. In metals with a partly filled conduction band there is ample supply of such empty energy levels, the conduction band electrons are free to move. The metals are therefore good electrical conductors, with the electrical conductance generally decreasing with temperature. In figure ?? valence band energy levels are drawn blue, conduction band levels red. Filled levels are illustrated with solid lines, empty levels by dashed lines.

Now consider a material made from group IV atoms like carbon (C), silicon (Si) or germanium (Ge). These atoms each make covalent bindings with their four nearest neighbors. This results in filled valence bands and an empty conduction band. For diamond (C) the energy gap between the top of the valence band U_V and the bottom of the conduction band U_C is of the order of 6 to 7 eV, much larger than the typical thermal energy of the topmost electrons. Thus, the conduction band remains empty and there are no available local energy levels for electrons in the filled valence band to move to under influence of the electric field. The electrons are thus not allowed to move and the material will be an insulator.

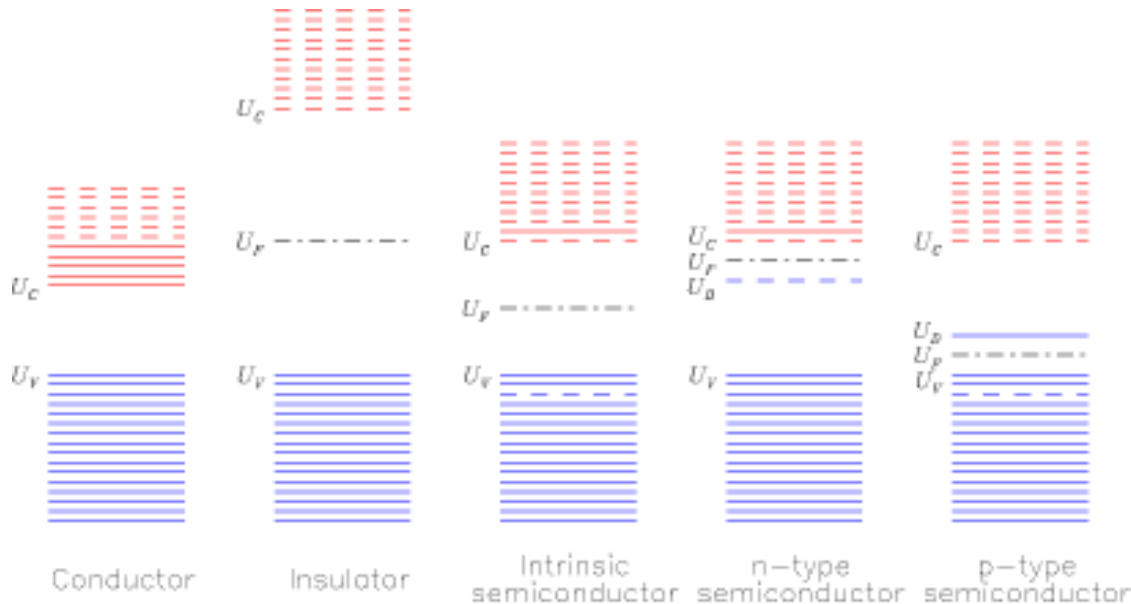


Figure 3.2: Solid state energy levels.

For crystalline silicon the corresponding energy gaps is 1.10 eV. In this case some of the electrons may be thermally excited to the conduction band even at room temperature. This leaves empty energy levels (holes) in the valence band. This means that these materials are semiconductors with an electrical conductance strongly dependent on (and increasing with) the temperature of the material. Charge is transported through the material not only by the thermally excited electrons of the conduction band. An important observation is that even an empty hole in an otherwise filled valence band will act as a free positively charged, charge carrier. Neighboring electrons of the valence band may under the influence of the imposed electric field move into the empty electron state, resulting in the motion of the hole in the opposite direction.

The number of electrons that are excited to the conduction band is determined by the

temperature through the Fermi-Dirac distribution. The Fermi energy will vary in accordance with the number of thermally excited electrons, typically taking values about halfway between U_V and U_C . This also means that if extra electrons are added to the semiconductor, about half of these are added to the conduction band, the other half occupying energy levels near the top of the valence band that are made empty. A semiconductor that has an equal number of holes and electrons that can move under the influence of an electric field is called an intrinsic semiconductor. This type of semiconductors stands in contrast to semiconductors contaminated with foreign atoms.

In a silicon crystal contaminated with group V atoms (for instance phosphor P), each foreign atom will replace one Si atom in the crystal lattice and remain fixed in this location. The foreign atom contributes one extra electron relative to the Si atom it replaces and will therefore be called a donor atom. The extra electron will occupy what are called donor impurity levels. In figure ?? these levels are denoted U_D . They are found just below the conduction band, approximately 0.05 eV from the edge of the conduction band. We recall that this is only twice the value of T at room temperature. The electrons in the donor impurity levels are thus easily thermally excited into the conduction band, leaving behind an ionized donor atom in the lattice. Such materials conduct almost entirely by negative charge carriers (electrons) and are called n-type semiconductors. Under conditions of complete ionization the number density of free charge carriers (electrons) will be equal to the number density N_D of impurity atoms.

If the silicon crystal instead is contaminated by group III atoms (for instance boron B) each foreign atom will lack one electron for a complete chemical binding. Such atoms will leave vacant levels (holes) in the valence band. These atoms are therefore called acceptors. The vacant levels, called acceptor impurity levels and denoted U_A in figure ??, are located just above the top of the valence band, approximately 0.05 eV from the edge of the valence band. Neighboring valence band electrons are easily thermally excited into the vacant levels where they will be trapped and not allowed to move. They do, however, leave behind holes in the valence band which may act as positive charge carriers. Such materials are therefore called p-type semiconductors. Again the number density of free charge carriers (holes) will be equal to the number density N_A of impurity atoms for a state of complete ionization.

We note that at low enough temperatures ($T < 70$ K) the ionization degrees for both types of doped semiconductors become negligible and therefore that the materials stop to act as semiconductors. This phenomenon is referred to as “freeze-out”. At this point the CCD will cease to function.

3.3 The photoelectric effect

The photo-electric effect traditionally refers to a process in which the energy $h\nu$ of a photon is absorbed by one electron in the surface layer of a metal, and where the energized electron subsequently escapes the metal with a maximum kinetic energy

$$U_{kin} = h\nu - W. \quad (3.3)$$

Here W represents the work function of the metal, that is, the energy needed to lift an electron from the top of the conduction band to just outside the metal surface. The photo-electric effect is important historically in that it clearly demonstrated the quantum nature of light.

In the present context we are interested in the photo-electric effect in doped semiconductors. The semiconductor will be initialized in a completely depleted state, that is, every free charge carrier will be driven away from the illuminated part of the material. We are interested in the process where the photon energy $h\nu$ is absorbed by a bounded, valence band electron, and where the electron is lifted to the conduction band and therefore becoming a free charge carrier in the semiconductor itself. The CCD detector relies on our ability to collect and subsequently count the number of such electrons being produced.

The quantum efficiency for a CCD detector can be represented in the form

$$QE = CCE(1 - R_{ref}) \exp(-x_{poly}/L_A)(1 - \exp(-x_{epi}/L_A)) \quad (3.4)$$

Here CCE is the charge collection efficiency, that is, the ability of the detector to collect all the photoelectrons generated. This is often a factor of value close to unity. R_{ref} is the reflection coefficient for silicon at the wavelength of interest, and L_A the corresponding photon absorption length in the epitaxial layer of effective thickness x_{epi} . The third factor in expression (3.4) will be present for front side illuminated CCDs with effective poly-crystalline gate thickness x_{poly} .

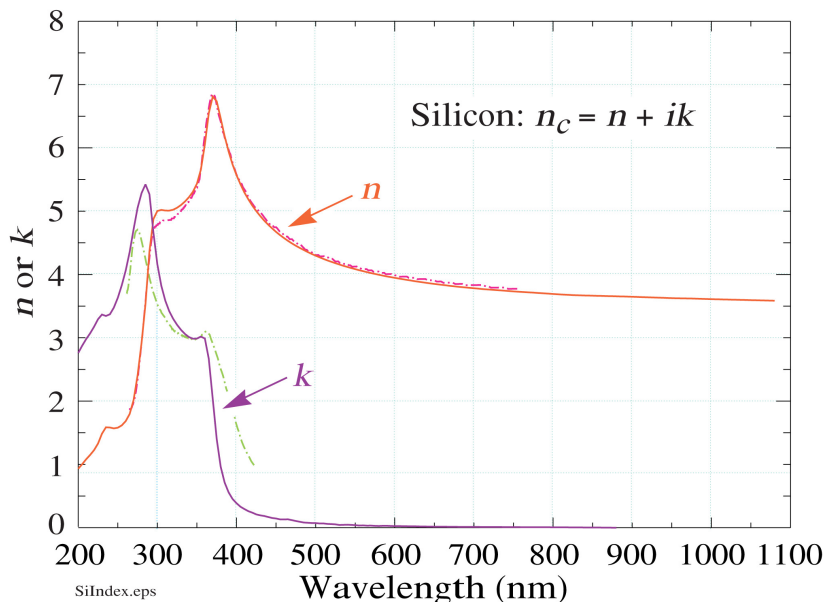


Figure 3.3: Reflection coefficients (both real and imaginary) for Si as a function of wavelength.

In figure 3.3 the reflection coefficient of silicon is plotted as a function of wavelength for the range 200-1100 nm. In figure 3.4 the corresponding absorption length is given for the same wavelength band. We notice the reduced quantum efficiency in the UV to soft X-ray range. Increased efficiency for wavelengths down to about 50 nm will result by applying phosphor coatings to the illuminated side of the CCD. The phosphor absorbs incoming photons of one wavelength and then re-emits isotropically at a longer wavelength. A loss factor of 50 % results from the isotropic re-radiation property. A popular phosphor is lumigen, effective for wavelengths less than 480 nm and re-emitting at about 530 nm.

To be able to lift a valence-band electron to the conduction band the photon energy $h\nu$ must exceed the band gap energy, $U_C - U_V \approx 1.1$ eV for silicon. This corresponds to

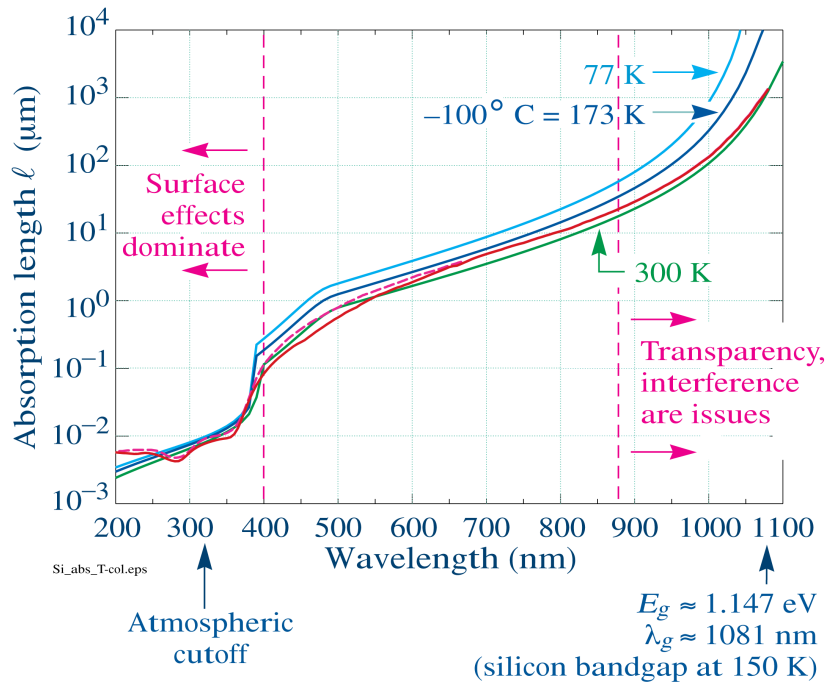


Figure 3.4: Absorption length of Si as a function of wavelength and temperature.

wavelengths $\lambda < 1090$ nm. For photons with less energy silicon will appear transparent. Note in connection with this that the electrodes at or near the surface of a detector such as a CCD can reflect some of the incident light thus reducing the detectors efficiency. One solution to this is to replace metallic electrodes with transparent polysilicon electrodes. Alternately, the detector may be illuminated from the back so that it does not have to pass through the electrodes at all. This, though, requires that the silicon forming the detector be very thin so that the electrons produced by incident radiation are collected efficiently. This process is difficult and many devices may be damaged during operation. Successfully thinned CCDs are therefore expensive as well as being fragile. At longer wavelengths the thinned CCD can become semi-transparent, this reduces the efficiency of the CCD and may in addition cause interference fringes to be produced, which must be removed in the data reduction process. Both of these effects are visible in figure 3.5, which features a solar image taken in the infrared 854.2 nm Ca II line.

For photon energy in the range 1.14 to 3.1 eV a single electron-hole pair is produced. At higher energies multiple electron-hole pairs will be produced by a single photon as energetic conduction band electrons collide with other valence band electrons. The average number of conduction band electrons effectively generated for photon energy $h\nu > 10$ eV is approximated by the empirical formula

$$\eta = h\nu/E_{e-h} \quad (3.5)$$

where $E_{e-h} \approx 3.65$ eV for silicon.

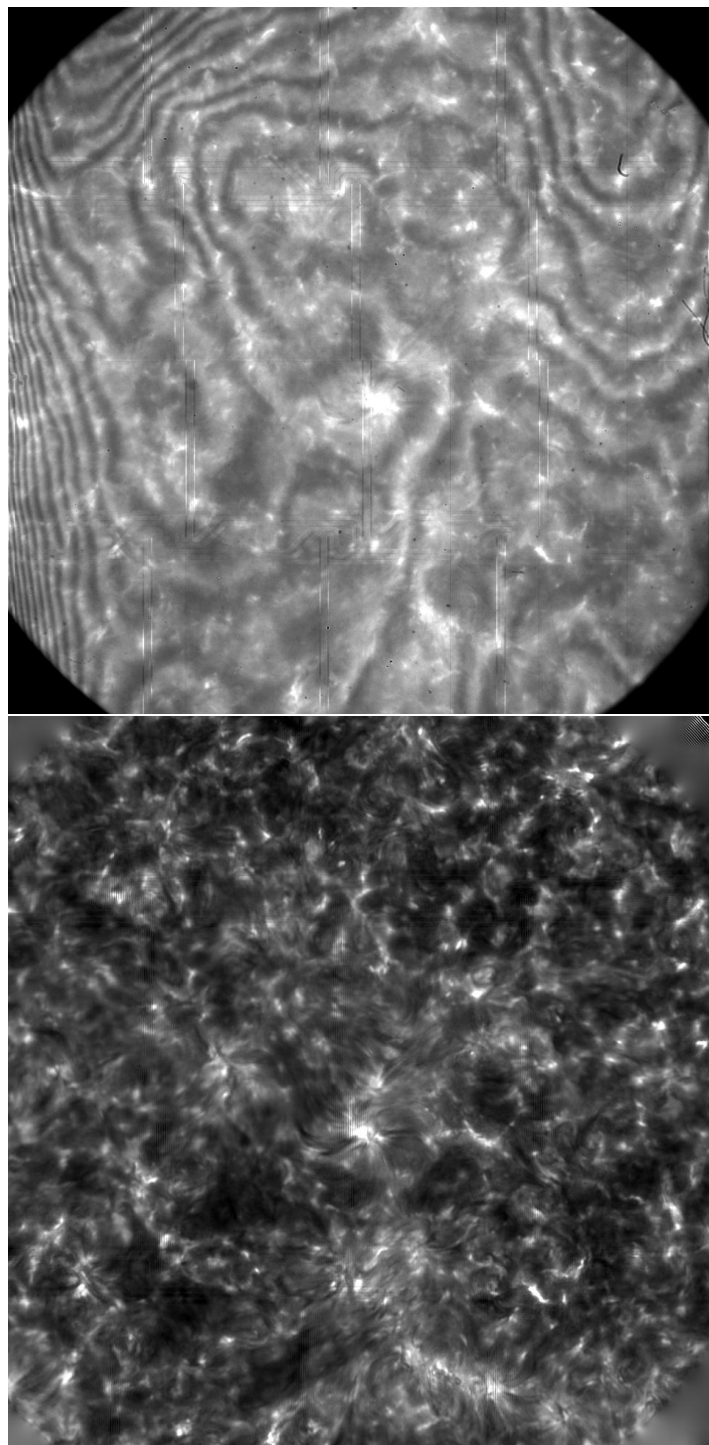


Figure 3.5: Pre- and post-processed images taken of the quiet Sun in the $\lambda 8542 \text{ \AA}$ line of Ca II at the Swedish 1-meter Solar Telescope, June 13, 2008 with the CRISP Fabry-Perot focal plane instrument. Notice that at this wavelength the CCD is partly transparent. Notice also the patterns due fringing. Most, if not all, of these artifacts can be removed with *e.g.* MOMFBD techniques.

3.4 CCDs

The CCD-detector (Charge-Coupled Device) was invented in 1969 by Boyle and Smith at Bell Telephone Laboratory, the same laboratory where the transistor was invented 20 years earlier. The CCD was originally intended for use as computer memory. Its usefulness as a electromagnetic radiation detector was, however, discovered only a few years later. The first application of a $400 \times 400 \times 15 \mu\text{m}$ pixel CCD for high-resolution astronomical imaging was made in 1975. Since then the CCD has developed into becoming the major image forming detector for infrared, optical and X-ray wavelengths in astronomy as well as in other fields. Examples include the original $800 \times 800 \times 15 \mu\text{m}$ pixel detectors for the (three-phase) Wide Field Planetary Camera (WF/PC) of the Hubble Space Telescope or the (virtual phase) $1024 \times 1024 \times 18 \mu\text{m}$ pixel detector for the Solar X-ray Telescope of the Yohkoh Satellite. CCD detectors are presently routinely produced in sizes $2\text{k} \times 4\text{k}$ pixels, but have also been produced in sizes up to 10000×10000 pixels. Detectors of this size or larger are becoming impractical due to rapidly increasing read-out times and production costs.

3.5 A simplified three-phase CCD lay-out

The CCD depends for its functioning as a photon counting device on four different operations:

1. The conversion of individual photons to elementary electric charges during the illumination period.
2. The storing of these charges over the desired exposure time.
3. The transfer of the stored charges from pixel to pixel for the read-out procedure.
4. The accurate read-out of the accumulated charge for each pixel element.

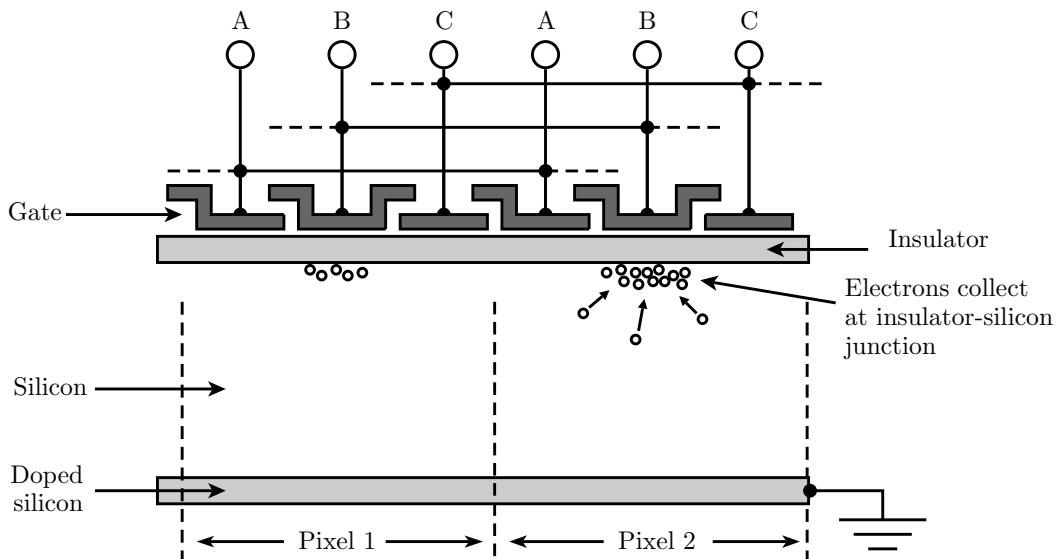


Figure 3.6: The figure shows a cross-section of two pixels on a CCD. Each pixel consists of three gates A, B, C, where all gates with the same letter are connected.

In figure 3.7 a schematic lay-out for a three-phase 4×5 CCD detector matrix is illustrated. Figure 3.6 shows a cross-section of a CCD. On top of a strongly doped p-type silicon substrate is laid a weakly doped p-type epitaxial layer, a subsequent electrically insulating SiO_2 layer and finally a layer of individual transparent, poly-crystalline silicon gate electrodes. Each pixel element consists of three such electrodes connected to three clocking voltage generators A, B and C. The colored region represent the size of one pixel. Each line of pixels is electrically separated from the neighboring lines by a strongly doped p-implant under the oxide layer, indicated by blue lines in the figure. The electrodes A, B and C for each pixel are electrically connected to the similar electrode of the other pixels. In addition to the 4×5 pixel matrix the figure shows a 4 element register with a separate set of A, B and C electrodes. The register which is shielded from radiation is needed for the read-out process.

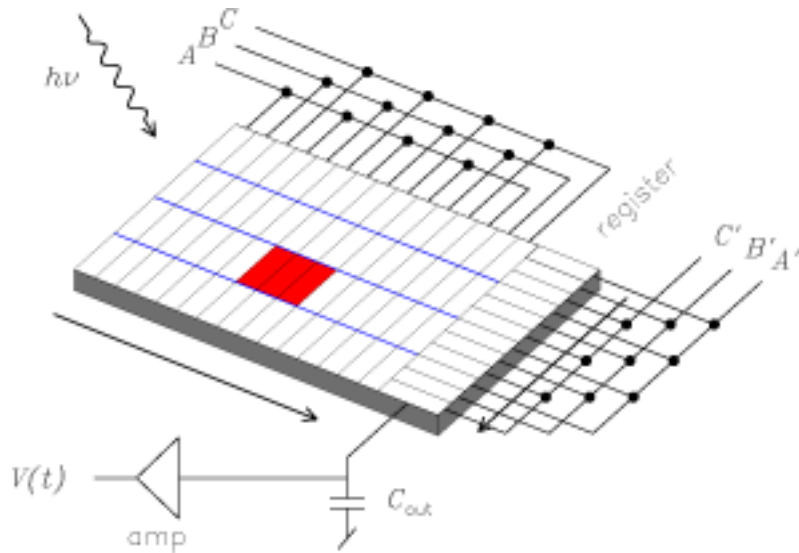


Figure 3.7: Schematic lay-out of a three-phase CCD detector

1. During the illumination phase the B-gate is held at high potential (10 V) while the A- and C-gates are kept at low potential (2 V). Individual photons penetrating into the p-layer excites valence band electrons into the conduction band.
2. These electrons are collected in the potential well created under the B-gate. The low potential of the A- and C-gates isolates charges generated in any given pixel element from those generated in the neighboring pixels.
3. The charge transfer phase is initiated by lifting C-gate to high potential. This widens the trapping potential well and drives the accumulated electrons towards the C-gate. This charge transport is strengthened by subsequently lowering the potential at the B-gate. The accumulated electrons are now transported from under the B-gate to under the C-gate. This procedure is next repeated twice, transporting the electrons further on to the A- and B-gates of the subsequent pixel element. The full procedure is then repeated until the charges accumulated over the full length of the detector array have been shifted out at the far end. See figure 3.8 for an illustration.

4. At the far end the individual shifted charge packets are dumped into the register. Before the next set of charge packets from the different pixels lines can be dumped to the register, the contents of the register cells are shifted out to the measuring capacitor C_{out} and recorded by a charge measuring circuit. From the recorded charge-versus-time series, the originating pixel element for each charge packet can be identified and the recorded image reconstructed.

We will return to study different aspects of these different stages of the CCD detector in greater detail below.

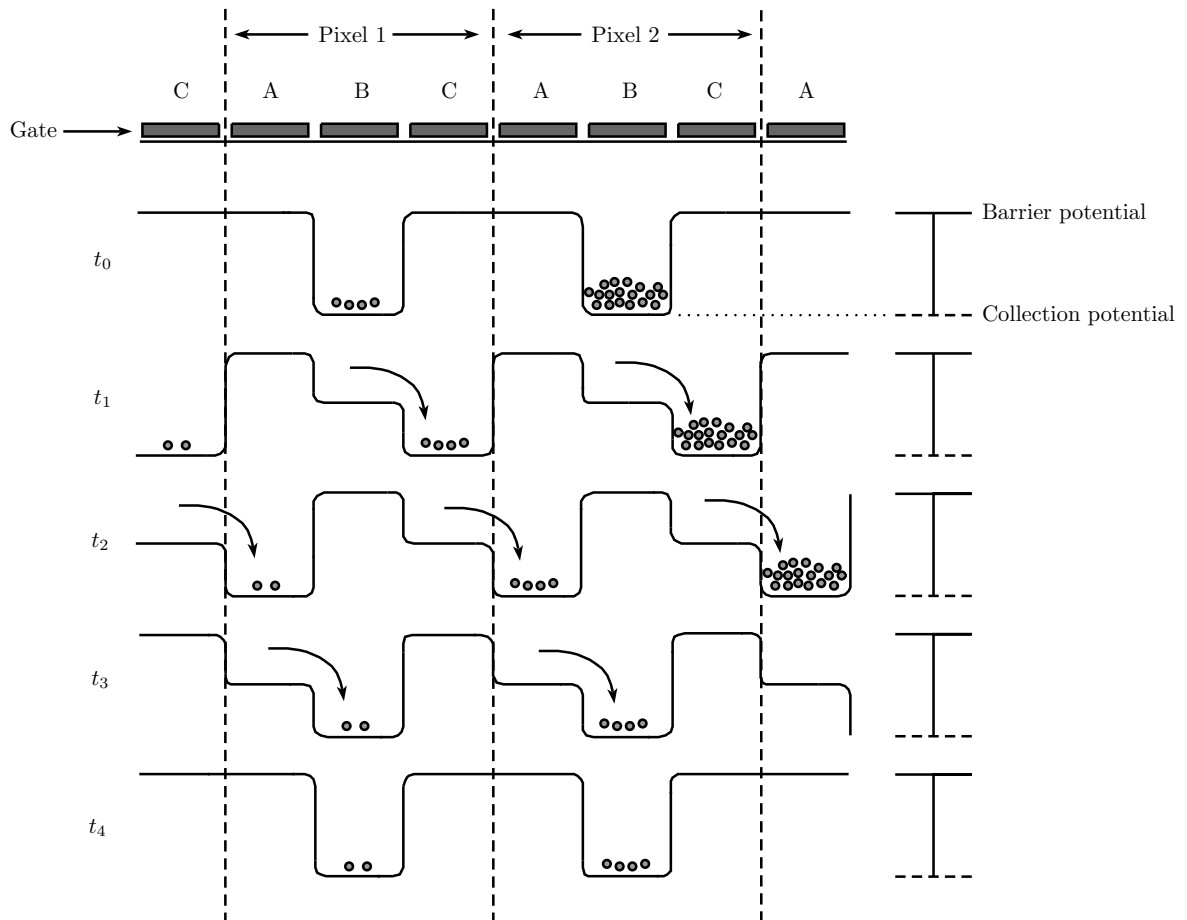


Figure 3.8: Process of moving electrons to the register. The potential across the gates are shifted so that electrons fall into the potential well that the neighbouring gate sets up.

3.5.1 Other types of clocking

Astronomical CCDs are mainly three phase devices, but there are other types as well.

A two phase CCD requires only a single clock, but needs double electrodes to provide directionality to the charge transfer process. Each pixel consists of two electrodes, one located deeper into the substrate than the other, linked to the same voltage source. Every other pixel is connected to alternating voltage sources. When the voltages cycle between, say,

2 V and 10 V the stored charge is attracted over to the nearer of the two neighboring surface electrodes and then accumulates again under the buried electrode.

Virtual phase CCDs require only one set of electrodes. Additional wells with a fixed potential are produced by p and n implants directly into the silicon substrate. The active electrode can then be at higher and lower potentials as required to move the charge through the device. The active electrodes in a virtual phase CCD are physically separated from each other leaving parts of the substrate directly exposed to incoming radiation. This enhances their sensitivity.

3.6 The surface channel MOS capacitor

Let us now consider the particular silicon structure illustrated in figure 3.9. On top of a heavily doped p-substrate another weakly doped (epitaxial) p-layer with acceptor density N_A is laid, then a layer of SiO_2 and finally a layer of poly-crystalline silicon. The latter two layers act as an insulator and a conductor, respectively. Note that the conducting poly-layer has been broken up into three separate parts for each pixel for reasons to be explained below. The dielectric constants (permittivities) of the oxide and p-layers are $\epsilon_{ox} = 3.45 \times 10^{-11} \text{ F/m}$ and $\epsilon_{si} = 1.04 \times 10^{-10} \text{ F/m}$, respectively. The oxide layer will prevent conduction currents to cross. The structure can therefore be characterized as a metal-oxide-semiconductor (MOS) capacitor.

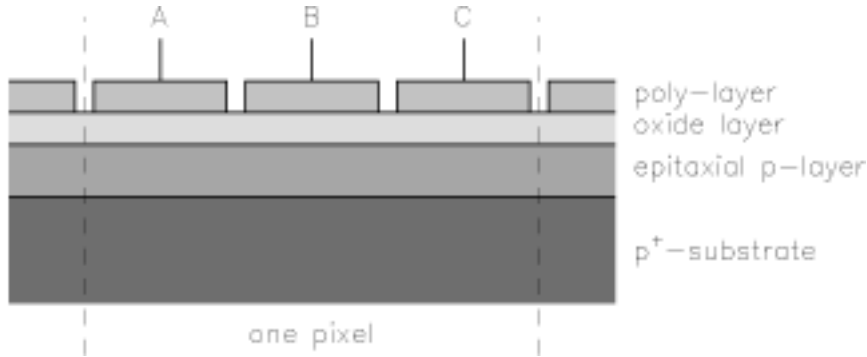


Figure 3.9: Surface channel MOS capacitor

Let the top conductive layer be given a few volts positive bias relative to the substrate. Due to the bias voltage V_G an electric field will be established across the insulator layer and reaching a distance x_d inside the p-layer. Within this distance holes will be swept away, leaving a region depleted of free charge carriers but with space charge density $-eN_A$ due to the fixed acceptor ions. The insulating layer and the depleted part of the p-layer act as two plane parallel capacitors in series, with capacitances

$$C_{ox} = \frac{\epsilon_{ox}}{d} \quad \text{and} \quad C_{dep} = \frac{\epsilon_{si}}{x_d}. \quad (3.6)$$

Inside the oxide layer a constant electric field E_{ox} will be established. Due to the existing space charge density the potential inside the depletion region will satisfy the Poisson equation

$$\frac{dV}{dx} = \frac{eN_A}{\epsilon_{si}} \quad (3.7)$$

with solution

$$V(x) = \frac{eN_A}{2\epsilon_{si}}(x - x_d)^2. \quad (3.8)$$

The electric field at the oxide-silicon interface at $x = 0$ is thus given by

$$E_S = -\frac{dV}{dx}(x = 0) = \frac{eN_A x_d}{\epsilon_{si}}. \quad (3.9)$$

The discontinuity in the dielectric constant at this interface means that there will exist a corresponding discontinuity in the electric field. Thus (remembering that $\nabla \cdot (\epsilon \mathbf{E}) = \rho_{free}$) inside the oxide layer the electric field is related to E_S through

$$\epsilon_{si} E_S - \epsilon_{ox} E_{ox} = 0. \quad (3.10)$$

The total voltage drop over the two capacitors can now be expressed in the form

$$V_G = E_{ox} d + \frac{eN_A}{2\epsilon_{si}} x_d^2, \quad (3.11)$$

from which an explicit expression for the thickness x_d of the depletion layer follows,

$$x_d = -\frac{\epsilon_{si}}{C_{ox}} + \sqrt{\left(\frac{\epsilon_{si}}{C_{ox}}\right)^2 + \frac{2\epsilon_{si}}{eN_A} V_G}. \quad (3.12)$$

The result is plotted in figure 3.10 for different gate voltages V_G for a case with uniform acceptor density $N_A = 1 \times 10^{21} \text{ m}^{-3}$.

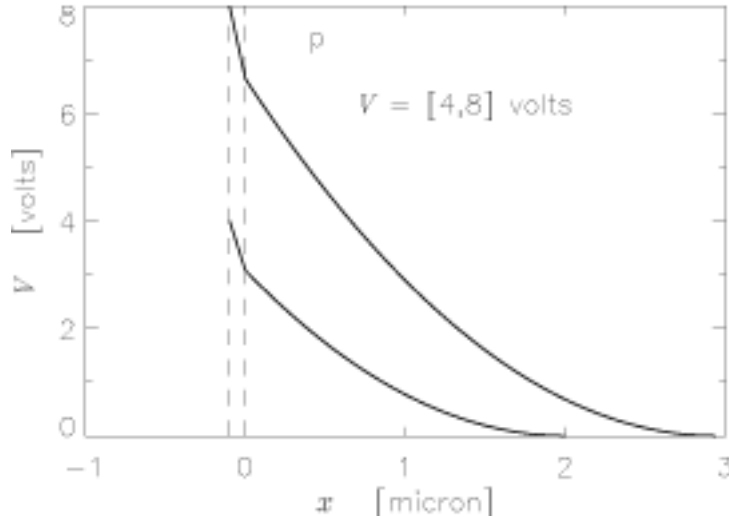


Figure 3.10: Surface channel potential well.

If the depletion layer is now illuminated, electron-hole pairs may be formed. Under the influence of the existing electric field in this region the holes will drift to the right in figure 3.10. The electrons go to the left and are trapped in the potential well at the oxide-silicon interface. If at a given time τ during the illumination \mathcal{N} electrons per unit interface area are collected, then these represent a negative surface charge density $\mathcal{Q} = -e\mathcal{N}$. With this surface

charge present the relation (3.10) between the electric field in the oxide layer and the surface electric field in the depletion region must be replaced by

$$\epsilon_{si} E_S - \epsilon_{ox} E_{ox} = Q \quad (3.13)$$

When substituted in (3.11) this means that the expression for the thickness of the depletion region (3.12) is transformed into

$$x_d = -\frac{\epsilon_{si}}{C_{ox}} + \sqrt{\left(\frac{\epsilon_{si}}{C_{ox}}\right)^2 + \frac{2\epsilon_{si}}{eN_A} V_Q}, \quad (3.14)$$

with

$$V_Q = V_G + \frac{Q}{C_{ox}}. \quad (3.15)$$

Obviously, the holding capacity of the MOS capacitor for a given gate voltage V_G is exceeded when $x_d \rightarrow 0$.

3.7 The buried channel MOS capacitor

The surface channel MOS capacitor studied above met with serious difficulties in practical applications. A fraction of the accumulated electrons tended to get trapped at imperfections at the oxide-silicon interface. It was thus not possible to achieve the CTE values required to build large array CCD detectors. Thus, the buried channel MOS capacitor was invented. This structure, showing remarkable CTE performance, differ from the corresponding surface channel structure by having an extra n-layer (donor density N_D) of thickness t introduced between the oxide and p-layer. The structure is illustrated in figure 3.11.

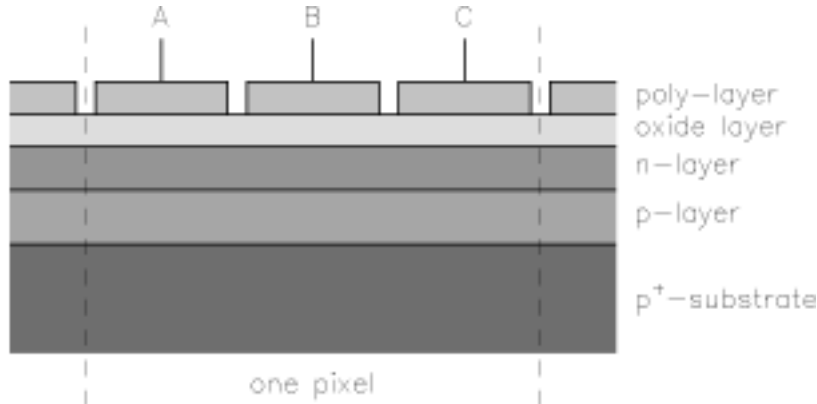


Figure 3.11: Buried channel MOS capacitor

The analysis of the buried channel MOS capacitor is only slightly more complicated than the preceding one. The extra n-layer reshapes the potential well to form a potential maximum between the oxide-silicon interface and the new n-p junction. To perform as a photo-detector, however, it is of major importance to make sure that complete depletion of majority carriers (electrons) in the n-layer has been achieved before the photon counting sequence is initiated. We return to a discussion of this requirement below.

3.7.1 Potential well

If we for the time being assume the depletion condition to be satisfied the shape of the potential well is found by solving the Poisson equation in the form

$$\frac{dV}{dx} = \begin{cases} 0 & -d < x < 0 \\ \frac{-eN_D}{\epsilon_{si}} & 0 < x < t \\ \frac{eN_A}{\epsilon_{si}} & t < x < t + x_p \\ 0 & t + x_p < x \end{cases} \quad (3.16)$$

where x_p now denotes the thickness of the p-layer depletion region. The boundary conditions require the potential to be a continuous function for the full x -range. The same applies for the electric field $E = -dV/dx$, except at the oxide-silicon interface where a discontinuity in the dielectric constant exists. The solution is

$$V(x) = \begin{cases} V_G - E_{ox}(x + d) & -d < x < 0 \\ V_{max} - \frac{eN_D}{2\epsilon_{si}}(x - t + x_n)^2 & 0 < x < t \\ \frac{eN_A}{2\epsilon_{si}}(x - t - x_p)^2 & t < x < t + x_p \\ 0 & t + x_p < x \end{cases} \quad (3.17)$$

where V_{max} is the potential maximum occurring at a distance x_n from the n-p junction. With the chosen form (3.17) of the solution the boundary conditions at $x = t + x_p$ is automatically satisfied. At $x = t$ the boundary conditions dictate

$$N_D x_n = N_A x_p \quad (3.18)$$

$$V_{max} = \frac{eN_D}{2\epsilon_{si}} x_n^2 + \frac{eN_A}{2\epsilon_{si}} x_p^2. \quad (3.19)$$

From the requirements at $x = 0$ we find

$$E_{ox} = -\frac{\epsilon_{si}}{\epsilon_{ox}} \frac{dV}{dx}_{(x=0^+)} \quad (3.20)$$

$$V_G - E_{ox}d = V_{(x=0^+)}. \quad (3.21)$$

Finally, solving for x_p we find

$$x_p = -x_2 + \sqrt{x_2^2 + x_1^2 + \frac{2\epsilon_{si}}{eN_A} V_G} \quad (3.22)$$

with

$$x_1^2 = \frac{N_D}{N_A} \left(t^2 + \frac{2\epsilon_{si}}{\epsilon_{ox}} td \right) \quad \text{and} \quad x_2 = t + \frac{\epsilon_{si}}{\epsilon_{ox}} d. \quad (3.23)$$

The solution assumes uniform donor and acceptor densities N_D and N_A , complete depletion of the n-layer, and that the thickness t and d of the n- and p-layers exceeds x_n and x_p , respectively. In figure 3.12 the solution is plotted for different gate voltages V_G for a case where $N_A = 1 \times 10^{21} \text{ m}^{-3}$, $N_D = 1 \times 10^{22} \text{ m}^{-3}$, $t = 5000 \text{ nm}$, and $d = 1000 \text{ nm}$.

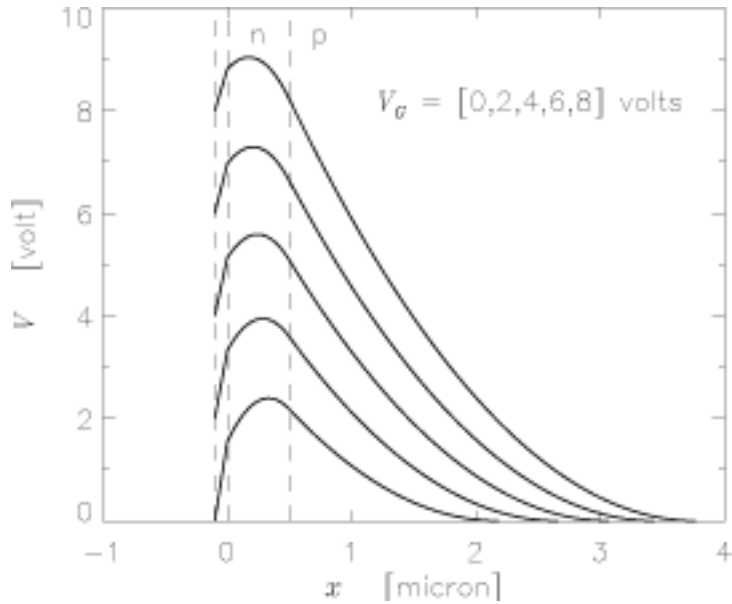


Figure 3.12: Buried channel potential well.

3.7.2 Depletion

At the n-p junction mobile carriers from both sides (electrons from the n-side and holes from the p-side) will tend to diffuse across the junction and recombine with the opposite type carriers from the other side. In this way a region on both sides of the junction will be depleted of carriers, but with space charge densities determined by the dopant concentrations, N_D and N_A , respectively. Left to itself a contact potential of approximately 0.7 V will be established across the n-p junction, creating an electric field directed from the n-side to the p-side and of sufficient strength to stop further diffusion of carriers across the junction¹.

A potential bias applied across the n-p junction will disturb this equilibrium. For a forward bias, acting to reduce the self-generated electric fields at the junction, the diffusion of majority carriers from both sides will continue and an electric current will flow across the junction. For a reverse bias the self-generated electric field will be strengthened, driving majority carriers on both sides further away from the junction and increasing the width of the depletion region.

An analysis similar to the one above will show that the widths of the depletion layers, x_n and x_p , on the two sides of the junction are given by

$$x_n = \frac{N_A}{N_D} x_p, \quad (3.24)$$

¹There are in fact small currents, even in equilibrium, but in that case they are equal such that $I_r = I_g$. The first *recombination current*, I_r is due to the majority carriers that are able to overcome the potential barrier V_b , cross the depletion barrier, and undergo recombination. I_r has two components; one caused by n-side electrons, the other by p-side holes. The magnitude of this current will depend on the temperature and on the size of the barrier. The second *generation current*, I_g , is due to minority carriers and flows in the opposite direction. The minority carriers are thermally ionized conduction-band electrons on the p-side and valence band holes on the n-side, which diffuse away from their creation sites. If they reach the depletion region, they will be swept across. Diffusion speed outside the depletion region will depend on the temperature and the impurity concentration, but I_g is independent of V_b

with

$$x_p = \sqrt{\frac{2\epsilon_{si}N_D}{eN_A(N_A + N_D)} V_{ref}}. \quad (3.25)$$

The situation is illustrated in figure 3.13.

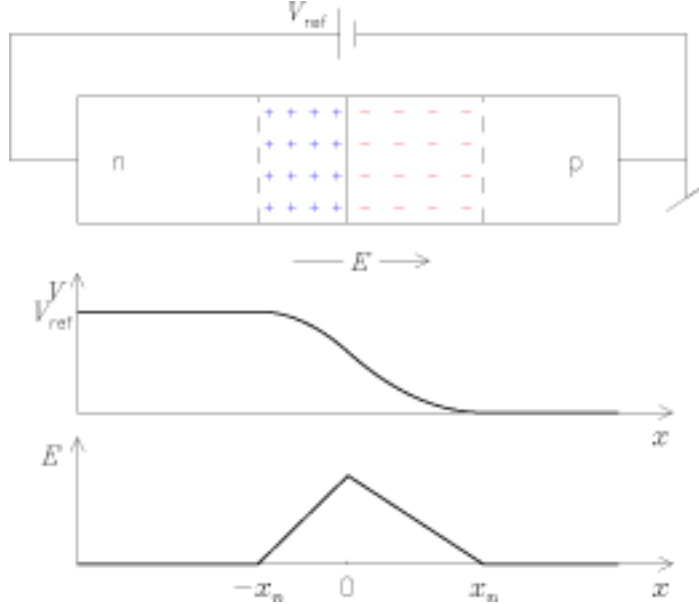


Figure 3.13: n-p junction depletion region.

Similarly, with the n-channel potential lying above the gate potential, the electric field near the oxide-silicon interface will drive n-channel majority carriers away from this interface. This creates another depletion region starting from the oxide-silicon interface. With increasing V_{ref} (the potential of the non-depleted and therefore conducting part of the n-channel) relative to the gate potential V_G , the width of the gate-induced depletion region increases. Eventually, the two depletion regions from the n-p junction and the oxide-silicon interface grow together. This occurs when $V_{max} = V_{ref}$. At this point the voltage generator supplying the V_{ref} bias to the n-channel will lose control. The n-channel is no longer conducting and the gate potential V_G will take control and govern the subsequent process. This is also the necessary initialization requirement for the buried channel CCD to work as a photo-detector.

The n-p junction described above is an example of a diode: it will carry positive current in the direction p to n, but not in the reverse direction. The size of the current will depend on the potential V_{ext} applied over the diode. Absorption of a photon in a diode causes an ionization and the creation of a conduction band electron and valence bond hole. This adds a new contribution to the generation current dependent on ϕ , the number of photons that enter the detector per second. The total current will then be something like

$$I_T = -q\phi\eta + I_r + I_g$$

where η is a factor that depends on the fraction of incident photons that are absorbed as well as the probability that a generated charge carrier will cross the junction before recombining. Electron-hole pairs created in the depletion zone are immediately swept apart by the strong

electric field there, while those created outside must first diffuse to the diffusion zone and can therefore recombine before reaching that far.

A light sensitive diode can be used in several ways:

- As a *photo-conductor* where a battery holds the external voltage to a constant value and the current is a linear function of the incident photon flux.
- As a *power-cell* the diode is connected to a constant-load resistance, and the power output depends on the incident photon flux. This is the principle behind solar power cells.
- In the *photovoltaic* mode current from the diode is held at zero, making it a stroage capicitor, and the voltage across it is a non-linear function of the photon flux.

3.7.3 Storage capacity

As the CCD detector is subsequently illuminated, the generated photoelectrons will be collected in a region around the maximum potential V_{max} in the n-channel. This region therefore becomes non-depleted, with part of the space charge density of the donor ions neutralized by the photo-electron space charge density. This in turn means that the potential maximum starts to decrease and the charge collection region to widen.

Indeed, we expect a flat-topped potential distribution within the photo-electron collection region. Due to the presence of the photo-electrons, this region will be electrically conducting and where the internal electric field and the net space charge density from donor ions and photo-electrons both vanish. The width Δx of the flat-topped potential part is therefore determined by the relation

$$\Delta x = -\frac{\mathcal{N}}{N_D}, \quad (3.26)$$

where \mathcal{N} is the collected number of photo-electrons per unit detector area.

The analysis of the buried channel MOS capacitor with photo-electrons present is rather similar to the one carried out above. The Poisson equation now reads

$$\frac{dV}{dx} = \begin{cases} 0 & -d < x < 0 \\ \frac{-eN_D}{\epsilon_{si}} & 0 < x < t - \Delta x - x_n \\ 0 & t - \Delta x - x_n < x < t - x_n \\ \frac{-eN_D}{\epsilon_{si}} & t - x_n < x < t \\ \frac{eN_A}{\epsilon_{si}} & t < x < t + x_p \\ 0 & t + x_p < x \end{cases} \quad (3.27)$$

with solution

$$V(x) = \begin{cases} V_G - E_{ox}(x + d) & -d < x < 0 \\ V_{max} - \frac{eN_D}{2\epsilon_{si}}(x - t + \Delta x + x_n)^2 & 0 < x < t - \Delta x - x_n \\ V_{max} & t - \Delta x - x_n < x < t - x_n \\ V_{max} - \frac{eN_D}{2\epsilon_{si}}(x - t + x_n)^2 & t - x_n < x < t \\ \frac{eN_A}{2\epsilon_{si}}(x - t - x_p)^2 & t < x < t + x_p \\ 0 & t + x_p < x. \end{cases} \quad (3.28)$$

The boundary conditions (3.18)-(3.21) are still valid. We note that the given form of the solution ensures that the boundary conditions at the borders of the charge collection region are automatically satisfied. The solution (3.22) is still valid, but the definitions of x_1 and x_2 in (3.23) have to be replaced by

$$x_1^2 = \frac{N_D}{N_A} \left[(t - \Delta x)^2 + \frac{2\epsilon_{si}}{\epsilon_{ox}} (t - \Delta x)d \right] \quad \text{and} \quad x_2 = t - \Delta x + \frac{\epsilon_{si}}{\epsilon_{ox}} d. \quad (3.29)$$

In figure 3.14 the potential structure for a given gate voltage V_G , but for different values \mathcal{N} of collected photo-electrons per unit detector area is given. The parameters for the MOS capacitor are identical to that of figure 3.12. With $\mathcal{N} = 15 \times 10^{14} \text{ m}^{-2}$ the charged region is less than 40 nm away from the oxide-silicon interface.

We conclude that there will exist an upper limit to how much charge can be stored in the device. An over exposure of one pixel element will mean that surplus photo-electrons will start to leak into neighboring pixels, producing a “blooming” effect in the image.

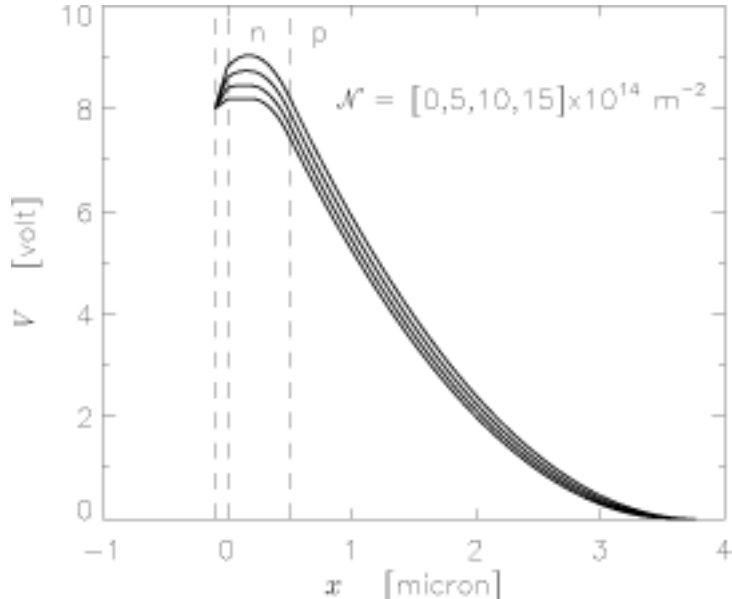


Figure 3.14: Buried channel potential structure with photo-electrons present.

3.8 The charge transfer process

After the illuminated charge generation phase the collected charges need to be transferred to a suitable charge measuring circuitry. In a three-phase CCD array each pixel is supplied with three separate gate electrodes as illustrated in figures 3.9 or 3.11, each of these electrodes are connected with the corresponding electrodes of the neighboring pixels. In the collecting phase the middle electrode of each pixel is biased high (10 V), the others low (2 V). Photo-electrons generated over the full pixel will collect in the potential well existing under the B electrode. Electrodes A and C act to isolate charges generated in the selected pixel from similar charges generated in the neighboring pixels.

At the end of the illumination period the charge transfer phase starts. This is done by applying clocking potentials to the gate electrodes as indicated in figure 3.15. The transfer of

electrons from B to C starts by raising the gate electrode C to high potential. This will widen the potential well under gate B to also include gate C. The collected electrons will drift to fill the widened potential well uniformly due to self-induced repulsion. Next the B-gate potential is lowered, creating fringing fields that push the remaining electrons under B toward C. In this way the electrons have been shifted one gate position and are ready to be shifted to gate A of the next pixel and so on. After three gate shifts the collected electrons have been moved one pixel.

Optimum performance of the transfer process is achieved for slow slew rates of the clocking signals. The characteristic RC rise and fall times τ_{RC} of the clocks are therefore often related to the one pixel transfer time t_T by

$$\tau_{RC} = \frac{t_T}{12}. \quad (3.30)$$

This is the choice made in figure 3.15. A typical value of the transfer time may be $t_T = 1 \mu\text{s}$.

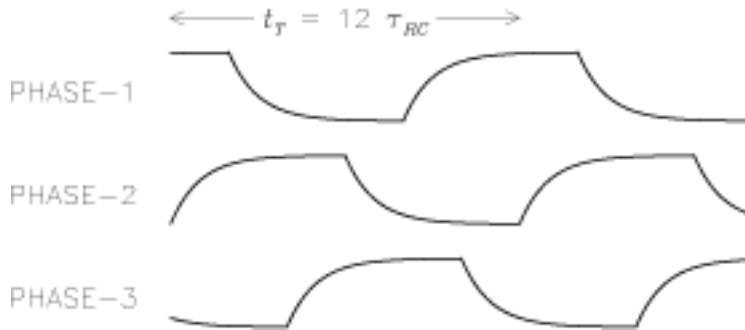


Figure 3.15: Clocking signal for three-phase CCD

3.9 Charge measurements

The final operational phase of the CCD detector is the measurement of the charges accumulated in the different pixels during the exposure time. This is accomplished by dumping the transferred charges on to a small capacitor connected to a MOSFET amplifier. The MOSFET amplifier is the only active element of the CCD detector, that is, it is the only element that requires power. The individual pixel elements made up of MOS capacitors are themselves passive elements.

The output amplifier generates a voltage proportional to the charge transferred, the larger voltages the smaller the capacitance of the output capacitor. Important engineering design criteria for the output stage is to minimize the noise generation in the MOSFET amplifier. This can be achieved by cooling the CCD detector to temperatures down to about - 90°C. Modern high-performance CCDs have achieved remarkable noise level equivalents down to less than 2 (elementary) electron charges.

3.10 Dark currents

Operating the CCD detector under reduced temperatures will also reduce problems related to dark currents in the MOS capacitors. The basic underlying assumption of the CCD as a photon counting device is that the photoelectrons are the only source of the accumulated

charge. This assumption is challenged by the existence of dark currents. Dark currents occur naturally in semiconductors through thermal generation of charge carriers. Dark current generation occurs independent of the illumination state of the semiconductor, thus its name. The only way of reducing this error source for a given detector is to lower the operating temperature. The dark current level for a given temperature is, however, strongly dependent on the fabrication process and the quality of the silicon used in the production.

There are three main regions that contribute to dark currents: the neutral bulk material below the potential well, the depleted material within the potential well and the oxide-silicon interface. Normally the latter is the more important one. Dark current carriers are generated through the presence of midband energy states halfway between the valence and conduction bands. These states are associated with imperfections or impurities within the semiconductor or at the oxide-semiconductor interface. They promote dark currents by acting as stepping stones for two-step thermal transitions of electrons and holes between the valence and conduction bands. Any electron raised to the conduction band through this process in the depleted region will be collected in the potential well together with the desired photoelectrons. Corresponding electrons generated in the field-free region outside the depletion region may enter this region through a diffusion process, then to be collected by the existing electric field.

The temperature variation of the dark current in the CCD is well described by the formula

$$I_d = C\mathcal{T}^{3/2} \exp(-U_g/\mathcal{T}), \quad (3.31)$$

where C is a constant for each detector and U_g is the silicon band-gap energy. The band-gap energy is found to follow the empirical formula (in eV units)

$$U_g = 1.1557 - \frac{7.021 \times 10^{-4} T^2}{1108 + T} \quad (3.32)$$

with temperature T given in degrees K. In figure 3.16 the dark current for the CCD normalized to unity for room temperature ($T = 300$ K) is plotted. One should bear in mind that the operating temperature of the CCD cannot be made arbitrarily low. To function the temperature of the CCD must be high enough that the dopant atoms remain in ionized state in the lattice and thus contribute to the formation of potential wells. This requires operating temperatures exceeding 70 K.

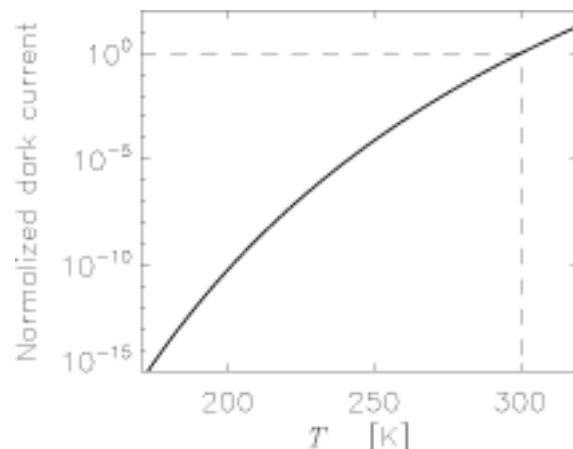


Figure 3.16: Normalized dark current as a function of temperature

3.11 CCD summary, problems and corrections

For typical noise levels and pixel capacities, astronomical CCDs have dynamic ranges of 100 000 to 500 000.

A major problem is the noise produced by cosmic rays. A single cosmic ray particle coming through one of the pixels of the detector can cause a large number of ionizations. The resulting electrons accumulate in the storage region along with those produced by photons. These are usually recognizable by the observer as ‘spikes’ in the image. Replacing such spikes is possible by using the average of the surrounding pixels, but this does not retrieve the original information lost. In addition the correction must often be done ‘by hand’ which can be time consuming. Automatic removal of spikes is sometimes possible given several individual images of the same object or a good model of the data — but such automatic removal is difficult and can become a ‘black art’.

Another defect of CCDs is the variation in the background noise between pixels. There may be large-scale variations of 10–20 % over the whole sensitive area, and there may be individual pixels with permanent high levels. The first problem can be reduced by flat fielding if its effect can be determined by observing a uniform source. The effect of a single hot spot may also be reduced in signal processing by replacing it with an average of its neighbors. However, the hot spot pixel is often also a poor transporter of charge resulting in a spurious line being introduced into the image.

Yet another problem is that of cross talk or blooming. This occurs when electrons stray to nearby pixels. This especially affects rear illuminated CCDs as in them electrons are produced quite far from the electrodes. This is the reason rear illuminated CCDs are thinned; *ie* to reduce this distance. It will also occur for any CCD where the accumulating charge nears its maximum capacity.

3.12 Other types of detectors for visible light

In these notes we have concentrated almost exclusively on CCD’s, but one should be aware that also other types of detectors exist. These are covered were summarily here and in somewhat more detail in chapter 1 of Kitchin’s *Astrophysical Techniques*.

3.12.1 Photomultipliers

Electron photomultiplier phototubes were once the workhorse of optical astronomy. They continue to be used when individual photons need to be detected as in neutrino and cosmic ray Čerenkov detectors or when very rapid responses are required as in observations of occultations.

Photomultipliers detect photons through the photoelectric effect. A photoemitter is coated on to the cathode and this is at a negative potential of some 1000 V. Once a photoelectron has escaped from the photoemitter, it is accelerated by an electric potential until it strikes a second electron emitter. The primary electron’s energy then goes into pair production and secondary electrons are emitted from the substance in a manner analogous to photo-electron emission. Several secondary electron emissions result from a single primary electron. The secondary emitter is coated onto dynodes that are successively more positive than the cathode by 100 V or so for each stage. The various electrodes are shaped and positioned so that the electrons are channelled towards the correct next electrode in the sequence

after each interaction. The final signal pulse may contain 10^6 electrons for each incoming photon.

3.12.2 Superconducting tunnel junction detectors (STJs)

Kitchin mentions that a possible replacement of CCDs could come in the form of superconducting tullen junction detectors (STJ). At temperatures below T_c , an unlimited number fo superconducting states exist at an energy Δ below the Fermi level. Single electrons will therefore occupy only states of energy ($E_F - \Delta$ or lower. Δ is a strong function of temperature rising from zero at T_c to a maximum Δ_m at temperatures below about $0.3T_c$. The value of Δ_m measures the binding energy per electron of a *Cooper pair* is very small; for example 1.4×10^{-4} eV for Pb, which is typical. If a superconductor is to absorb a photon it must have energy larger than 2Δ so that a Cooper pair can be broken up and both electrons promoted to excited states in the “conduction” band. These electrons will have quantum characteristics that differ from energetic electrons in an ordinary metal, and are therefore termed *quasiparticles*. The number of states available to quasiparticles at energies just above the gap is very large.

The STJ can operate from the UV to the longwave infrared, and also in the X-ray region. Its operating principle is based on a *Josephsons junction*. This has two superconducting layers separated by a insulating layer that is thin enough (of order 1 nm) to permit quantum mechanical tunneling. A junction can be arranged as a light-detecting diode by applying a positive bias voltage less than $V^+ = 2\Delta/q$ to one of the superconductors and a magnetic field applied parallel to the junction. If the junction is very cold all excited states are empty. In a normal Josephson junction Cooper pairs could tunnel across the insulating layer to the superconductor with applied voltage V^+ , but the applied magnetic field hindres this, and the diode does not conduct.

If the superconductor without applied voltage absorbs a photon of energy hc/λ it receives enough energy to break apart mulitple Cooper pairs, promoting a maximum of $hc/\lambda\Delta$ electrons into excited states. These quasiparticles *can* tunnel across the insulator, and those that do produce a current pulse that is inversely proportional to the wavelength λ of the exciting photon.

The STJ detector can therefore count individual incoming photons and determine their wavelength, from X-ray to infrared, of each. This is a technology still in development, but some practical multi-pixel STJ-based detectors have begun to appear at telescopes.

3.12.3 Photovoltaic cells

These are also known as photodiodes, photoconductors, and barrier junction detectors. The idea is to use the properties of a p-n junction in a semiconductor. When such a junction is in equilibrium electrons and holes have diffused across the junction until a sufficient potential difference is set up to halt the flow. The two Fermi levels are then coincident and the potential across the junction is equal to their original difference. If now light falls on the junction it can generate electron-hole pairs in both the n-type and the p-type materials. The electrons in the conduction band of the p-region will be attracted towards the n region by the intrinsic potential difference across the junction, and they will be free to flow in that direction. The holes in the valence band of the p-type material will be opposed by the potential and will not move. In the n-type region the electrons will be similarly trapped while the holes will be

pushed across the junction. Thus a current is generated by the illuminating radiation and this may simply be monitored and used as a measure of light intensity. For use as a radiation detector the p-n junction often has a region of undoped (or intrinsic) material between the p and n regions in order to increase the size of the detecting area. These devices are known as p-i-n junctions, and their operating principle does not differ from that of the simple p-n junction.

3.12.4 Thermocouples

Two dissimilar metals in contact can develop a potential difference across their junction. This is called the Seebeck effect. The position of the Fermi level will change with temperature and the change in Fermi level may not be the same in two dissimilar metals, and so at the junction the difference between the two Fermi levels will vary with temperature. In a thermocouple, two dissimilar metals are joined into a circuit that incorporates a galvanometer. When one junction is at a different temperature from the other, their Seebeck potentials differ and a current flows through the circuit.

A practical thermocouple for radiation detection is made from two metals in the form of wires that are twisted together and blackened to improve their absorption. The other junction is kept in contact with something with a large thermal inertia so that it is kept at a constant temperature. Several thermocouples are usually connected serially so that their potentials combine. This is called a *thermopile*.

Practical thermocouples and thermopiles are usually made from antimony and bismuth or from nickel and various mixtures of copper, silicon, chromium, aluminium etc. They are useful wide-band detectors, especially for infrared work. Their simplicity of operation and robustness has led to many application for them despite their relatively low sensitivity.

3.12.5 Phototransistors

These are of little direct use in astronomy because of their low sensitivity. They consist simply of a p-n-p or n-p-n transistor with the minority current carriers produced by the illumination instead of the normal emitter. Thus the current rises with increasing radiation and provides a measure of its intensity.

3.13 Infrared detectors

Many of the detectors mentioned above have some infrared (IR) sensitivity, especially out to $1\ \mu\text{m}$. At longer wavelengths, other types of detectors are needed. The IR region is conventionally divided into three: the near (NIR), $0.7\text{--}5\ \mu\text{m}$, the mid (MIR), $5\text{--}30\ \mu\text{m}$ and the far (FIR), $30\text{--}1000\ \mu\text{m}$. All IR detectors need to be cooled, with the longer the operating wavelength, the colder the required temperature. Thus in the NIR liquid nitrogen ($77\ \text{K}$) suffices, in the MIR liquid helium ($4\ \text{K}$) is needed, while one must operate at temperatures down to some $100\ \text{mK}$ in the FIR. Currently there are two types of detector in the IR: the photoconductor of the NIR and MIR (and somewhat into the FIR) and the bolometer for the FIR.

3.13.1 Photoconductive cells

These cells exhibit a change in conductivity with the intensity of their illumination. The mechanism for that change is the absorption of radiation by the electrons in the valence band of a semi-conductor and their consequent elevation to the conduction band. The conductivity therefore increases with increasing illumination, and is monitored by a small bias current. These cells have been assembled into arrays of up to 2048×2048 for the NIR and 1024×1024 for the MIR, though at the long wavelength end of the MIR arrays of some hundred cells is the maximum. In the FIR sizes are still only up to 32×32 . Unlike CCDs infrared arrays are read out pixel by pixel.

3.13.2 Bolometers

Bolometers change their electrical resistivity in response to heating by illuminating radiation. At the simplest, two strips of material are used as the arms of a Wheatstone bridge. When one is heated by the radiation its resistance changes and so the balance of the bridge alters.

3.14 Noise

In the absence of noise any detector would be capable of detecting any source, however faint. A minimum signal to noise ratio of unity is required for detection. However, most research work requires signal to noise ratios of at least 10, and preferably 100 or 1000.

Noise sources can be separated into four classes: *intrinsic noise* originating from the detector, *signal noise* arising from the character of the incoming signal, *external noise* e.g. spurious signals from cosmic rays and the like, *processing noise* from amplifiers and similar used to convert the signal from the detector into a usable form.

Intrinsic noise in solid state devices comes from four sources.

1. Thermal noise arises in any resistive material. It is due to the thermal motion of the charge carriers.
2. Shot noise occurs in junction devices and is due to variation in the diffusion rates in the neutral zone of the junction because of random thermal motions.
3. Generation-recombination noise is caused by the fluctuation in the rate of generation and recombination of thermal charge carriers.
4. Flicker noise, or ($1/f$ noise), occurs when the signal is modulated in time, either because of intrinsic variations or because it is being ‘chopped’ (i.e. source and background are alternately observed).

Signal noise can be present for a variety of reasons. One example is background noise. Noise also comes from the quantum nature of light. At low signal levels photons arrive at the detector sporadically. A Poisson distribution gives the probability of arrival, and this has the standard deviation of \sqrt{n} where n is the mean number of photons per unit time.

3.15 Exercises

1. Describe, in detail, how two phase and virtual phase CCDs move charges compared to three phase CCDs.
2. Re-derive the expressions for the total voltage drop and for thickness of the depletion region x_d for a surface channel potential well. Reproduce with `idl` the plot of the potential versus depth for gate voltages of 4, 8 and 12 V for a depleted CCD using the numbers given in the lecture notes.
3. How many electrons \mathcal{N} per unit interface area and over time τ can be collected before the thickness of the depletion region x_d approaches zero? How would you convert the number of electrons into a limiting photon flux?
4. Re-derive the expressions for the potential in an illuminated buried channel CCD, making sure that all the boundary conditions are satisfied (and understood!). How would you derive a limit for the storage capacity given in number of photoelectrons \mathcal{N} of the CCD using this expression?
5. Derive equations 3.24 and 3.25 giving the size of the depletion region in a n-p diode with reverse bias V_{ref} .
6. What is a photomultiplier? (We will discuss photomultipliers further when we cover *photometry*.)
7. Give a basic description of a *Superconducting tunnel junction detector (STJ)*. Find examples of current astronomical use (if any) and future prospects.
8. Give a basic description of how *photovoltaic cells*, *photoconductive cells*, and *bolometers* work and for which regions of the spectrum they are used for. Find examples of modern telescopes/instruments (space or ground based) on which such measurement techniques are used.

Chapter 4

Fourier analysis

4.1 Definitions

There are many common (and confusing, but ultimately trivial!) differences in defining the *Fourier transform*. One common definition is

$$F(\nu) = \int_{-\infty}^{\infty} f(t)e^{-i2\pi\nu t} dt$$

Thus $F(\nu)$ gives the wavenumber representation of the function $f(t)$. The inverse transform can be written

$$f(t) = \int_{-\infty}^{\infty} F(\nu)e^{i2\pi\nu t} d\nu$$

$F(\nu)$ is in general a complex function whose interpretation may be aided by expression in the polar coordinate form $F(\nu) = A(\nu)e^{i\phi(\nu)}$, where $A(\nu)$ and $\phi(\nu)$ are real functions where $A(\nu) = |F(\nu)|$ is the amplitude and $\phi(\nu) = \arg[F(\nu)]$ is the phase. Note that we then can write the inverse transform as

$$f(t) = \int_{-\infty}^{\infty} A(\nu)e^{i[2\pi\nu t + \phi(\nu)]} d\nu,$$

which is seen to be a recombination of all the frequency components of $f(t)$. Each component is a complex sinusoid of the form $e^{2\pi i\nu t}$ whose amplitude is $A(\nu)$ and whose initial phase (at $t = 0$) is $\phi(\nu)$. This interpretation of the Fourier transform clearly shows its relation to the *Fourier series*¹

$$f(x) = \frac{a_0}{2} + \sum_{n=1}^{\infty} [a_n \cos(nx) + b_n \sin(nx)]$$

with coefficients given by

$$\begin{aligned} a_n &= \frac{1}{\pi} \int_{-\pi}^{\pi} f(x) \cos(nx) dx \\ b_n &= \frac{1}{\pi} \int_{-\pi}^{\pi} f(x) \sin(nx) dx. \end{aligned}$$

¹Note that by using Euler's formula $e^{inx} = \cos(nx) + i \sin(nx)$ a more concise (and modern) form can be used: $f(x) = \sum_{n=-\infty}^{\infty} c_n e^{inx}$ with $c_n = \frac{1}{2\pi} \int_{-\pi}^{\pi} f(x) e^{-inx} dx$.

It is common to perform the substitution $\nu = \omega/2\pi$ which gives

$$\begin{aligned} F(\omega) &= \int_{-\infty}^{\infty} f(t)e^{i\omega t} dt \\ f(t) &= \frac{1}{2\pi} \int_{-\infty}^{\infty} F(\omega)e^{-i\omega t} d\omega \end{aligned}$$

4.2 Properties

Fourier transforms exhibit a number of properties that are very useful:

- Linearity

$$af(t) + bg(t) \iff aF(\omega) + bG(\omega)$$

- Multiplication

$$f(t)g(t) \iff \frac{1}{2\pi}(F \otimes G)(\omega)$$

where we define the *convolution* \otimes as

$$K(\omega) \equiv \int_{-\infty}^{\infty} F(\omega')G(\omega - \omega')d\omega'$$

- Convolution

$$(f \otimes g)(t) \iff F(\omega)G(\omega)$$

- Conjugation

$$\overline{f(t)} \iff \overline{F(-\omega)}$$

- Scaling

$$f(at) \iff \frac{1}{|a|}F\left(\frac{\omega}{a}\right)$$

- Time reversal

$$f(-t) \iff F(-\omega)$$

- Time shift

$$f(t - t_0) \iff e^{-i\omega t_0}F(\omega)$$

- Parsevals theorem

$$\int_{-\infty}^{\infty} f(t)\overline{g(t)}dt = \frac{1}{2\pi} \int_{-\infty}^{\infty} F(\omega)\overline{G(\omega)}d\omega$$

The *correlation* of two functions, denoted by $\text{Corr}(g, h)$, is defined

$$\text{Corr}(g, h) \equiv \int_{-\infty}^{\infty} g(t')h(t')dt'$$

The correlation is a function of t , called the *lag*. The “Correlation theorem” states that

$$\text{Corr}(g, h) \iff G(f)\overline{H(f)}$$

if g and h are real functions, as we expect for our applications [otherwise the expression on the right hand side of the correlation theorem is $G(f)H(-f)$.] The correlation of a function with itself is called the *autocorrelation*. In this case we have

$$\text{Corr}(g, g) \iff |G(f)|^2$$

which is also known as the “Wiener-Khinchin theorem”. The *total power* in a signal can be computed from the autocorrelation of that signal and following Parseval’s theorem we can write

$$\text{Total Power} \equiv \int_{-\infty}^{\infty} |g(t)|^2 dt = \int_{-\infty}^{\infty} |G(f)|^2 df.$$

Often one desires to know how much power is contained in the frequency interval between f and $f + df$. In this case it is often not interesting to distinguish between positive and negative f , but rather regard f as varying from 0 (zero frequency or DC) to $+\infty$. In this case we define the *one-sided power spectral density* of the function g :

$$P_g(f) \equiv |G(f)|^2 + |G(-f)|^2 \quad 0 \leq f < \infty,$$

when g is real the two terms in the equation above are equal, so

$$P_g(f) = 2|G(f)|^2.$$

4.3 Sampling Theorem and Aliasing

We will in general be dealing with functions $h(t)$ which are sampled at evenly spaced intervals in time (or space). Let Δ denote the time (space) interval between consecutive samples.

For any sampling interval Δ , there is a special frequency ν_c called the *Nyquist frequency* given by

$$\nu_c \equiv \frac{1}{2\Delta}$$

The critical sampling of a sine wave is two sample points per cycle. There are two aspects of the critical frequency. First, if the original signal is bandwidth limited to frequencies smaller than ν_c then the function is completely determined by its discrete samples. This is the *sampling theorem*. However, if a signal is *not* bandwidth limited to less than the Nyquist frequency then the power that lies outside the range $-\nu_c < \nu < \nu_c$ is spuriously moved into that range. This phenomena is called *aliasing*.

4.4 FFTs

Let us now estimate a Fourier transform from a finite number of sampled points. Suppose that we have N consecutive sampled values

$$h_k \equiv h(t_k) \quad t_k \equiv k\Delta \quad k = 0, 1, 2, \dots, N - 1$$

so that the sampling interval is Δ . Also assume N is even. With N numbers of input, we cannot produce more than N independent numbers of output. So, instead of trying to

estimate the Fourier transform $H(\nu)$ at all values of ν in the range $-\nu_c$ to ν_c , let us seek estimates at only the discrete values

$$\nu_n \equiv \frac{n}{N\Delta}, \quad n = \frac{-N}{2}, \dots, \frac{N}{2}$$

The extreme values of n correspond to the lower and upper values of the Nyquist critical frequency range.

The remaining step is to approximate the continuous transform by a discrete sum

$$H(\nu_n) = \int_{-\infty}^{\infty} h(t)e^{2\pi i \nu_n t} dt \approx \sum_{k=0}^{N-1} h_k e^{2\pi i \nu_n t_k} \Delta = \Delta \sum_{k=0}^{N-1} h_k e^{2\pi i k n / N}$$

The final summation is called the *discrete Fourier transform* of the N points h_k . Let us denote it by H_n :

$$H_n \equiv \sum_{k=0}^{N-1} h_k e^{2\pi i k n / N} \tag{4.1}$$

Up to now we have taken the view that index n varies from $-N/2$ to $N/2$. However, since it is clear that equation 4.1 is periodic in n we also have that $H_{-n} = H_{N-1}$. With this in mind it is customary to let n vary from 0 to $N - 1$ (one period). When this convention is followed the *zero* frequency corresponds to $n = 0$, positive frequencies $0 < \nu < \nu_c$ correspond to values $1 \leq n \leq N/2 - 1$, while negative frequencies $-\nu_c < \nu < 0$ correspond to $N/2 \leq n \leq N - 1$. The value $n = N/2$ corresponds to both $\nu = \nu_c$ and $\nu = -\nu_c$.

The discrete *inverse* transform which recovers h_k from the H_n is

$$h_k = \frac{1}{N} \sum_{n=0}^{N-1} H_n e^{-2\pi i k n / N}$$

How do we implement the discrete transform in code? The brute strength approach takes of order N^2 operations: Define W as the complex number

$$W \equiv e^{2\pi i / N}$$

Then equation 4.1 can be written

$$H_n = \sum_{k=0}^{N-1} W^{nk} h_k,$$

i.e. the vector h_k is multiplied by a matrix whose $(n, k)^{th}$ element is the constant W to the power $n \times k$. The matrix multiplication produces a vector result whose components are H_n . This multiplication evidently needs N^2 complex multiplications.

In fact, the discrete Fourier transform can be achieved in $N \log_2 N$ operations with an algorithm called the it Fast Fourier Transform or *FFT*. Here is one derivation of the FFT, that of Danielson and Lanczos in 1942. They showed that a discrete transform of length N can be rewritten as the sum of two discrete transforms, each of length $N/2$. One of the two is

formed from the even numbered points of the original N , the other from the odd-numbered points.

$$\begin{aligned}
 F_k &= \sum_{j=0}^{N-1} e^{2\pi i j k / N} f_j \\
 &= \sum_{j=0}^{N/2-1} e^{2\pi i 2jk / N} f_{2j} + \sum_{j=0}^{N/2-1} e^{2\pi i (2j+1)k / N} f_{2j+1} \\
 &= \sum_{j=0}^{N/2-1} e^{2\pi i jk / (N/2)} f_{2j} + W^k \sum_{j=0}^{N/2-1} e^{2\pi i jk / (N/2)} f_{2j+1} \\
 &= F_k^e + W^k F_k^o
 \end{aligned}$$

F_k^e denotes the k^{th} component of the Fourier transform of length $(N/2)$ formed from the even components of the original f_j , while F_k^o is the corresponding transform of length $(N/2)$ from the odd components.

This procedure can be applied recursively; having reduced the problem of computing F_k to that of computing F_k^e and F_k^o , one can do the same reduction of F_k^e to the problem of computing the transform of its $N/4$ even-numbered inputs data, F_k^{ee} , and $N/4$ odd-numbered data F_k^{eo} . When we start with an original N which is a integer power of 2 (one should only use FFTs with N a power of 2, padding the input data with zeroes is necessary) we can continue applying the Danielson-Lanczos method until the original data is subdivided all the way down to transforms of length one. The Fourier transform of length one is just the identity operation that copies its one input number into its output slot. Thus, for every pattern of e 's and o 's numbering $\log_2 N$ in all there is a one-point transform that is given by

$$F_k^{eoeeeo...oee} = f_n \quad \text{for some } n$$

Which value of n corresponds to which pattern? Reverse the pattern of e 's and o 's, let $e = 0$ and $o = 1$ and one will have, *in binary*, the value of n . This is because the successive subdivisions of the data into odd and even are tests of successive least significant bits of n . Thus by rearranging the input vector f_j in bit reversed order so that the individual numbers are in the order obtained by bit reversing j . The points are given as one-point transforms. These are recombined with the adjacent number to give two-point transforms, then combine adjacent pairs again to give 4-point transforms, and so on, using the Danielson-Lanczos formula at every step.

The FFT therefore has a structure where first the data are sorted into bit reversed order and thereafter the transforms of length $2, 4, 8, \dots, N$ are computed implementing the Danielson-Lanczos formula.

4.5 Exercises

Experiment with the **fft** function in **idl**. First make an x -axis, *eg idl> x=findgen(2000)/100.*2.*!pi*

1. Compute the amplitude of the transform of $f = \sin x$. In plotting this amplitude, what should be used for the x -axis?

2. What happens if you set the edges of f to zero: *eg* multiply f by a step-function s such as `idl> s=fltarr(2000) & s[200:1800]=1.0?` Overplot the amplitude of the transform as you narrow the region of s that is equal to one.
3. Compute the transform of step-functions of various widths.
4. Add sinusoidal functions to f with different frequencies and check the resulting transforms. What happens to the transform if you add a constant to f ?
5. Consider a function g given by the sum of three sinusoids of differing frequency. Construct such a g and remove one of the frequencies from g using forward and back transforms FFT's in `idl`.

Chapter 5

Diffraction I

Let us now consider how light reacts to being confined to a given aperture. The resolution of an aperture is restricted due to the wave nature of light: as light passes through any opening it is *diffracted* and the wave fronts spread out in a shape given by the envelope of Huygens's secondary wavelets which radiate spherically outwards from all points on a wave front. These waves travel along every path, from the source to the point of observation, where they are added together only giving a significant net contribution when they add coherently in phase. (In the following I will follow Kip Thorne's lecture notes found at [www.pma.caltech.edu/Courses/ph136/yr2004.](http://www.pma.caltech.edu/Courses/ph136/yr2004/))

5.1 Helmholtz-Kirchhoff Integral

Let us restrict attention to the simplest (and, luckily the most useful) case: a monochromatic scalar wave

$$\psi = \psi(\mathbf{x})e^{-i\omega t}$$

with field variable ψ of frequency $\omega = ck$ which satisfies Helmholtz's equation

$$\nabla^2\psi + k^2\psi = 0 \tag{5.1}$$

except at the boundaries. ψ is generally a real physical value, but for convenience we will use a complex representation. The wave is monochromatic and non-dispersive and the medium is isotropic and homogeneous so that k can be treated as a constant¹. This formalism is valid for weak sound waves in a fluid and is fairly accurate for the propagation of electromagnetic waves in vacuum or in a medium with a constant dielectric constant ϵ . In the latter case ψ can be considered as one of the Cartesian components of the electric or magnetic field vector, e.g. E_x or B_y . In vacuum Maxwell's equations imply that $\psi = E_x$ satisfies equation 5.1.

The Helmholtz equation 5.1 is an elliptic, linear, partial differential equation, and thus permits us to express the value of $\psi_{\mathcal{P}}$ of ψ at any point \mathcal{P} inside some closed surface \mathcal{S} as an integral over \mathcal{S} of some linear combination of ψ and its normal derivative.

Let us derive this expression by augmenting the actual wave ψ in the interior of \mathcal{S} with a

¹Each of these assumptions can be lifted at the cost of introducing technical complications.

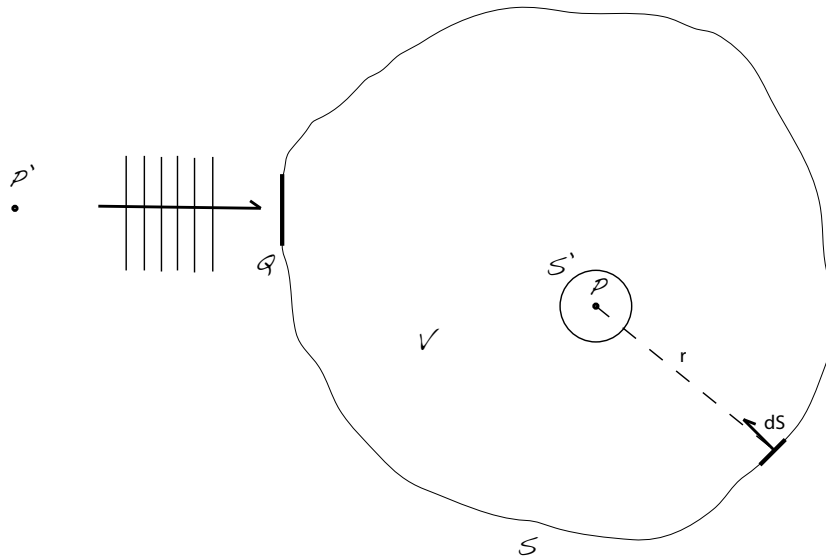


Figure 5.1: Surface \mathcal{S} for the Helmholtz-Kirchhoff integral. The surface \mathcal{S}' surrounds the observation point \mathcal{P} , and \mathcal{V} is the volume bounded by \mathcal{S} and \mathcal{S}' . The aperture \mathcal{Q} , the incoming wave to the left of it and the point \mathcal{P}' are used later in the text.

second solution² of the Helmholtz equation, namely

$$\psi_0 = e^{ikr}/r.$$

This is a spherical wave originating from the point \mathcal{P} , and r is the distance from \mathcal{P} to the point where ψ_0 is evaluated. Now apply Gauss' theorem

$$\int_{\mathcal{V}} \nabla \cdot \mathbf{F} dV = \int_{\mathcal{S}} \mathbf{F} \cdot d\mathbf{S}$$

to the vector field $\psi \nabla \psi_0 - \psi_0 \nabla \psi$ and invoke Helmholtz equation to arrive at

$$\int_{\mathcal{S}+\mathcal{S}'} (\psi \nabla \psi_0 - \psi_0 \nabla \psi) \cdot d\mathbf{S} = - \int_{\mathcal{V}} (\psi \nabla^2 \psi_0 - \psi_0 \nabla^2 \psi) dV = 0 \quad (5.2)$$

Where we have introduced a small sphere \mathcal{S}' of radius r' surrounding \mathcal{P} ; \mathcal{V} is the volume between the two surfaces \mathcal{S} and \mathcal{S}' ; and we have made the opposite choice of direction for the integration element $d\mathbf{S}$ – it points into \mathcal{V} instead of outwardly as is usual, changing the sign of the second expression in the equation above.

Now let the radius r' decrease to zero. We then find that

$$\psi \nabla \psi_0 - \psi_0 \nabla \psi \rightarrow -\psi(0)/r'^2 + O(1/r')$$

²Remember that in spherical polar coordinates we write the gradient of a scalar as

$$\nabla f = \frac{\partial f}{\partial r} \mathbf{e}_r + \frac{1}{r \sin \theta} \frac{\partial f}{\partial \phi} \mathbf{e}_\phi + \frac{1}{r \sin \theta} \frac{\partial f}{\partial \theta} \mathbf{e}_\theta$$

and the divergence as

$$\nabla \cdot A = \frac{1}{r^2} \frac{\partial}{\partial r} (r^2 A_r) + \frac{1}{r \sin \theta} \frac{\partial A_\phi}{\partial \phi} + \frac{1}{r \sin \theta} \frac{\partial}{\partial \theta} (A_\theta \sin \theta)$$

and thus the integral over \mathcal{S}' becomes $4\pi\psi(\mathcal{P}) \equiv 4\pi\psi_{\mathcal{P}}$.³ We then have

$$\psi_{\mathcal{P}} = \frac{1}{4\pi} \int_{\mathcal{S}} \left(\psi \nabla \frac{e^{ikr}}{r} - \frac{e^{ikr}}{r} \nabla \psi \right) \cdot d\mathbf{S}. \quad (5.3)$$

This equation is the *Helmholtz-Kirchhoff formula* is the expression relating ψ at \mathcal{P} to a linear combination of its value and normal derivative on a surrounding surface. If \mathcal{P} is many wavelengths away from the boundary \mathcal{S} , then the integral is only influenced by the waves ψ as they enter through \mathcal{S} , and not when they are leaving.

5.2 Diffraction by an aperture

Next let us suppose that some aperture \mathcal{Q} of size much greater than a wavelength but much smaller than the distance to \mathcal{P} is illuminated by a distant wave source. Let \mathcal{S} pass through \mathcal{Q} , and denote by ψ' the wave incident on \mathcal{Q} . Assume that the diffracting aperture has a local and linear effect on ψ' : that the wave transmitted through the aperture is given by

$$\psi_{\mathcal{Q}} = t\psi',$$

where t is a complex transmission function that varies over the aperture. In practice, t is usually zero or unity. However, t can also represent a variable phase factor when, for example, the aperture comprises a medium of variable thickness and of different refractive index from that of the homogeneous medium outside the aperture.

Let us now use the Helmholtz-Kirchhoff formula 5.3 to compute the field at \mathcal{P} due to the wave $\psi_{\mathcal{Q}} = t\psi'$ transmitted through the aperture. The surface \mathcal{S} comprises the aperture \mathcal{Q} , a sphere of radius $R \gg r$ centered on \mathcal{P} , and the linear extension of the aperture to meet the sphere; and assume that the only incoming waves are those which pass through the aperture.

On the aperture, as $kr \gg 1$, we can write $\nabla(e^{ikr}/r) \simeq -ik\mathbf{n}e^{ikr}/r$ where \mathbf{n} is a unit vector pointing towards \mathcal{P} . Similarly we write $\nabla\psi \simeq ik\mathbf{n}'\psi'$, where \mathbf{n}' is a unit vector along the direction of propagation of the incident wave (and where our assumption that anything in the aperture varies on scales long compared to $\lambda = 1/k$ permits us to ignore the gradient of t). Inserting these gradients into equation 5.3 one obtains

$$\psi_{\mathcal{P}} = -\frac{ik}{2\pi} \int_{\mathcal{Q}} d\mathbf{S} \cdot \left(\frac{\mathbf{n} + \mathbf{n}'}{2} \right) \frac{e^{ikr}}{r} t\psi' \quad (5.4)$$

This equation can be used to compute the wave from a small aperture at any point \mathcal{P} in the far field. It has the form of an integral transform for the incident field variable ψ' , where the integral is over the area of the aperture. The kernel of the transform is the product of several factors: the factor $1/r$ ensures that the flux or energy (proportional to ψ^2) falls off as the inverse square of the distance to the aperture. The phase factor $-ie^{ikr}$ advances the phase of the wave by an amount equal to the optical path length between the element of the aperture and \mathcal{P} , minus $\pi/2$. The amplitude and phase of the incoming wave ψ' can also be changed by the transmission function t . Finally there is the *obliquity factor* $d\hat{\mathbf{S}} \cdot (\mathbf{n} + \mathbf{n}')/2$, where $d\hat{\mathbf{S}}$ is the unit vector normal to the aperture.

³See Exercise 2.

5.3 Spreading of the wavefront

Equation 7.1 gives a general description for computing the diffraction pattern from an illuminated aperture. It is commonly used in two different limits, called *Fraunhofer* and *Fresnel*.

Suppose that the aperture has a linear size a and is roughly centered on the geometric ray from the source point \mathcal{P}' to the field point \mathcal{P} . Consider the variations of the phase ϕ of the contributions to $\psi_{\mathcal{P}}$ that come from various places in the aperture. Using trigonometry we can estimate that locations on opposite sides of the aperture produce phases at \mathcal{P} that differ by

$$\Delta\phi = k(r_2 - r_1) \sim ka^2/2r, \quad (5.5)$$

where r_1 and r_2 are the distances from the two edges of the aperture to the point \mathcal{P} .

There are two limiting regimes depending on whether the aperture is large or small compared with the *Fresnel length*

$$r_F \equiv \left(\frac{2\pi r}{k} \right)^{1/2} = (\lambda r)^{1/2}$$

When $a \ll r_F$, the phase variation $\Delta \sim a^2/r_F^2$ is $\ll \pi$ and can be ignored; the contributions from different parts of the aperture are essentially in phase with each other – this is the *Fraunhofer* regime. When $a \gg r_F$, $\Delta\phi \gg \pi$ and the phase variation is very important in determining the observed intensity $|\psi_{\mathcal{P}}|^2$ – this is the *Fresnel* regime.

Consider a planar wave propagating perpendicular to an aperture of size a . Wave optics insists that the transverse localization of the wave into a region of size $\Delta x \sim a$ must produce a spread in its transverse wave vector, $\Delta k_x \sim 1/a$ (a momentum of uncertainty⁴ $\Delta p_x = \hbar\Delta k_x \sim \hbar/a$.) This uncertain transverse vector produces, after propagating a distance r , a corresponding uncertainty $(\Delta k_x/k)r \approx r_F^2/a$ in the beam's transverse size; and this uncertainty superposes incoherently on the aperture-induced size a to produce a net transverse beam size

$$\begin{aligned} \Delta x &\sim \sqrt{a^2 + (r_F^2/a)^2} \\ &\sim a \quad \text{if } r \ll a^2/\lambda \quad \text{Fresnel regime} \\ &\sim \left(\frac{\lambda}{a} \right) r \quad \text{if } r \gg a^2/\lambda \quad \text{Fraunhofer regime.} \end{aligned}$$

In the nearby Fresnel regime the aperture creates a beam whose edges will have the same shape and size as the aperture itself, and will be reasonably sharp but with some oscillatory blurring associated with wave-packet spreading. By contrast in the more distant Fraunhofer regime wave front spreading will cause the transverse size of the entire wave to grow linearly with the distance, and the intensity pattern will typically not resemble the aperture at all.

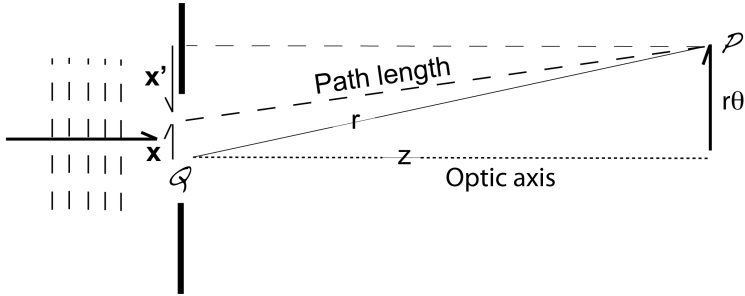


Figure 5.2: Geometry for computing the path length between a point Q in the aperture and the observation point P . The transverse vector \mathbf{x} is used to identify Q in the Fraunhofer analysis and in a later lecture \mathbf{x}' is used for Fresnel analysis.

5.4 Fraunhofer diffraction

Consider now the Fraunhofer regime and specialize to the case of an incident plane wave with wave vector \mathbf{k} orthogonal to the aperture plane. Regard the line along \mathbf{k} through the center of the aperture Q as the “optic axis”; identify points in the aperture by their two-dimensional vectorial separation \mathbf{x} from that axis; identify P by its distance r (note change in definition of r) from the aperture center and its 2-dimensional transverse separation $r\theta$ from the optic axis. Now, restrict attention to small angle diffraction $|\theta| \ll 1$. The geometric path length between P and a point \mathbf{x} on Q can be expanded as

$$\text{Path length} = (r^2 - 2r\mathbf{x} \cdot \theta + x^2)^{1/2} \simeq r - \mathbf{x} \cdot \theta + \frac{x^2}{2r} + \dots$$

The first term in this expression, r , just contributes an \mathbf{x} -independent phase e^{ikr} to ψ_P . The third term, $x^2/2r$, contributes a phase variation that is $\ll 1$ here in the Fraunhofer region (but will be important in the Fresnel region). Therefore, in the Fraunhofer region, we can retain just the second term $-\mathbf{x} \cdot \theta$ and write equation 7.1

$$\psi_P(\theta) \propto \int e^{-ik\mathbf{x} \cdot \theta} t(\mathbf{x}) d^2x \equiv \bar{t}(\theta)$$

Where d^2x is the surface area element in the aperture plane and we have dropped a constant phase factor and constant multiplicative factors. Thus, $\psi_P(\theta)$ in the Fraunhofer regime is given by the two dimensional Fourier transform denoted by $\bar{t}(\theta)$, of the transmission function $t(\mathbf{x})$, with \mathbf{x} made dimensionless in the transform by multiplying with $k = 2\pi/\lambda$.

5.5 Diffraction of a single slit

Consider now a single transparent stripe, a slit, of width a centered on $x = 0$, and measure the scalar angle θ from the direction of the incident radiation. This slit has the transmission

⁴In this way we can achieve a quick and dirty “derivation” of the Rayleigh criterion using photons with momentum p impinging on a lens of diameter a which gives that the resolution ($\theta = \Delta p_x/p$) may be found as

$$\theta = \Delta p_x/p = \frac{h/a}{h/\lambda} = \lambda/a.$$

function

$$\begin{aligned} t_1(x) &= 1 \quad |x| < a/2, \\ &= 0 \quad |x| > a/2. \end{aligned}$$

Its diffraction pattern is

$$\begin{aligned} \psi_{\mathcal{P}}(\theta) &\propto \bar{t}_1 \\ &\propto \int_{-a/2}^{a/2} e^{ikx\theta} dx \\ &\propto \text{sinc}\left(\frac{ka\theta}{2}\right), \end{aligned} \tag{5.6}$$

where $\text{sinc}(x) \equiv \sin(x)/x$.

5.6 Babinet's principle

In the previous section we have shown how to compute the Fraunhofer diffraction pattern formed by a narrow slit. We might also be interested in the pattern produced by the complementary aperture, *i.e.* a needle of width and length the same as the slit. We can derive the needles pattern by observing that the sum of the waves from the two apertures should equal the wave from a completely unaltered incident wave front. That is to say if we exclude the direction of the incident wave, the field amplitude diffracted by the two apertures are the negative of each other, and hence the intensities $|\psi|^2$ are the same. Therefore the Fraunhofer diffraction patterns from the needle and the slit — and indeed from any complementary apertures — are identical, except in the direction of the incident wave.

5.7 Diffraction by a circular aperture

Let us now compute how well a telescope can distinguish neighboring stars. We cannot expect to resolve them (or any two objects) that are closer together in the sky than the angular width of the diffraction pattern formed by the telescope's aperture. Of course, optical imperfections and pointing errors in a real telescope may degrade the image quality even further, but this is the best that can be done, limited only by the uncertainty principle.

The calculation is straightforward using equation 7.1 and assuming a circular aperture telescope with diameter D :

$$\begin{aligned} \psi(\theta) &\propto \int_{\pi D} e^{-ikx\cdot\theta} d^2x \\ &\propto \text{jinc}\left(\frac{kD\theta}{2}\right) \end{aligned}$$

where $\text{jinc}(x) \equiv J_1(x)/x$ with J_1 the Bessel function of order one. The flux from a star observed at angle θ is therefore $\propto \text{jinc}^2(kD\theta/2)$. This intensity pattern is known as the *Airy pattern*. There is a central “Airy disk” surrounded by a circle where the flux vanishes, and then further surrounded by a series of concentric rings whose flux vanishes with radius. Only 16% of the total light falls outside the the central Airy disk. The angular radius θ_A of the Airy disk, *i.e.* the radius of the dark circle surrounding it, is determined by the first zero of $J_1(kD\theta/2)$ which is found to be $\theta_A = 1.22\lambda/D$.

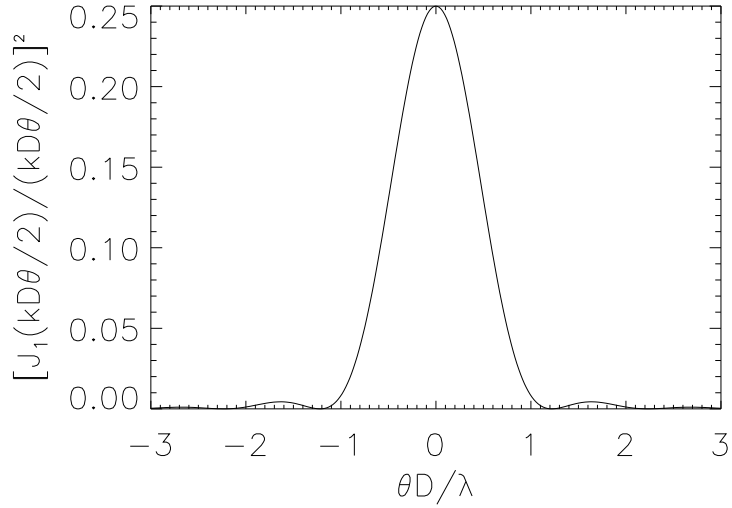


Figure 5.3: Airy diffraction pattern for a circular aperture. Note the first zero of the function at $\theta D/\lambda = 1.22$.

5.8 Exercises

1. Confirm that the expression in Eq. 5.2 is correct by using Gauss' theorem.
2. Carry out the integral over \mathcal{S}' in Eq. 5.2 by letting the radius r' go to zero, and show that its value is $4\pi\psi_p$.
3. Why can we write $(r_2 - r_1) \sim a^2/2r$ in Eq. 5.5? Draw a figure to show the geometry of the problem.
4. Carry out the integral in Eq. 5.6, and show that the result is correct.
5. The intensity of radiation is proportional to the square of ψ . Plot, for example with IDL, the intensity pattern from the diffraction of a single slit in the Fraunhofer regime.
6. Write a IDL routine that plots a cut through the Airy disk such as figure 5.3 and, in addition, plots an image of the Airy disk.

Chapter 6

Telescopes for visible light

Astronomers use telescopes to collect radiation from astronomical sources and to estimate their direction and structure as well as spectral and absolute intensities. The wide range of photon energies involved in astronomical observations means that the telescopes are very different in form depending on wavelength band. We can subdivide telescope types roughly into four categories.

- detectors which sense the direction of arrival and energy of individual (gamma-ray) photons
- non-focusing (X-ray) collimators which restrict the field of view of the detector
- phased arrays, and pencil beam interferometers (metre wavelength)
- reflecting or refracting telescopes which focus incoming radiation (all wavelengths except gamma-rays)

Here we will concentrate on the latter category, and especially to those telescopes used to observe visible and infrared radiation.

The theoretical consideration of resolution that we discussed in previous lectures is only applicable if the lens or mirror as well as the intervening atmosphere is of sufficient optical quality that the image is not already degraded beyond the diffraction limit. There are many effects that will blur an image and these are collectively known as aberrations. With one exception they can all effect images produced by both lenses or mirrors. The universal or monochromatic aberrations are known as the Seidel aberrations. The exception is chromatic aberration and the related second order effects of transverse chromatic aberration and secondary color, and these only effect lenses.

6.1 Lenses, mirrors and geometric optics

The speed of light in a vacuum is a constant, c , identical for all observers. The *phase velocity* v of light in a dielectric medium such as air, water, or glass is always less than c such that

$$n(\lambda) = \frac{c}{v(\lambda)}$$

where n is the *index of refraction*, which in general is a function of the wavelength λ . Another important characteristic of a material is thus the *chromatic dispersion* $dn/d\lambda$. Glassmakers

traditionally express this dispersion as the Abbe number, or costringence, defined in equation 6.2, which depends roughly on the reciprocal of the dispersion.

Along a ray of light moving through a medium (a homogenous medium will have straight rays of light) one can measure the distance s that light moves in time t

$$s = \frac{ct}{n}$$

Points of equal s delineate a surface called the *geometrical wavefront*. Wavefronts are always perpendicular to rays. If ds is an infinitesimal element along a ray path the ray travel time is

$$\tau = \int \frac{ds}{v} = \frac{1}{c} \int n ds = \frac{w}{c}$$

where w is the *optical path length*. In some situations with a coherent source (where all waves are emitted in phase) the geometrical wavefronts also correspond to surfaces of equal phase.

6.1.1 Fermat's principle and Snell's law

Fermat's principle states that the path of a ray between two points will always be an extremum in total travel time τ or optical path length.

Consider a situation where a plane separates two different materials, and assume that the index of refraction is larger in the material on the right. A light ray that travels towards the right will strike the normal to the surface at the *angle of incidence*, θ_1 , and the ray splits into two components - a reflected ray, and a refracted ray. These two rays make angles θ_R and θ_2 with the normal, which is measured so that positive angles counterclockwise from the normal.

Fermat's principle implies the law of reflection

$$\theta_1 = -\theta_R.$$

We can also deduce the path of the refracted ray by requiring the optical path between two fixed points P_1 and P_2 to be an extremum. This argument leads to Snell's law of refraction

$$n_1 \sin \theta_1 = n_2 \sin \theta_2 \quad (6.1)$$

(Note that this expression reduces to the law of reflections for $n_1 = -n_2$.)

For a ray coming from a medium with a larger index of refraction there is a *critical angle* which produces a refracted ray that never leaves the medium, which one can see is given by

$$\theta_C = \sin^{-1} \left(\frac{n_1}{n_2} \right)$$

This state of affairs is called a *total internal reflection*, where the angle of incidence is greater than θ_C , where all light that reaches the interface is reflected back into the higher index medium.

Snell's law is a general result that applies to any shape, and can be used as the foundation of almost all geometrical optics.

6.1.2 Reflection and transmission coefficients

The laws governing the relative *intensities* of incident and reflected, refracted beams are complicated and fall outside the realm of geometrical optics. *Fresnels formulas* for reflection and transmission coefficients give the amplitudes of the reflected and refracted waves as a function of angle of incidence, polarization, and indices of refraction. A few results are worth stating:

- Polarization is important. Waves polarized with the electric field vector perpendicular to the plane of incidence (transverse electric phase), are reflected differently than waves polarized with the magnetic field perpendicular to the plane of incidence (transverse magnetic).
- The reflectance, R , is the fraction of the power of the incident wave that is reflected. At normal incidence ($\theta_1 = 0$) and for all cases

$$R = \left(\frac{n_1 - n_2}{n_1 + n_2} \right)^2$$

- For both transverse electric and transverse magnetic polarization the reflectance becomes large at large angles of incidence. In the external case, $R \rightarrow 1.0$ as $\theta_1 \rightarrow 90^\circ$ and light rays that strike a surface at grazing incidence close to 90° will be mostly reflected. For the internal case, $R = 1.0$ for all angles greater than the critical angle.
- For all values of θ_1 other than those described above R is smaller for transverse magnetic than for transverse electric polarization. Thus initially unpolarized light become partially polarized after reflection from a dielectric surface. At one particular angle, *Brewster's angle* $\theta_p = \tan^{-1}(n_1/n_2)$, $R = 0$ for transverse magnetic polarization and only one polarization is reflected.

6.1.3 Reflection from a spherical surface

Consider a concave spherical surface with radius R and center C as shown in figure 6.1. The line that is coincident with the axis of symmetry (goes through C and the center of the surface) is called the *optical axis*. Set up a Cartesian coordinate system where the z -axis lies on the optical axis and the origin, the *vertex* (V) is at the point where the surface meets the optical axis. Let us describe the situation in the $y - z$ plane. The *paraxial approximation* assumes that all incident rays are nearly parallel to the optical axis, and that all angles of reflection are small. This latter means that the diameter of the mirror is small compared to the radius of curvature.

Consider the ray that originates at the *object* at point O on the optical axis and is reflected at point P to reach the image at I . If the point P is at position y_p then we can deduce that

$$\begin{aligned}\alpha_o &\approx \tan \alpha_o \approx \frac{y_p}{s_o} \\ \alpha_c &\approx \tan \alpha_c \approx \frac{y_p}{R} \\ \alpha_i &\approx \tan \alpha_i \approx \frac{y_p}{s_i}\end{aligned}$$

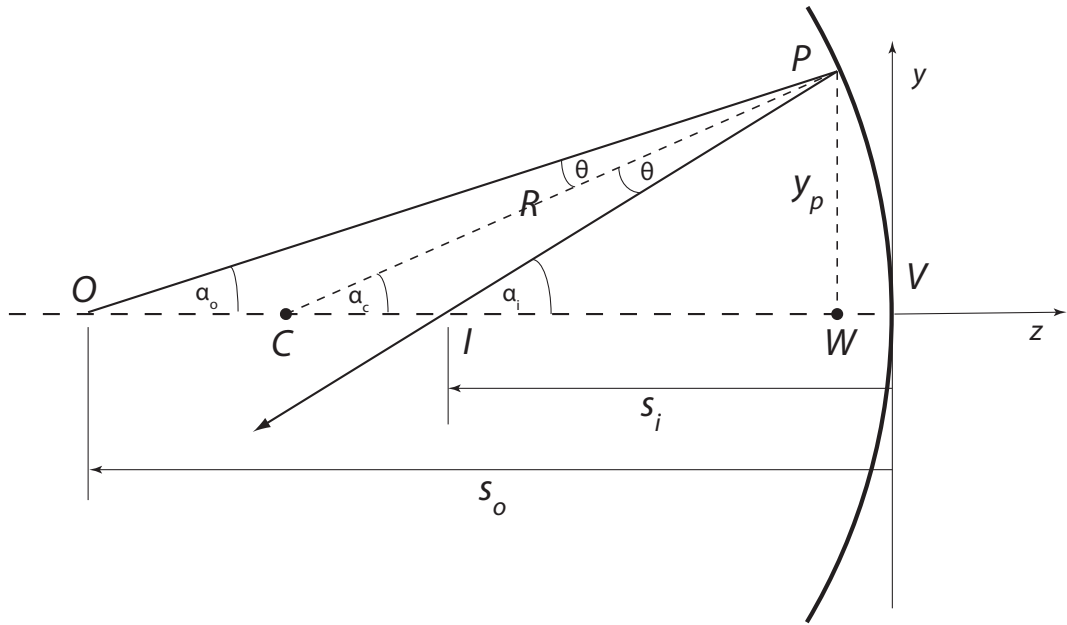


Figure 6.1: Reflection from a spherical surface. See text for details.

given that s_o is the distance between the mirror surface and the object, and s_i is the distance between the image and the mirror surface (both along the optical axis). The angle α_c is the angle between the line joining the center of the surface C and the point P and the optical axis.

If θ is the angle of incidence then we have, considering the triangles OPC and CPI that

$$\theta = \alpha_c - \alpha_o = \alpha_i - \alpha_c$$

or

$$2\alpha_c = \alpha_o + \alpha_i$$

Substituting this into the first three approximations for the angles we derive

$$\frac{2}{R} = \frac{1}{s_o} + \frac{1}{s_i} = \frac{1}{f} = -P.$$

The distance $R/2$ is termed the *focal length* of the mirror, often written f , while the *power* of the surface is written P . Note that as the object distance s_o goes to ∞ the image distance s_i goes to f .

6.1.4 Refraction in lenses

Snell's law of refraction is also a good starting point for understanding lenses. Given that all angles are small, indices of refraction n_1, n_2 and a radius of curvature R_{12} , Snell's law implies that

$$\frac{n_2}{s_2} - \frac{n_1}{s_1} = \frac{(n_2 - n_1)}{R_{12}}.$$

(note here that s_1 is negative). If we take the focal length f to be the value of s_2 when s_1 approaches infinity we have

$$f_2 = \frac{n_2 R_{12}}{(n_2 - n_1)}$$

Thus, for refraction, the paraxial equation for image and object distances is

$$\frac{n_2}{s_2} - \frac{n_1}{s_1} = \frac{n_2}{f_2} = -\frac{n_1}{f_1} = P_{12}$$

where P_{12} is the *power* of the surface. The power, like the focal length, measures how strongly converging (or diverging for negative P) an interface is. A plane has zero power.

For a lens in air (or vacuum) we can set $n_1 = 1$ and $n_2 = n$ giving the ratio of the speed of light in vacuum/air to the speed of light in glass, *i.e.* $n = c/c_g$. Snell's law implies that a plane wave front in vacuum/air remains plane as light enters the glass. A typical value for glass is 1.5, so the speed of light in glass is some 200 000 km/s. Since the frequency of light does not change, this means that the wavelength of light is shorter in glass than in vacuum.

An imaging lens is constructed so that the optical length w in all rays is identical even if the geometric distances are different.

6.1.5 Imaging properties

The relation between the distance from a thin lens to an object s and to the image of the object s' is related to the focal length f of the lens by the thin lens formula

$$\frac{1}{s} + \frac{1}{s'} = \frac{1}{f}$$

Note that a point infinitely far away is imaged at the focal point of the lens, *i.e.* that for $s \rightarrow \infty$ then $s' = f$.

Evaluating an optical design is best done by *ray tracing*, *i.e.* by tracing the path of several rays from an object through all the optical elements until they form a final image. This is usually done with a computer program that follows a number of rays, applying Snell's laws and/or the laws of reflection at every interface — usually employing more exact formulations than the paraxial approximation. However, using the paraxial approximation we can get a (useful!) rough estimate using only a ruler, paper and a pencil. *Graphical ray tracing* uses the following specific rules for a thin lens:

1. Rays incident parallel to the axis emerge through the right focal point.
2. Rays incident through the left focal point emerge parallel to the axis.
3. Rays through the vertex do not change direction.

Likewise, when dealing with a spherical mirror

1. Incident rays parallel to the optical axis are reflected through the focal point, F .
2. Incident rays through the focal point are reflected parallel to the axis.
3. Incident rays that reach the vertex are reflected back at an equal and opposite angle.
4. Incident rays through the center of curvature, C , are reflected back upon themselves.

6.1.6 Simple telescopes

In its simplest form an astronomical telescope consists of two parts, an objective and an eyepiece. The objective images the object one is studying, and which is “infinitely” far away (parallel rays in) on the focal point or focal plane. This image is real, and can be seen if one places a screen in the focal plane. An eyepiece beyond the focal point functions as a magnifying glass. These two elements form the basic telescope (see figure 6.2).

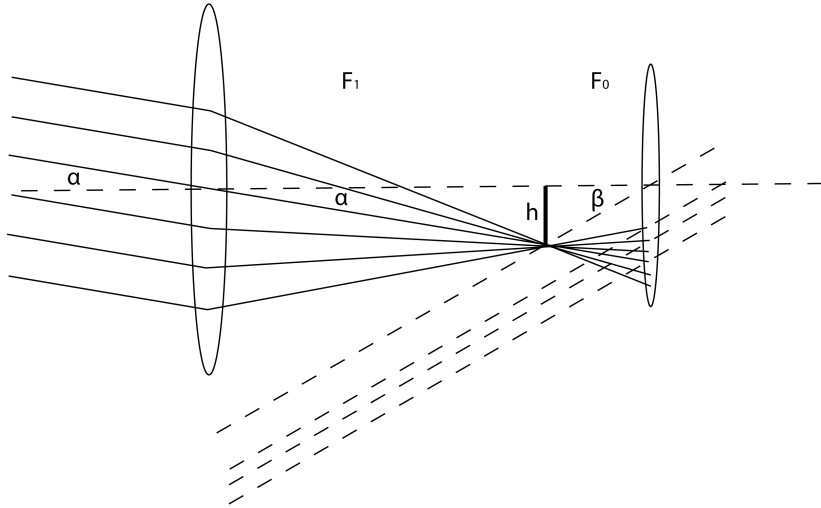


Figure 6.2: Schematic telescope design. Object has angular size α and is focused by the primary lens with focal length F_1 . Image is observed using the eyepiece adjusted so as to give a virtual image at infinity. The focal length of the eyepiece is F_0 .

The *image scale*, s , describes the mapping of the sky by any camera. The image scale is the angular distance on the sky that corresponds to a unit linear distance in the focal plane of the camera. Given a focal length f , draw paths followed by two rays, one from a point (*e.g.* a star) on the optical axis, the other from a point separated from the first by a small angle θ on the sky. Rays pass through the vertex without deviation, so assuming the paraxial approximation, $\theta \approx \tan \theta$, it is clear that

$$s = \frac{\theta}{y} = \frac{1}{f}$$

where y is the distance the points are separated in the focal plane. Typical focal plane detectors are composed of many identical pixels. If the center of each pixel is separated from its nearest neighbors by d then the *pixel scale* of a telescope is just $s_p = sd$.

The *focal ratio* is defined as

$$\mathcal{R} = \frac{f}{D}$$

where D is the diameter of the entrance aperture of the telescope. One can show that the brightness (energy per unit area to the focal plane) is proportional to \mathcal{R}^2 .

The magnification M of a telescope is given by considering that the image formed by an object at an angle of α (assumed small) to the optical axis. The real image is in focus at distance F_1 , where F_1 is the focal length of the objective lens, since the object is very far away. This image is observed by the eyepiece adjusted so as to give a virtual image at

infinity, *i.e.* the eyepiece should be a distance F_0 away from the image formed by the objective. Considering the geometry of the system shown in figure 6.2 we see that the magnification M must be given by $M = \beta/\alpha$ and that therefore

$$M = \frac{\beta}{\alpha} = \frac{\tan(h/F_0)}{\tan(h/F_1)} \approx \frac{h/F_0}{h/F_1} = \frac{F_1}{F_0}.$$

Note that the image is formed upside down.

6.2 Optical Materials

An ideal mirror should have a reflectivity of 1.0 for all wavelengths (λ) of interest. The substrate should be easy to shape to an accuracy of a fraction of λ , and once shaped, should be mechanically and chemically stable. Low mass is a virtue, as mirrors and lenses should be as large as possible and must be mobile. Since the temperature can change rapidly high thermal conductivity and a low coefficient of thermal expansion are also essential.

For reflecting telescope's first two centuries, one used *speculum metal*, an alloy primarily of copper and tin. However, it was (is) heavy and only has 45% reflectivity at best, and tarnishes easily. Astronomers therefore switched to silvered glass mirrors once the technology became available in the 1880s. Most modern mirrors generally use substrates made with special glasses (*e.g.* Pyrex) or ceramics (Cervit or Zerodur) that have low coefficients of thermal expansion. A coating of Al is best for the near ultraviolet and optical since Al is durable and cheap. Ag is poor in the ultraviolet, is superior to Al when $\lambda > 450$ nm. Au is best in the infrared for $\lambda > 650$ nm. Be is toxic, but is the lowest density workable metal with very good rigidity.

Short wavelengths, extreme ultraviolet (EUV) and shorter, present difficulties: First energetic photons tend to be absorbed, scattered, or transmitted by most materials, and second, curved mirrors in general need to be shaped with an accuracy of at least $\lambda/4$, which for a 1 nm X-ray, amounts to one atomic diameter! X-Ray and EUV focusing telescopes are therefore often designed to operate with grazing incidence as discussed later.

Transmitting materials form lenses, windows, correctors, prisms, filters, fibres, and more. Of primary relevance are index of refraction, dispersion, and absorption. The index of refraction for a number of glasses as a function of wavelength λ is shown in table 6.1. Generally glasses with a high index of refraction will also have high dispersion and are called “flints”, while those with smaller index and dispersion are called “crowns”.

In ultraviolet (150 nm – 400 nm) ordinary glasses become opaque, fused quartz (SiO_2) is the exception. All other ultraviolet transmitting materials are crystalline, rather than glass, and are more difficult to shape and more likely to chip and scratch. The most useful is perhaps calcium fluoride (CaF_2), which transmits from 160 nm to 7 μm . Other fluoride crystals have similar properties. Fused quartz and fluorides do not transmit well below 180 nm and some birefringent crystals, such as sapphire (Al_2O_3) can be used in the very far ultraviolet. Optics for $\lambda < 150$ nm must be reflecting and for $\lambda < 15$ nm only grazing incidence reflections are possible.

In the infrared ordinary glasses transmit to about 2.2 μm , and some special glasses to 2.7 μm . A large selection of crystalline materials, some identical to those used in the ultraviolet, transmit to much longer λ , but most are soft, or fragile, or sensitive to humidity, so can only be used in protected environments.

Glass type	Refractive index at the specified wavelengths (nm)				
	361	486	589	656	768
Crown	1.539	1.523	1.517	1.514	1.511
High dispersion crown	1.546	1.527	1.520	1.517	1.514
Light flint	1.614	1.585	1.575	1.571	1.567
Dense flint	1.705	1.664	1.650	1.644	1.638

Table 6.1: Index of refraction in various glass types vary as a function of wavelength and are thus dispersive.

Coating the surface of an optical element with a thin film can exploit the wave properties of light to increase, or decrease, its reflectance. A thin film exactly 1/4 wavelength thick applied to a reflecting substrate will introduce two reflected beams, one from the front film surface, and the other from film-substrate interface. The second beam will emerge one-half wavelength out of phase, and the two beams will destructively interfere. If the amplitudes are equal, the interference will be total. An antireflection coating works best at only one wavelength, but will to some extent also work for a broader band centered near the design wavelength. A similar technique can enhance the reflectivity of a surface and multiple layers of alternating high and low index materials can improve the reflectivity of a mirror over a broad range of mirrors. Such *multilayer mirrors* are in frequent use in solar satellites observing the sun at normal incidence in the EUV as will be discussed later.

6.3 Chromatic aberration

Chromatic aberration arises through the change in the refractive index of glass or other optical material with the wavelength. Typical values for some optical glasses are shown in table 6.1. The degree to which the refractive index varies with wavelength is called the dispersion, and is measured by the constringence ν

$$\nu = \frac{\mu_{589} - 1}{\mu_{486} - \mu_{656}} \quad (6.2)$$

where μ_λ is the refractive index of the wavelength λ . Note that the constringence (also called the *Abbe number*) is roughly inversely proportional to the dispersion, *i.e.* $(dn/d\lambda)$. The three wavelengths that are chosen for the definition of ν are those of strong Fraunhofer lines: the C-line 486 nm H β , the D lines 589 nm (Na), and the F-line 656 nm H α . The glasses listed above have constringence that varies from 57 for crown glass to 33 for the dense flint.

The effect of dispersion upon an image is to spread it out into a series of different colored images along the optical axis. Looking at this sequence of images with an eyepiece, then at a particular point along the optical axis, the observed image will consist of a sharp image in the light of one wavelength surrounded by blurred images of varying sizes in the light of all remaining wavelengths. To the eye, the best image occurs when yellow light is focused since it is less sensitive to red and blue light. The spread of colors along the optical axis is called the *longitudinal chromatic aberration*, while that along the image plane containing the circle of least confusion is called the *transverse chromatic aberration*.

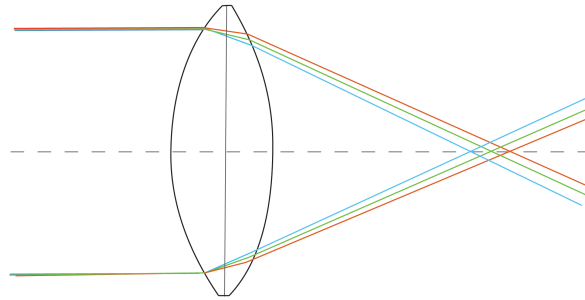


Figure 6.3: Chromatic aberration.

Delayed by Newton's declaration of impossibility, in the 1760s in France and England it was discovered that two (or more) lenses can be combined to reduce the effect of chromatic aberration. Commonly a biconvex crown glass lens is combined with a planoconcave flint glass lens to produce an *achromatic doublet*. This can reduce the chromatic dispersion by a factor 30. If the radii of the curved surfaces are all equal, then the condition for two wavelengths, λ_1 and λ_2 , to have coincident images is

$$2\Delta\mu_C = \Delta\mu_F$$

where $\Delta\mu_C$ and $\Delta\mu_F$ are the differences between the refractive indices at λ_1 and λ_2 for the crown glass and flint glass respectively. More flexibility in the design can be achieved if the two surfaces of the converging lens have differing radii. Then the condition for achromatism is

$$\frac{|R_1| + |R_2|}{|R_1|} \Delta\mu_C = \Delta\mu_F$$

where R_2 is the radius of the surface of the crown glass that is in contact with the flint lens and R_1 is the radius of the other surface of the crown glass lens. Fraunhofer perfected the design and construction of achromats which led to the possibility of making large refractors, which became the telescope design of choice at most observatories after the 1820s. The era of the refractor came to an end around 1900 when the size of these reached roughly 1 m, above which size gravity deforms the shape of the lens. It is interesting to note that the Swedish 1-meter Solar Telescope with a 1.0 m lens is one of the worlds largest refractors.

Since photographic film has a different wavelength sensitivity than the human eye, achromats had to be redesigned when photographic technology was adopted by astronomers in the 1880s.

It is possible to design doublets so that three or more wavelengths are corrected, in this case the corrective lenses are called *apoachromats*. Adding more lenses, a properly designed *triplet*, called a *superapoachromat* can bring four wavelengths into a common focus.

6.3.1 Schupmann achromat

Another interesting solution to the problem of achieving an achromatic image is the combination of a positive lens and a second negative lens in which case one has an intermediate image and the final image is virtual. This is named a Schupmann lens. The drawback of the virtual image location can be overcome with the help of a mirror. The collecting mirror is placed behind the negative lens, which is used twice and therefore has less power than the

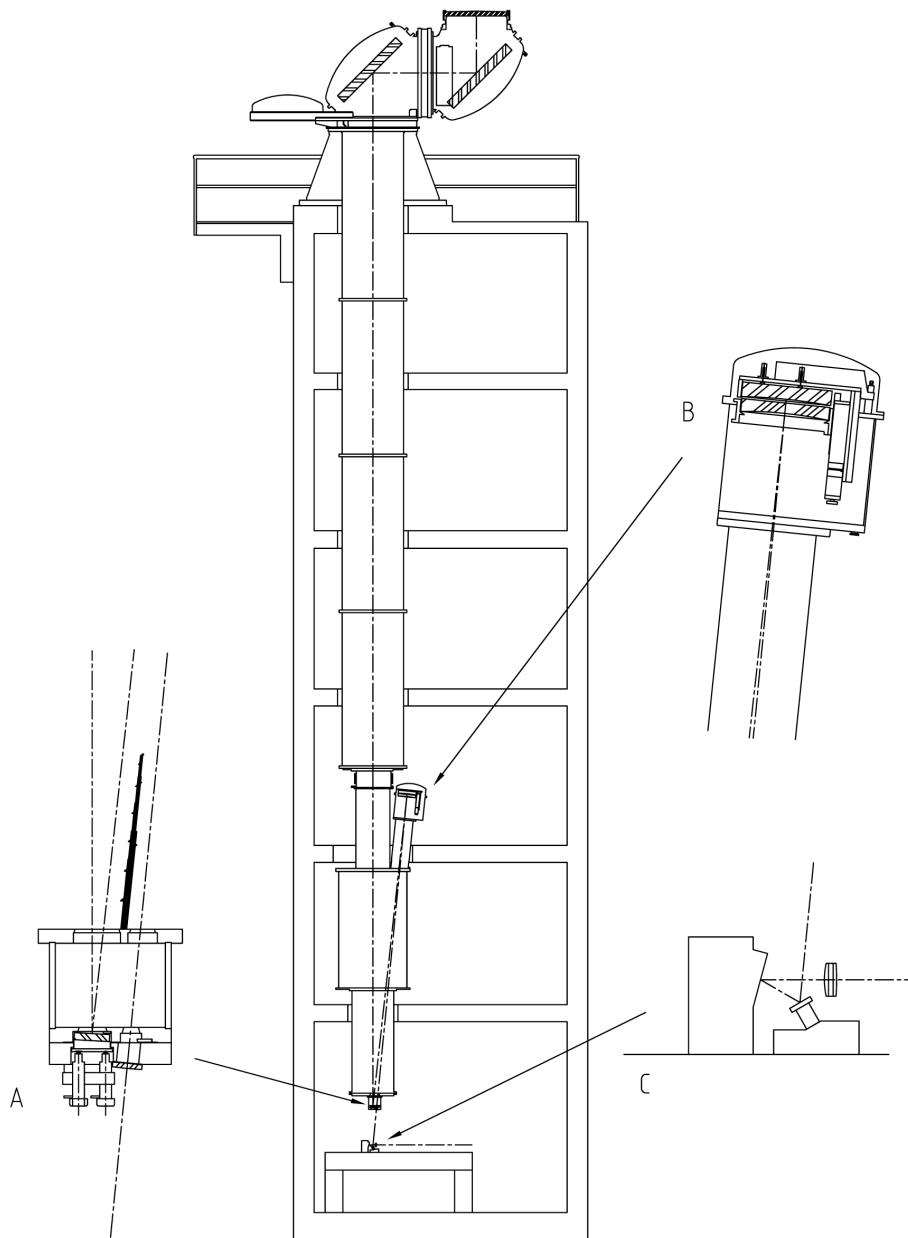


Figure 6.4: Schematic drawing of the Swedish 1-meter Solar Telescope tower with the turret and vacuum system (center drawing). Details of the box holding the field mirror and field lens are shown in A and the Schupmann corrector with one lens and one mirror in B. The re-imaging optics, located on the optical table and consisting of a tip-tilt mirror, an adaptive mirror and a re-imaging lens are shown in C.

negative lens in the usual setup. There are few refracting telescopes in professional night time astronomy, but the Swedish 1-meter Solar Telescope is a refracting telescope in which a Schupmann achromat is used.

6.4 Seidel Aberrations

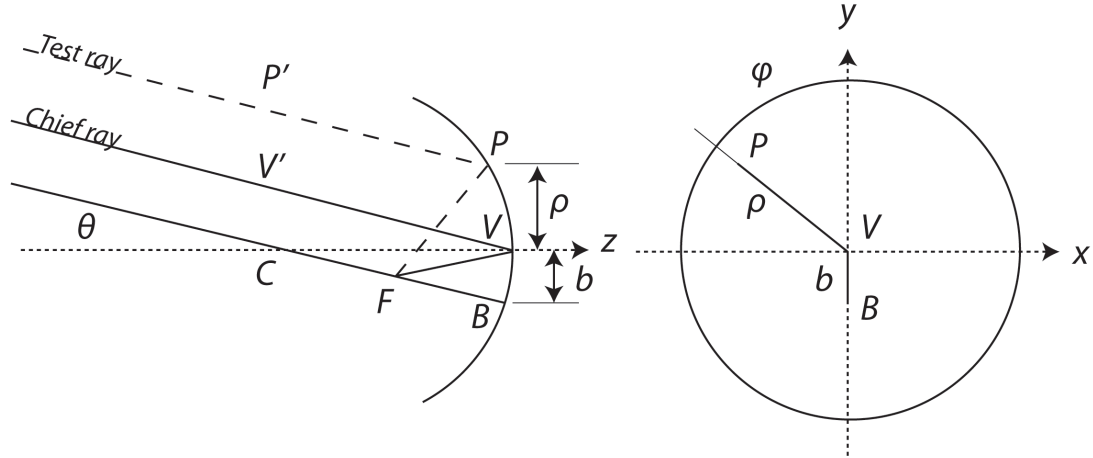


Figure 6.5: Geometry used in the Seidel aberration discussion. The left hand diagram shows rays through the center of curvature (CFB) and vertex (VV'), the chief ray), which along with the optical axis defines the meridional plane. Point P is outside the plane of the diagram. The right hand diagram locates points P, V, and B in the plane of the aperture when looking down the optical axis.

Consider a “perfect” telescope, it should transform an incident plane wavefront into a converging spherical wavefront whose center is the focus predicted by the paraxial approximation. For point sources off-axis the perfect telescope should produce spherical wavefronts converging somewhere on the image plane, also as predicted by the paraxial theory. Define the *chief ray* as the one passing from the object through the center of the entrance aperture. The plane containing this ray and the optical axis defines the *meridional* or *tangential plane*. The plane perpendicular to this plane is called the *sagittal plane*. If we now analyse the angles of reflection or refraction for a curved surface using the approximation

$$\sin \theta \approx \theta - \frac{\theta^3}{3!}$$

one obtains *third-order aberration theory* which is much more accurate than that given by paraxial theory where one assumes $\sin \theta = \tan \theta = \theta$. In this treatment one can show that the optical path *difference* between a test ray and the chief ray takes the form

$$\Delta w(\rho, \phi, b) = C_1 \rho^4 + C_2 \rho^3 b \cos \phi \quad (6.3)$$

$$+ C_3 \rho^2 b^2 \cos^2 \phi + C_4 \rho^2 b^2 + C_5 \rho b^3 \cos \phi \quad (6.4)$$

where the C_i values depend on the shapes of the optical surfaces and/or the indices of refraction. Each of the terms in this equation 6.3 has a different functional dependence, so one distinguishes five monochromatic third-order aberrations which are also known as the *Seidel aberrations*. Note that since the range of ρ depends on the diameter of the telescope the terms with the highest order of ρ are the most important.

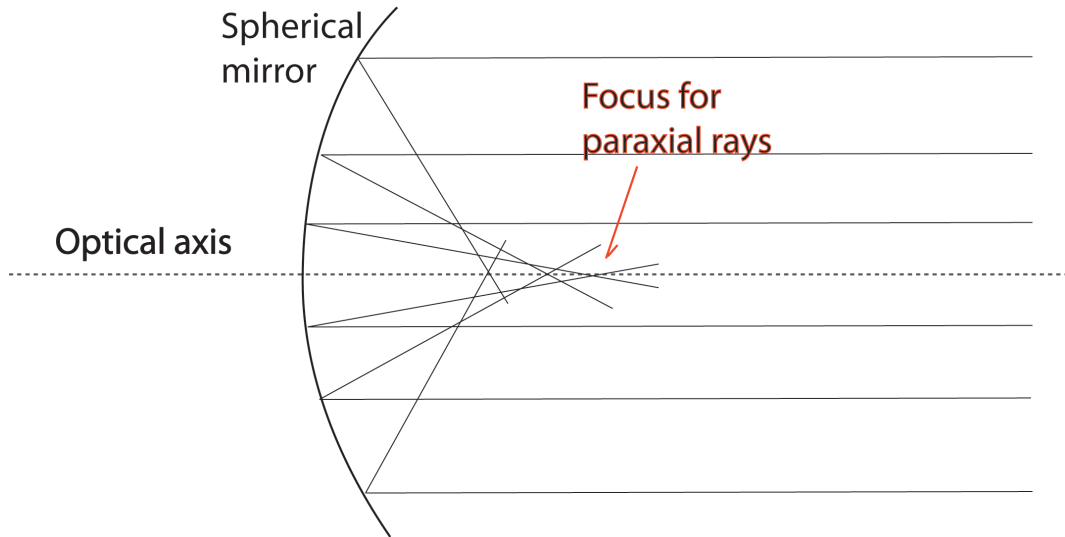


Figure 6.6: Spherical aberration.

6.4.1 Spherical aberration $\propto \rho^4$

A common and severe aberration of both lenses and mirrors is *spherical aberration*: annuli of the lens or mirror that are of different radii have different focal lengths. It is possible to minimize but not eliminate spherical aberration by minimizing the angles of incidence on every surface. Likewise, any lens with a large enough focal ratio will approach the paraxial case closely enough that the blur due to spherical aberration can be made smaller than the seeing disk. Since a large focal ratio also minimizes the chromatic aberration, early refracting telescopes (1608 – 1670) tended to have moderate apertures and large focal lengths, at the cost of reduced image brightness and unwieldy telescope length.

For mirrors, removing spherical aberration is simple. A paraboloid reflector, made by deepening the sphere to a paraboloidal surface, will display no on-axis aberrations at all — rays from infinity parallel to the axis will all come to the same focus. Newton constructed the first workable reflecting telescope in 1668, and reflecting telescopes were fashionable from the 1780s (when the Herschels were making great discoveries with speculum paraboloids) until the superiority of the refractor became apparent in the 1830s as a result of the discovery that an achromatic doublet can be designed to minimize both chromatic aberration and spherical aberration: These cannot be eliminated from a simple lens without using aspheric surfaces, but can be reduced for a given focal length by adjusting the shape factor q

$$q = \frac{R_2 + R_1}{R_2 - R_1}$$

where R_1 and R_2 are the radii of the first and second surfaces of the lens respectively. Judicious choice of surface radii in an achromatic doublet can lead to some correction of spherical aberration while still retaining the color correction.

It is also possible to remove spherical aberration from a *spherical* mirror by the use of a transparent corrector plate, as we will discuss in connection with Schmidt and Maksutov telescopes later in this lecture.

6.4.2 Coma $\propto \rho^3 b \cos \phi$

Coma in an optical system refers to an aberration which results in off-axis point sources such as stars appearing distorted. Specifically, coma is defined as a variation in magnification over the entrance pupil. Coma is an inherent property of telescopes using parabolic mirrors, thus deepening a spherical mirror in order to correct spherical aberration will introduce coma. It causes the images for objects away from the optical axis to consist of a series circles that correspond to the various annular zones of the lens or mirror and which are progressively shifted away from the optical axis. The severity of the coma is proportional to the square of the aperture and the angular size of the blur is given by

$$L = A \frac{bD^2}{f^3} = A\theta\mathcal{R}^{-2}$$

where A is a constant that depends on the shape of the surface.

Lenses or mirrors in which both spherical aberration and coma are minimized at a single wavelength are called best form or *aplanatic*. No single element aplanatic telescope is possible, either in a reflector or a refractor. As with spherical aberration, a large focal ratio will reduce coma, but impose penalties in image brightness and telescope length. Otherwise, minimizing coma in a refracting system requires a system of lenses, and at least two mirrors in reflecting telescopes.

6.4.3 Astigmatism $\propto b^2 \rho^2 \cos^2 \phi$

Astigmatism

Different focal planes.

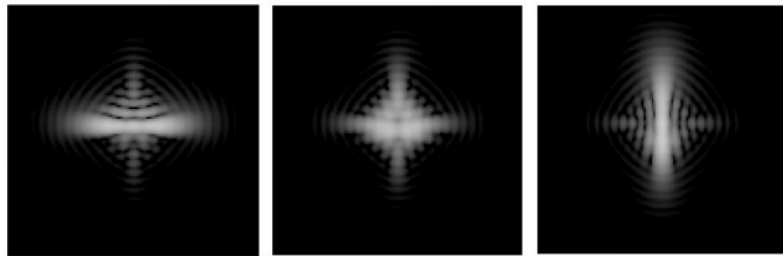


Figure 6.7: Example of the effect of astigmatism.

Astigmatism is an effect where the focal length differs for rays in the plane containing an off-axis object and the optical axis (tangential plane), in comparison with rays in the plane at right angles to this (sagittal plane). An example of astigmatism is shown in figure 6.7. The angular dependence suggests that the wavefront distortion is zero for rays in the sagittal plane (*i.e.* $\phi = 90^\circ, \phi = 270^\circ$), but an extremum for rays in the meridional plane.

The blurred image suffering astigmatism has an angular length

$$L = B\theta^2\mathcal{R}^{-1}$$

where B is a constant that depends on the shape of the reflecting or refracting surface.

It is possible to correct astigmatism, but at the expense of introducing an aberration called field curvature, *i.e.* that the surface containing the sharply focused image is not flat but curved. A system where a flat image plane is combined with corrected astigmatism is termed *anastigmatic* and a telescope that corrects for astigmatism, coma, and spherical aberration a anastigmatic aplanat.

6.4.4 Field curvature $\propto \rho^2 b^2$

This aberration results from off-axis images falling on a spherical surface called the *Petzval surface*. Detectors are generally flat, so much of an image formed on a detector will be out of focus. For a small detector, this defocus will not exceed the seeing disk or diffraction limit and therefore not be a problem. For larger detectors is to bend the detector to fit the Petzvel surface, as was done with photographic plates using a mechanical plate holder. Large solid-state detectors like CCDs are mechanically quite fragile, so bending is not an option. In which case a corrector plate or lens is used to flatten the field.

6.4.5 Distortion $\propto \rho b^3 \cos \phi$

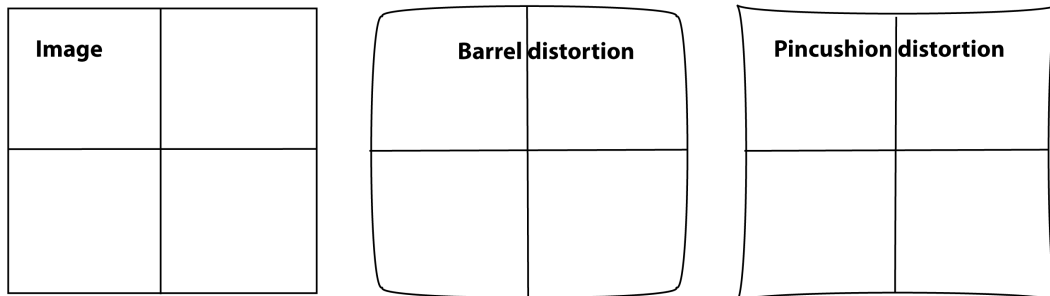


Figure 6.8: Distortion

The final aberration is *distortion*, which is a variation in the magnification over the image plane. A distorted system will deliver images that suffer *pincushion* or *barrel* distortion according to whether the magnification increases or decreases with distance from the optical axis.

Since distortion does not change the image quality, it can be removed from digital in a post processing phase.

Another fault of optical systems is called *vignetting*. It arises as a result of uneven illumination of the image plane, usually due to the obstruction of the light path by parts of the instrument.

6.4.6 Zernike polynomials

In an optical system the location of the diffraction focus will depend on the type and magnitude of aberration present. Because of this dependence, it is appropriate to restructure the classical aberration terms and include explicitly the required image shift to place the diffraction focus at the origin. These modified terms are called the orthogonal aberrations,

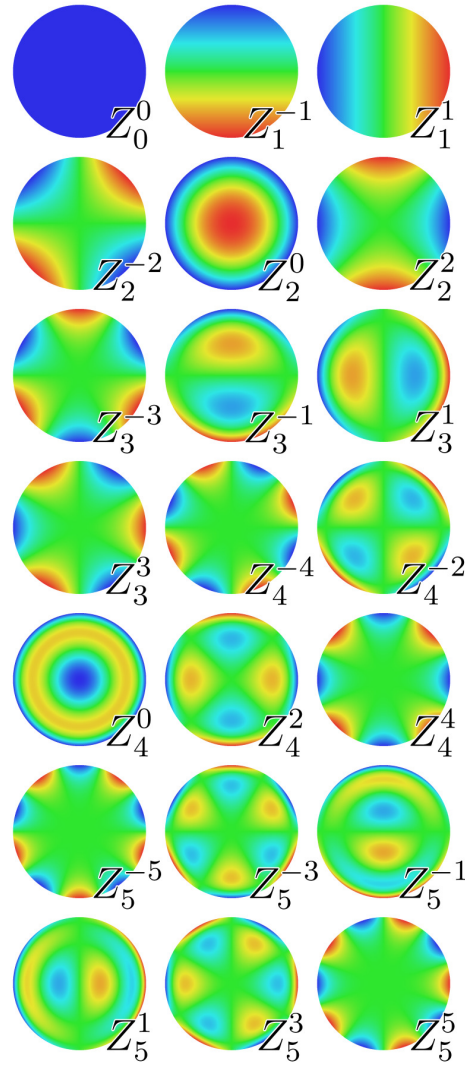


Figure 6.9: The first few Zernike polynomials, see table 6.2

with polynomials in ρ and φ (*i.e.* using a circular co-ordinate system) called *Zernike polynomials*. Developed by Frits Zernike in the 1930s, Zernike's polynomials are orthogonal over a circle of unit radius. A complex, aberrated wavefront profile may be curve-fitted with Zernike polynomials to yield a set of fitting coefficients that individually represent different types of aberrations. Their advantage are the simple analytical properties which leads to closed form expressions of the two-dimensional Fourier transform in terms of Bessel functions. Their disadvantage, in particular for high n is the unequal distribution of nodal lines over the unit disk, which introduces ringing effects near the perimeter $\rho \approx 1$, which leads attempts to define other orthogonal functions over the circular disk¹.

¹For atmospheric turbulence Zernike polynomials are not the optimal set of basis functions because the Zernike coefficients are statistically dependent. Basis functions that do not have this property can be constructed and are called the *Karhunen–Loéve functions* which represent stochastic processes as an infinite linear combination of orthogonal functions analogous to a Fourier series representation of a function on a bounded in-

Zernike polynomials	Roles of the Zernike polynomials
a_0	“Piston”, equal to the mean value of the wavefront
$a_1 \times \rho \cos(\varphi)$	“X-tilt”, deviation of the overall beam in the sagittal direction
$a_2 \times \rho \sin(\varphi)$	“Y-tilt”, deviation of the overall beam in the tangential direction
$a_3 \times (2\rho^2 - 1)$	“Defocus”, a parabolic wavefront resulting from being out of focus
$a_4 \times \rho^2 \cos(2\varphi)$	“X-astigmatism”, horizontally oriented cylindrical shape
$a_5 \times \rho^2 \sin(2\varphi)$	“Y-astigmatism”, vertically oriented cylindrical shape
$a_6 \times (3\rho^2 - 2)\rho \cos(\varphi)$	“X-coma”, comatic image flaring in the horizontal direction
$a_7 \times (3\rho^2 - 2)\rho \sin(\varphi)$	“Y-coma”, comatic image flaring in the vertical direction
$a_8 \times (6\rho^4 - 6\rho^2 + 1)$	“Third order spherical aberration”

Table 6.2: ρ is the normalized pupil radius, φ is the azimuthal angle around the pupil, the coefficient a_0, \dots, a_8 are the wavefront errors in wavelengths.

There are even and odd Zernike polynomials. The even ones are defined as

$$Z_n^m(\rho, \varphi) = R_n^m(\rho) \cos(m\varphi)$$

and the odd ones

$$Z_n^{-m}(\rho, \varphi) = R_n^m(\rho) \sin(m\varphi)$$

where m and n are non-negative integers with $n \geq m$, φ is the azimuthal angle and ρ is the normalized radial distance. The radial polynomials R_n^m are defined as

$$R_n^m(\rho) = \sum_{k=0}^{(n-m)/2} \frac{(-1)^k (n-k)!}{k! [(n+m)/2 - k]! [(n-m)/2 - k]!} \rho^{n-2k} \quad \text{if } n - m \text{ even}$$

$$R_n^m(\rho) = 0 \quad \text{if } n - m \text{ odd}$$

The first few Zernike polynomials are described in table 6.2.

6.5 Practical telescopes

Even after a telescope design has been perfected; in which one attempts to remove as many of the aberrations as possible from the list above, there remains the task of physically producing the instrument specified. This must be done taking into consideration what one actually needs to observe in order to meet a certain scientific goals.

Manufacturing of lenses and mirrors is broadly similar: the surface is roughly shaped by moulding or diamond milling. It is then matched to another surface formed in the same material whose shape is inverse, called the *tool*. The two surfaces are ground together with coarse carborundum or other grinding powder between them until the required surface begins to approach its specifications. The pits left behind are removed by a second grinding stage

terval. The coefficients in the Karhunen–Loéve theorem are random variables and the expansion basis depends on the process. The Karhunen–Loéve transform adapts to the process in order to produce the best possible basis for its expansion. (Source: Wikipedia and Gua-ming Dai *Modal compensation of atmospheric turbulence with the use of Zernike polynomials and Karhunen-Loéve functions* J.Opt.Soc.Am. 12, October 1995.)

in which finer powder is used. A third stage follows, and so on. As many as eight or ten such stages may be necessary. When grinding pits are reduced to a micron or so in size, the surface may be polished. Once the surface has been polished it can be tested for accuracy of fit. A third stage termed *figuring* is often necessary when the surface is not within specification.

There are a number of tests that can determine the shape of a mirror's surface to within ± 50 nm or better, such as Foucault, Ronchi, Hartmann and Null tests.

Epicyclic grinding. Larger mirrors are ground by using large machines that move the tool in an epicyclic fashion. The motion of the tool is similar to that of the planets under the Ptolemaic model of the solar system. The epicyclic motion can be produced by a mechanical arrangement, but commercial production of large mirrors is now largely done by computer controlled planetary polishers.

Stressed polishing. The mirror segments for large instruments such as the 10 m Keck or Gran Tecan telescopes are small, off-axis parts of the total hyperbolic shape. These are produced by so-called stressed polishing where the blank is deformed by carefully designed forces from a warping harness, and then polished to a spherical shape. When the deforming forces are released the blank springs into the required shape.

Numerically controlled diamond milling. The requirements for non-axisymmetric mirrors for segmented mirror telescopes and for glancing incidence x-ray telescopes have led to the development of numerically controlled diamond milling machines which can produce the required shaped and polished surface directly to an accuracy of 10 nm or better.

The defects in an image that are due to surface imperfections on a mirror will not exceed the Rayleigh limit if those imperfections are less than one eighth of the wavelength of the radiation for which the mirror is intended. The restriction on lenses is about twice as large as those of a mirror since the ray deflection is distributed over two faces.

The surface must normally receive its reflecting coating after production. The vast majority of astronomical mirror surfaces have a thin layer of aluminium evaporated on to them by heating aluminium wires suspended over the mirror inside a vacuum chamber. Other materials such as silicon carbide are sometimes used, especially for UV since the reflectivity of aluminium falls for < 300 nm. Aluminium initially has a reflectivity of 90 %, but this will fall to 75 % in the matter of months, hence realuminaization is needed regularly. Mirrors coated with suitably protected silver can achieve 99.9 % reflectivity in the visible, and this may be required as the total number of reflections becomes large.

Coefficient of thermal expansion. To avoid deformations of its shape it is essential that the coefficient of thermal expansion for a mirror is low. For glass it is of order 9×10^{-6} K $^{-1}$, for pyrex 3×10^{-6} K $^{-1}$, and for fused quartz 4×10^{-7} K $^{-1}$. Pyrex has been the favorite material up until the last 30 years when quartz or artificial materials such as 'CerVit' or 'Zerodur'. Another possibility is to use materials with a very high thermal conductivity, such as silicon carbide, graphite epoxy, steel beryllium, or aluminium. However, it can be very difficult to polish these materials as they have a relatively coarse crystalline surface.

Rigidity of mirrors, thin mirrors and honeycomb mirrors. Small solid mirrors can maintain their shape simply by mechanical rigidity. However, the thickness required for such rigidity scales as the cube of the size, so the weight of a solid mirror scales as D^5 — this quickly becomes too expensive to build. There are various ways to reduce the weight of mirrors, these fall into two major classes: thin mirrors and honeycomb mirrors. Thin mirrors are also subdivided into monolithic and segmented mirrors. In both cases active support is needed in order to maintain the correct shape. Honeycomb mirrors are thick solid blanks that have had a lot of the material behind the reflecting surface removed, leaving only thin struts to

support that surface.

Rotating mirrors, bath of mercury. Isaac Newton realized that the surface of a steadily rotating liquid would take up a paraboloidal shape under the combined forces of gravity and centrifugal acceleration. If the liquid reflects light, like mercury, gallium, gallium-indium alloy, or an oil suffused with reflecting particles, one can then use it as the primary mirror of a telescope.

6.5.1 Designs

The most common format for large telescopes is the Cassegrain system, although most large telescopes can be usually be used in several alternative different modes by interchanging the secondary mirrors. The Cassegrain is based on a paraboloidal primary and a convex hyperboloidal secondary. The major advantage of the Cassegrain lies in its telephoto characteristic, the secondary mirror serves to expand the beam from the primary mirror so that the effective focal length of the whole system is several times the that of the primary. A compact (thus cheap) mounting can thus be used to hold the optical elements while retaining the advantages of long focal length and large image scale. The Cassegrain is affiliated with coma and spherical aberration to about the same degree as an equivalent Newtonian.

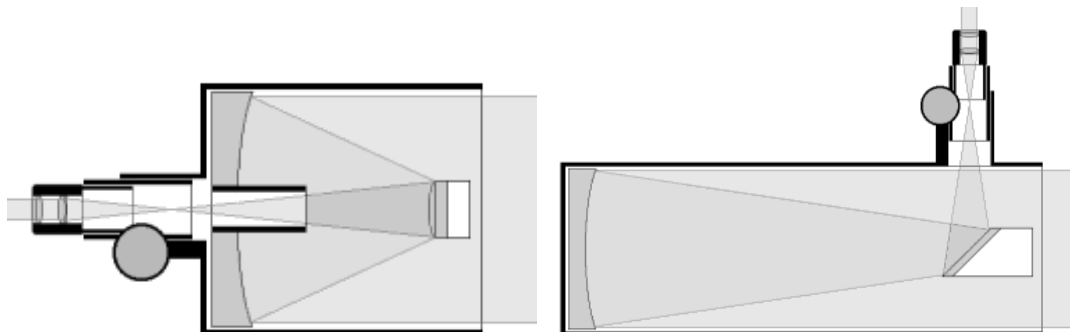


Figure 6.10: Cassegrain and Newtonian Designs

A great improvement of the Cassegrain can be achieved by a slight alteration to a Ritchey-Chrétien system. The optical arrangement is identical but for that the primary mirror is deepened to a hyperboloid and a stronger hyperboloid is used for the secondary. With this system both coma and spherical aberration can be corrected and one achieves a aplanatic system.

Corrector lenses just before the focus. One can also improve Cassegrain or Ritchey-Chrétien systems by adding correctors just before the focus. The correctors are low power lenses whose aberrations oppose those of the main system. The corrective optics may be combined with a focal reducer to enable the increased field of view to be covered by the detector array. A focal reducer is a positive lens, usually a apochromatic triplet, placed just before the focal point of the telescope that decreases the effective focal length and so gives a smaller image scale.

Coudé focus. Another related telescope design is the Coudé system, which in effect is a very long focal length Cassegrain or Ritchey-Chrétien whose light beam is folded and guided by additional flat mirrors to give a focus whose position is fixed irrespective of the telescope position. One way is to insert a diagonal mirror after the secondary, light is reflected down

the declination, and then down the polar axis by a second diagonal mirror. Light then always emerges from the end of the polar axis, whatever part of the sky the telescope is inspecting.

Nasmyth focus/system. With alt-ax mountings the light beam can be directed along the altitude axis to one of the two Nasmyth foci on the side of the mounting. These foci still rotate as the telescope changes azimuth, but this is still easier than changing the altitude and altitude of a conventional Cassegrain focus. Both of the fixed focus systems, Coudé and Nasmyth, are very advantageous when large equipment such as high dispersion spectrographs, are to be used. Disadvantages are that the field of view rotates as the telescope tracks an object across the sky, and is very small due to the large effective focal ratios that are required to bring the focus through the axes, and finally the additional reflections cause the loss of light.

The simplest of all designs is a mirror used at its prime focus. That is, the primary mirror is used directly to produce the images and the detector is placed at the top end of the telescope. The image quality of at the prime focus is usually poor even a few tens of arcsec away from the optical axis because the primary mirrors focal ratio may be as short as $f3$ or less in order to reduce the instrument length. A system that is almost identical to the use of a telescope at prime focus is the Newtonian. A secondary flat secondary mirror is used just before the prime focus. This reflects the light beam to the side of the telescope from where access to it is relatively simple. There is little advantage to this design over use of the prime focus for large telescopes. The images in a Newtonian system and at prime focus are very similar and are of poor quality away from the optical axis.

A Gregorian is similar to the Cassegrain except that the secondary is a concave ellipsoid and is placed after the prime focus. Since the primary mirror creates an actual image before the secondary mirror, the design allows for a field stop to be placed at this location, so that the light from outside the field of view does not reach the secondary mirror. This is a major advantage to solar telescopes, where a field stop can reduce the amount of heat reaching secondary mirror and subsequent components. Hinode/SOT (Solar Optical Telescope) is an example of a Gregorian.

Refractors (and the Swedish 1-meter Solar Telescope).

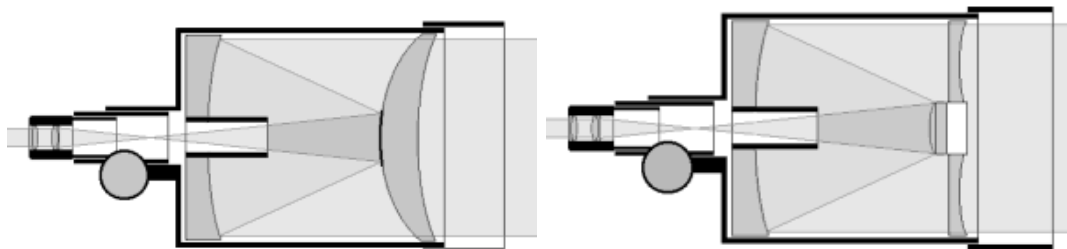


Figure 6.11: Maksutov and Schmidt-Cassegrain Designs

The catadioptric (from catoptric, *i.e.* reflecting, and dioptric, *i.e.* refracting) group of which the Schmidt camera is best known. A catadioptric system uses both lenses and mirrors in its primary light gathering section. Very high degrees of corrections of the aberrations can be achieved because of the wide range of variable parameters that become available. Diffraction limited performance over fields of view of several degrees is possible with focal ratios as fast as $f1.5$ or $f2$. The Schmidt camera cannot be used visually since its focus is inaccessible. One

of the best modifications of this is the Maksutov. A similar system is the Schmidt-Cassegrain telescope.

6.5.2 Mountings

The functions of a telescope mounting are to hold the optical components in their correct mutual alignment, and to direct the optical axis towards the object to be observed. One can consider the functions of the mounting under three separate aspects: supporting the optical components, preserving their correct spatial relationship, and acquiring and holding the object of interest in the field of view.

Equatorial mounting. This is a two axis mounting, with one axis, the polar axis, aligned parallel with the Earth's rotational axis, and the other, the declination axis, perpendicular to the polar axis. Only a single constant velocity motor is required to rotate the mounting around the polar axis in order to track an object.

Alt-az mounting. This mounting has motions in altitude and azimuth. Structurally it is much simpler and much more compact than the equatorial system. Its drawbacks are that the field of view rotates telescope motion, and that it needs driving continuously in both axes and with variable speeds in order to track an object.

Fixed position telescopes. Some telescopes do not track: *e.g.* transit telescopes point only along the meridian. Other telescopes do not vary their pointing at all and the tracking function is realized by moving the detector in the image plane while the massive telescope remains stationary.

Coelostat and heliostat. A coelostat is comprised of two flat mirrors that are driven so that a beam of light from any part of the sky is routed into a fixed direction. They are particularly used in conjunction with solar telescopes whose extremely long focal lengths make them impossible to move. One mirror of the coelostat is mounted on a polar axis and driven at half the sidereal rate. The second mirror is mounted and driven to reflect the light into the fixed telescope.

Mountings in space. Telescopes in space must also mount and track but since the effects of gravity are much less some aspects of these tasks is easier. In general two methods are used to stabilize the orientation of a telescope in space: small rockets and spinning reaction wheels. A space telescope often has more stringent pointing requirements than a telescope on the ground, and a guide star is often used to achieve this precision. To point on a given target requires continuous telescope movement because of the aberration of starlight induced by the telescopes orbital velocity and because of torques induced by atmospheric drag and thermal effects.

6.5.3 Telescopes in space

In connection with a RAND project in 1946, Lyman Spitzer was asked to consider the advantages of putting an astronomical telescope in space. This work came to full fruition in 1990 when the Hubble Space Telescope (HST) was launched. The HST has an aperture of 2.4 m and has generated unprecedented results, revolutionizing astronomy. Its replacement is meant to be the 6.5 m James Webb Space Telescope (JWST) built by NASA and ESA in collaboration and to be placed at the Sun-Earth L₂ Lagrange point in 2017 (or so).

The absence of an atmosphere and hence wavefront distortions means that a space telescope should have diffraction limited resolution. *I.e.* that the "diameter" of a star will be of

order the Airy disk

$$\theta = \frac{2.44\lambda}{D}$$

where λ is the wavelength observed and D the diameter of the telescope. Since there are no other distortions, the precision and alignment of optical surfaces becomes especially critical in space, where seeing will not mask any errors.

Note that the Earth's atmosphere is itself a source of background light, so from space the background is lower than on the ground. On the ground there are several sources: *airglow* (atomic and molecular line emission from the upper atmosphere), scattered sunlight, starlight and moonlight, and scattered artificial light. In the infrared, the atmosphere and telescopes both glow like blackbodies and dominate the background. From space the main contributor in the visible and in the near infra-red (NIR) comes from sunlight scattered from interplanetary dust (visible in dark sites on the ground as *zodiacal light*.) In the V band, the darkest background for the HST (near the ecliptic poles) is about 23.3 magnitudes/arcsec², while at the darkest ground based site it is of order 22.0 magnitudes/arcsec². In the thermal infrared the sky from space can be much darker than on the ground because it is possible to keep the telescope quite cold in space.

The atmospheric absorbs light at certain wavelengths, at these wavelengths it is only possible to observe from space. This is especially true for gamma-ray, x-ray, and UV astronomy, but also at other wavelengths: the atmosphere is a dynamic system and weather happens! Astronomers are often happy to achieve 1% accuracy on the ground, from space photometry precise to one part in 10⁵ is possible.

A space telescope in an orbit far enough away from the Earth (and the Moon) also has access to the entire sky all the time, half the sky is not blocked by the Earth at any given time, nor is a space telescope hindered by the day-night cycle or by moonlight.

A telescope on the ground experiences changing gravitational stresses as in points in different directions, and will respond by changing shape. Stresses induced by wind and temperature changes generate similar problems. Most of the expense of a large modern telescope is not in the optics, but in the systems needed to move and shelter the optics, while maintaining figure and alignment.

However, the total optical/infrared aperture on the ground exceeds that in space by a factor of at least 200, and that factor is likely to increase in the near future. The disadvantages of space astronomy are led by its enormous cost. Typically the two 8 m Gemini telescopes had a construction budget of 100 MUSD, the 2.4 m HST cost 2000 MUSD to construct and launch.

6.5.4 Observatory engineering

1. The location of an observatory is vital to its success. Seeing is substantially better at high altitude on isolated islands like Mauna Kea and La Palma and the various sites in northern Chile.
2. Lightweight mirrors in a compact structure are cost effective. Modern primary mirrors have fast focal ratios: f/1.75 for Keck, f/3.3 for Hale, which means shorter telescope length and a smaller building. The same is true for altazimuth mounts compared to equatorial mounts.
3. Active optics can improve image quality.

4. Local climate control can improve natural seeing. Structures that permit substantial airflow with *e.g.* fans, louvres, retractable panels, while still protecting from wind buffeting can improve seeing appreciably.
5. Novel focal arrangements can reduce costs of specialized telescopes. Keck and VLT can combine beams from several telescopes at a common focus (*i.e.* interferometry).
6. Adaptive optics can eliminate some of the effects of atmospheric seeing.

6.5.5 Future telescopes

If adaptive optics can produce a large diffraction limited FOV, then current mirror and mounting technology can allow telescopes of up to 100 m diameters. At present (2010) there are three serious multinational projects to build single aperture telescopes larger than the currently operational 8 – 11 m instruments. All three projects expect to see first light around 2018; and include the European Extremely Large Telescope (www.eso.org/sci/facilities/eelt) with a primary of $D = 42$ m built up of 1000 1.4 m segments, the Giant Magellan Telescope (www.gmto.org) $D = 24.5$ m of 7 8.4 m segments, and the Thirty Meter Telescope (www.tmt.org) $D = 30$ m consisting of 492 1.4 m segments. Each of these telescopes has a cost of some 10^9 US dollars.

6.6 Exercises

1. Show that Snell's law and the law of reflections follow from Fermat's principle. (Hint: set up an expression for the optical path length between two points as a function of, for example x and y , and minimize the expression, *i.e.* find $d/dy = 0$, keeping the positions $x_{1,2}$ constant.)
2. Make a figure showing the ray tracing of the image of an arrow (lying in the plane of the sky) through:
 - (a) A thin lens.
 - (b) A spherical mirror.

Use the appropriate rules for ray tracing in these separate cases. Indicate in both cases the positions of the object (the arrow), the focal points, and the image of the arrow.

3. What is the image scale expressed in arcsec per unit lenght?

Chapter 7

Diffraction II

7.1 Fresnel diffraction

Let us now continue our discussion of diffraction by considering the Fresnel regime, where the aperture is much larger than the Fresnel length $r_F = (\lambda r)^{1/2}$ and there is a large phase variation over the aperture. Specialize to incoming wave vectors that are approximately orthogonal to the aperture and to small diffraction angles so that we can ignore the obliquity factor. In contrast to the Fraunhofer case, identify \mathcal{P} by its distance z from the aperture plane, instead of its distance r from the aperture center, and use as integration variable in the aperture $\mathbf{x}' \equiv \mathbf{x} - r\theta$ (see figure 7.1).

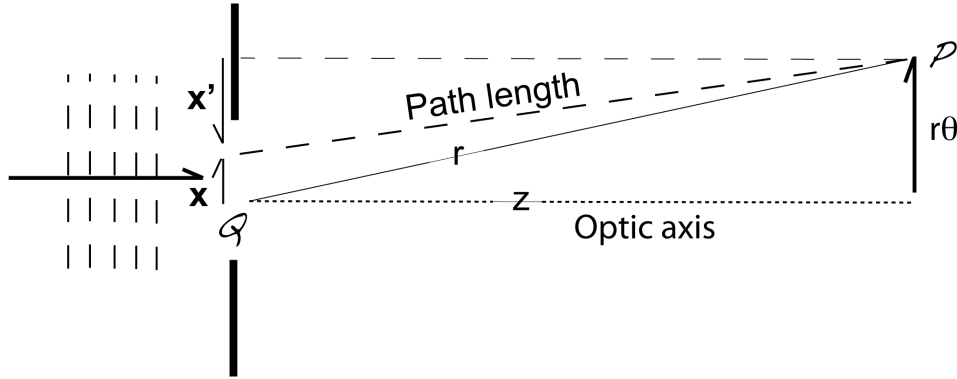


Figure 7.1: Geometry for computing the path length between a point Q in the aperture and the observation point \mathcal{P} . The transverse vector \mathbf{x} is used to identify Q in the Fraunhofer analysis and \mathbf{x}' is used for Fresnel analysis.

We can then write the dependence of the phase at \mathcal{P} on \mathbf{x} in the form

$$\Delta\phi \equiv k \times [(\text{path length from } \mathbf{x} \text{ to } \mathcal{P}) - z] = \frac{k\mathbf{x}'^2}{2z} + O\left(\frac{kx'^4}{z^3}\right)$$

In the Fresnel regime the term quadratic in \mathbf{x} is significant, and this is the reason the new variable \mathbf{x}' has been introduced is to simplify this expression.

As in the case of Fraunhofer diffraction, let us consider the diffraction pattern formed by a simple aperture of arbitrary shape, illuminated by a normally incident plane wave. It is

convenient to use Cartesian coordinates (x', y') and to define

$$s = \left(\frac{k}{\pi z} \right)^{1/2} x', \quad t = \left(\frac{k}{\pi z} \right)^{1/2} y'.$$

Notice that $(k/\pi z)^{1/2}$ is $\sqrt{2}/r_F$. Since we are assuming that the light is nearly orthogonal to the aperture we set the obliquity factor to one, and we can therefore rewrite (see lecture notes 5)

$$\psi_P = -\frac{ik}{2\pi} \int_Q d\mathbf{S} \cdot \left(\frac{\mathbf{n} + \mathbf{n}'}{2} \right) \frac{e^{ikr}}{r} t \psi'$$

to

$$\psi_P = -\frac{ik e^{ikz}}{2\pi z} \int_Q e^{i\Delta\phi} \psi_Q dx' dy' = -\frac{i}{2} \int \int e^{i\pi s^2/2} e^{i\pi t^2/2} \psi_Q e^{ikz} ds dt.$$

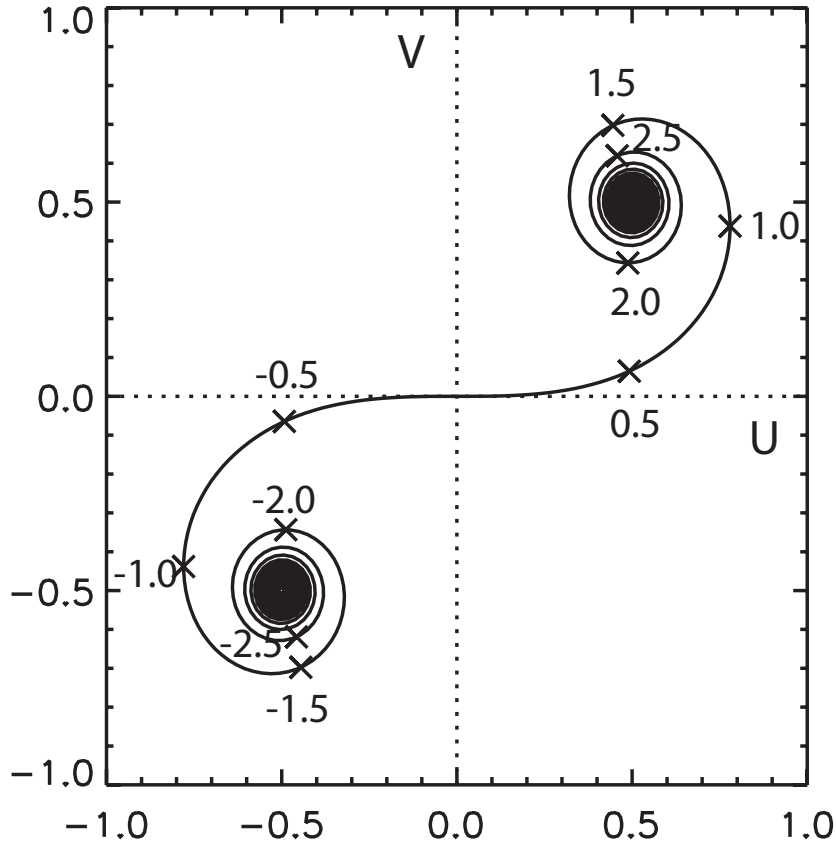


Figure 7.2: The Cornu Spiral showing the behaviour of the Fresnel integrals $U(\xi)$ and $V(\xi)$.

The expression above is quite general. Let us here concentrate on the Fresnel diffraction pattern for an incoming plane wave that falls perpendicularly on the aperture, so ψ_Q is constant over the aperture. Let us also confine ourselves to a rectangular aperture, with edges along the x' and y' directions. Then the two integrals have limits that are independent of each other and that can be expressed in the form $S(s_{max}) - S(s_{min})$ and $S(t_{max}) - S(t_{min})$ so

$$\psi_{\mathcal{P}} = \frac{-i}{2} [S(s_{max}) - S(s_{min})][S(t_{max}) - S(t_{min})] \psi_{\mathcal{Q}} e^{ikz} \equiv \frac{-i}{2} \Delta S_s \Delta S_t \psi_{\mathcal{Q}} e^{ikz}, \quad (7.1)$$

where the arguments are the limits of integration and where

$$S(\xi) \equiv \int_0^{\xi} e^{i\pi s^2/2} ds \equiv U(\xi) + iV(\xi)$$

with

$$\begin{aligned} U(\xi) &= \int_0^{\xi} ds \cos(\pi s^2/2) \\ V(\xi) &= \int_0^{\xi} ds \sin(\pi s^2/2) \end{aligned}$$

The real functions $U(\xi)$ and $V(\xi)$ are known as the *Fresnel integrals*.

The Fresnel integrals can be exhibited graphically using the *Cornu spiral*, which is a graph of the parametric equation $[U(\xi), V(\xi)]$, or equivalently a graph of $S(\xi) = U(\xi) + iV(\xi)$ in the complex plane.

The simplest illustration is the totally unobscured, plane wavefront. In this case the limits of both integrations extend from $-\infty$ to $+\infty$, which as is seen from figure 7.2 is an arrow of length $\sqrt{2}$ and phase $\pi/4$. Therefore, $\psi_{\mathcal{P}}$ is equal to $(2^{1/2}e^{i\pi/4})^2(-i/2)\psi_{\mathcal{Q}}e^{ikz} = \psi_{\mathcal{Q}}e^{ikz}$, as we could have seen from solving the Helmholtz equation for a plane wave.

Still following Kip Thorne's lecture notes, we make the following points

- Considering the integral derived above it is clear that only those light paths that are within a few Fresnel lengths of the geometric-optics path of least distance contribute to the wave field at the point \mathcal{Q} .
- Related to this, when computing the diffraction pattern from a more complicated aperture it is only necessary to perform the integral in the immediate vicinity of the geometric-optics ray.
- Finally, when integrating over the whole area of the wave front at \mathcal{Q} , we sum contributions with increasingly large phase differences that add up in such a way that the total has a net extra phase of $\pi/2$, relative the geometric optics ray. This phase factor cancels exactly the prefactor $-i$ in the Fresnel-Kirchhoff integral.

7.2 Lunar occultation of a radio source

The next simplest case of Fresnel diffraction is the pattern formed by a straight edge. Let us take the example of a quasar's radio waves being occulted by the moon. Treating the lunar limb as a straight edge, the radio source will create a changing diffraction pattern as it passes behind the moon, and this pattern can be measured by a radio telescope on the earth. Orient the coordinates such that the moon's edge is along the y' (or t) direction. Then we have $\Delta S_t \equiv S(t_{max}) - S(t_{min}) = \sqrt{2}i$ is constant, and $\Delta S_s \equiv S(s_{max}) - (s_{min})$ is described by the Cornu spiral: long before the occultation, ΔS_s is given by the arrow from $(-1/2, -1/2)$

to $(1/2, 1/2)$, *i.e.* $\Delta S_s = \sqrt{2}i$, and the observed amplitude is $\psi_Q e^{ikz}$. When the moon begins to occult the radio source, the upper bound on the Fresnel integral begins to diminish from $s_{max} = +\infty$, and the complex vector on the Cornu spiral begin to oscillate in length and phase. The observed flux will also oscillate, more and more strongly as geometric occultation is approached. At the point of geometric occultation, the complex vector extends from $(-1/2, -1/2)$ to $(0, 0)$ and so the observed wave amplitude is one half the occulted value and the intensity is one fourth. As the occultation proceeds, the length of the complex vector and thus the observed flux will decrease monotonically to zero, while the phase continues to oscillate.

Historically, diffraction of a radio source's waves by the moon led to the discovery of quasars.

7.3 Circular Apertures

The diffraction pattern for a plane wave can be thought of as formed by waves that derive from a patch a few Fresnel lengths in size. This point can be driven home by reanalyzing the unobstructed wave front in circular polar coordinates.

Consider a plane wave incident on an aperture \mathcal{Q} that is infinitely large, and define $\rho \equiv |\mathbf{x}'|/r_F = \sqrt{\frac{1}{2}(s^2 + t^2)}$. Then the phase factor in equation 7.1 is $\Delta\phi = \pi\rho^2$ and the observed wave will thus be given by

$$\begin{aligned}\psi_{\mathcal{P}} &= -i \int_0^\rho 2\pi\rho d\rho e^{i\pi\rho^2} \psi_Q e^{ikz} \\ &= (1 - e^{i\pi\rho^2}) \psi_Q e^{ikz}.\end{aligned}$$

This integral does not converge as $\rho \rightarrow \infty$! Why is that? Add up the contributions to $\psi_{\mathcal{P}}$ from each annular ring as one integrates outward from $\rho = 0$; when one has integrated out to a radius of r_F , *i.e.* $\rho = 1$, the contribution to the observed wave is $\psi_{\mathcal{P}} = 2\psi_Q$, in phase with the incident wave. But, when the integration has been extended to $\sqrt{2}r_F$, $\rho = \sqrt{2}$, $\psi_{\mathcal{P}} = 0$. And as ρ increases the integral will continue to oscillate.

Of course, we have already proven that this integral converges. Let us analyze what is going on by splitting up the aperture \mathcal{Q} into concentric annular rings, known as *Fresnel half-period zones*, of radius $\sqrt{nr_F}$, where $n = 1, 2, 3, \dots$. The odd numbered rings cancel out the contribution from the even number rings. However, the thickness of these rings decreases as $1/\sqrt{n}$, and eventually one must allow for the fact that the incoming wave is not exactly planar, or equivalently that the wave's distant source has finite size. The finite size causes the different pieces of the source to have their Fresnel rings centered at slightly different points in the aperture plane, causing the computation of $\psi_{\mathcal{P}}$ to begin averaging over rings, and the intensity asymptotes to $|\psi_Q|^2$.

Why have we then chosen such a strange way of decomposing a plane wave front? Because it allows for a particularly striking experimental verification of the theory of diffraction propounded here. Suppose one fabricates an aperture (a *zone plate*) in which, for a chosen observation point \mathcal{P} on the optic axis, alternate half-period zones are obscured. Then the wave observed at \mathcal{P} will be the linear sum of several diameters, and the sum should be larger than ψ_Q . This strong amplification is confined to our chosen spot on the optic axis; most everywhere else the field's intensity is reduced, thereby conserving energy. Thus, the zone

plate behaves like a lens. The lens' focal length is $f = kA/2\pi^2$, where A (typically chose to be a few mm^2 for a table top experiment) is the area of the first half-period zone. An interesting historical side note is that Poisson predicted this spot as a consequence of Fresnel's theory of light, and was planning to use it as an argument to disprove the theory. However, it was quickly demonstrated that the bright spot actually existed!

Zone plates are only good lenses when the radiation is monochromatic, since the focal length is wavelength-dependent $f \propto \lambda^{-1}$. Further, they have the interesting property that they posses secondary foci, where the fields from $3, 5, 7, \dots$ contiguous zones add up coherently.

7.4 Seeing in the atmosphere

7.4.1 A simple model (with exercises)

Stars viewed through the atmosphere appear to have angular diameters of order an arc second and to exhibit large amplitude fluctuations of flux with characteristic frequencies that can be as high as 100 Hz. Both of these phenomena are a consequence of irregular variations in the refractive index of the atmosphere. A simple model of this effect consists of a thin phase-changing screen, about a km above the ground, on which the rms phase variation is $\Delta\phi \gtrsim 1$ and the characteristic spatial scale on which the scale changes by $\sim \Delta\phi$ is a .

It is straightforward to show that rays will be irregularly deflected through a scattering angle $\Delta\theta \sim (\lambda/a)\Delta\phi$. Strong intensity variations require that several rays deriving from points on the screen separated by more than a , combine at each point on the ground. These rays combine to create a diffraction pattern on the ground with scale b .

It is possible to show that the Fresnel length in the screen is $\sim \sqrt{ab}$. The time variation in the observed intensity arises because winds in the upper atmosphere with speeds $u \sim 30 \text{ m s}^{-1}$ blow the irregularities and the diffraction pattern past the observer. The information given above is sufficient to estimate the Fresnel length r_F , the atmospheric fluctuation scale size a , and the rms phase variation $\Delta\phi$.

7.4.2 Effects of the atmosphere (including better model)

The two major effects of the Earth's atmosphere are *atmospheric refraction* and distorted wavefronts (or *seeing*) due to refraction in a turbulent atmosphere.

We can approximate the atmosphere as a series of plane-parallel plates, and the surface as an infinite plane. A ray incident at angle α refracts at each of the interfaces, and will ultimately make a new angle $\alpha + \Delta\alpha$ with the surface: thus, refraction shifts the apparent position of the source towards the zenith. The atmosphere consists of a very large number of thin layers and the total effect of refraction is to curve the path of the incident ray. In this limit Fermat's principle and the plane-parallel model gives

$$\Delta\alpha = R_0 \tan \alpha = \frac{n^2 - 1}{2n^2} \tan \alpha \approx (n - 1) \tan \alpha$$

where n is the index of refraction at the surface. The quantity $(n - 1) \times 10^6$ is the *refractivity*. Since the index is a function of wavelength rays of different colors are refracted at different angles, and at large zenith distances images are actually very low resolution spectra — with the blue image shifted more towards the zenith than red.

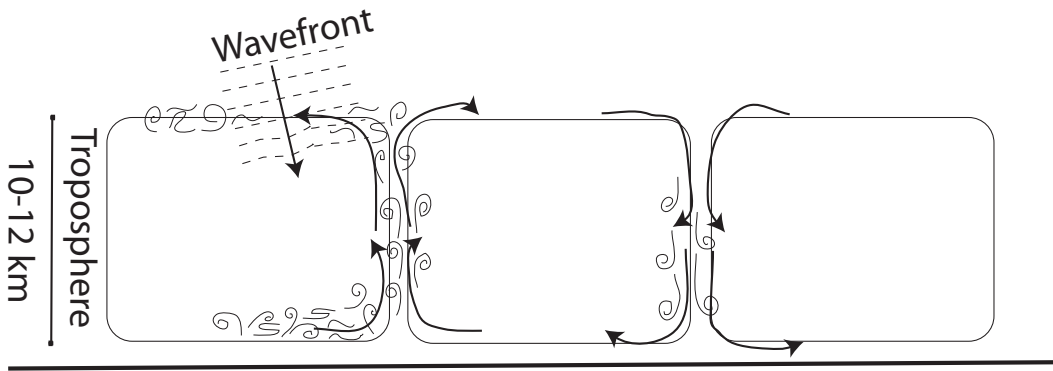


Figure 7.3: Sketch of atmospheric circulation in the troposphere and the effects it has on incoming wavefronts. Locally heated air near the ground will become buoyant and rise, resulting in a convective flow as cool air flows to fill its place. Turbulence is enhanced at the boundaries of convection cells.

In a perfectly serene and quiet atmosphere, then density and index of refraction of air will depend only on altitude, and every point at the same height will have the same index. In the real atmosphere solar heating drives convective cells in the lowest layer of the atmosphere, a region some 10–12 km thick called the *troposphere*. One mass of air can become slightly hotter and more buoyant than its neighbors and therefore rise. Another mass moves horizontally to take its place; cold air from above drops down to make room for the rising mass and completes the circulation around a cell. Many cells are established, and the air, especially at the boundaries of the flow, tends to break up into turbulent eddies of different density and temperature.

A wavefront from a distant star passing through the atmosphere arrives as a plane, but different parts will encounter slightly different patterns in the index of refraction. Each ray will traverse slightly different optical path, and the wavefront will no longer be a plane. Since the turbulent eddies at each altitude move at the local wind speed, the distortion in the wavefront changes very quickly.

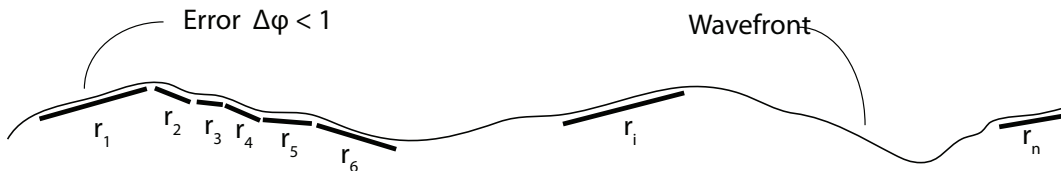


Figure 7.4: Quantifying the wavefront is done by fitting the wavefront with straight segments along which the difference between vertical z direction between the fit and the wavefront is less than $\lambda/2\pi$ (equivalent to changes in phase $\Delta\phi < 1$). The length of a segment r_i is called the coherence length and the average of all segments is the coherence length of the wavefront.

We can quantify this wavefront distortion. Consider first a one-dimensional model, start at one end of the wavefront and fit a straight line to a segment of the front. How long can this segment be before the fit becomes “poor”? We need a criterion for judging the goodness of fit, and we choose the root mean square (RMS) difference in the vertical z direction between the front and the fit. If this quantity becomes greater than $\lambda/2\pi n$, then fit is poor. This is

equivalent that the RMS deviation of phase ϕ is less than one radian. The maximum length that can be fit is r_1 , called the coherence length of the first segment. Moves along the front fitting successive segments of “good fit” r_i . The statistical mean of all the r_i values is r_{avg} the *coherence length of the wavefront*. Each segment has a different slope, so each will propagate in a slightly different direction, and each will focus at a different spot in the image plane of a telescope. The shorter the coherence length, the more *speckles* in the image.

Extending to two dimensions: select a random point on a two-dimensional wavefront and ask how large a 2D patch of the front we can expect to be coherent. The answer is called *Fried’s parameter* $r_{0\lambda}$, the expected diameter over which the RMS optical phase distortion is 1 radian.

7.4.3 Real time atmospheric compensation

Arguments of the sort given above (though with a somewhat more sophisticated model of atmospheric turbulence) can be used to derive the maximum diameter of a telescope before it becomes seriously affected by *seeing*, given by Fried’s coherence length

$$r_0 \approx 0.114 \left(\frac{\lambda \cos z}{550} \right)^{0.6} \text{ m}$$

where λ is the observing wavelength in nm and z is the zenith angle. Fried’s coherence length, r_0 is the distance over which the phase difference is one radian, and plays the same role as a in the simpler model above. In particular, the full width at half maximum of the seeing disk is given by

$$\theta \approx 0.2 \frac{\lambda [\mu\text{m}]}{r_{0\lambda} [\text{m}]}$$

If the diameter of a telescope, D , is larger than $r_{0\lambda}$, then this expression gives the image size. If $D < r_{0\lambda}$ the telescope is diffraction limited. Values for r_0 vary from a few centimeters to 15 or 20 cm (which is excellent seeing).

Short of placing telescopes in space above the atmosphere, one alternative is to correct the distortions introduced by atmospheric turbulence by the use of adaptive optics. In such systems, one or more of the optical components can be changed rapidly in such a manner that the undesired distortions in the light beam are reduced or eliminated.

The efficiency of an adaptive optics system is measured by the *Strehl ratio*. This quantity is the ratio of the intensity at the center of the corrected image to that at the center of a perfect diffraction limited image of the same source. The *normalized Strehl ratio* is the Strehl ratio of the corrected image divided by that for the uncorrected ratio. Strehl ratios of up to 0.6 are currently being achieved and one may reach 0.8 in the near future.

Note that a weakness of adaptive optics is that in the visual and near infrared, the correction only extends over a very small area (the *isoplanatic patch*).

Note also that there is some confusion in the literature between terms adaptive optics and active optics. We will consider adaptive optics to be those characterised by a fast closed-loop system, and active optics a more slowly operating open- or closed-loop system. The division is made at a response time of a few seconds. Thus, the tracking of a star by the telescope can be considered an active optics system that is open-loop if no guiding is used, and closed-loop if guiding is used. Large thin mirror optical systems may suffer distortions due to buffeting by wind at a frequency of 0.1 Hz or so; they may also distort under gravitational loading or thermal stresses. Correction of these sorts of effects also goes under the heading active optics.

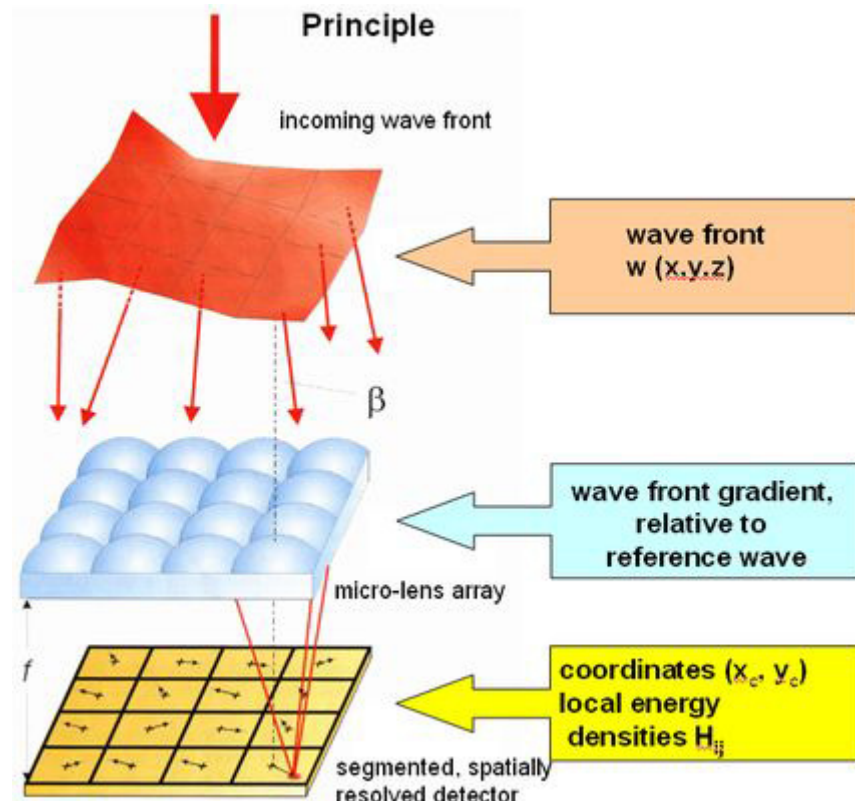


Figure 7.5: Principle of the Shack-Hartmann sensor. (figure from *Institut für Photonische Technologien e. V.*)

An atmospheric compensation system contains three main components, a sampling system, a wave front sensor, and a correcting system.

Sampling systems. The sampling system provides the sensor with the distorted wave front or a simulacrum thereof. A beam splitter is commonly used. This is a partially reflecting mirror that typically diverts about 10% of the radiation to the sensor, while allowing the remaining 90% to continue on to form the image.

In night time astronomy even the loss of 10% of the light is to be regretted. Many adaptive systems therefore use a guide star rather than the object of interest to measure the wave front. This becomes especially important when the object to be imaged is a large extended object, since sensors generally must be used on point or near point images (or at least images with sharp gradients, see figure 7.6). The guide star must be very near in the sky to the object of interest or its wave front will have gone through different atmospheric distortion. The isoplanatic patch is defined by the distance over which the Strehl ratio improvement due to the adaptive optics halves. In the visible it is typically of order 15 arcsec. The size of this patch scales as $\lambda^{1.2}$, so it is larger in the infrared, reaching typically 80 arcsec at $2.2 \mu\text{m}$.

The small size of the isoplanatic patch means that few objects have suitable guide stars; less than 1% of the the sky can be covered using real stars as guides. Recently therefore, artificial guide stars have been produced. This is done by using lasers pointed skywards. The laser is tuned to one of the sodium (Na) D line frequencies and excites the free sodium atoms in the atmosphere at a height of about 90 km. The glowing atoms appear as star-like patches

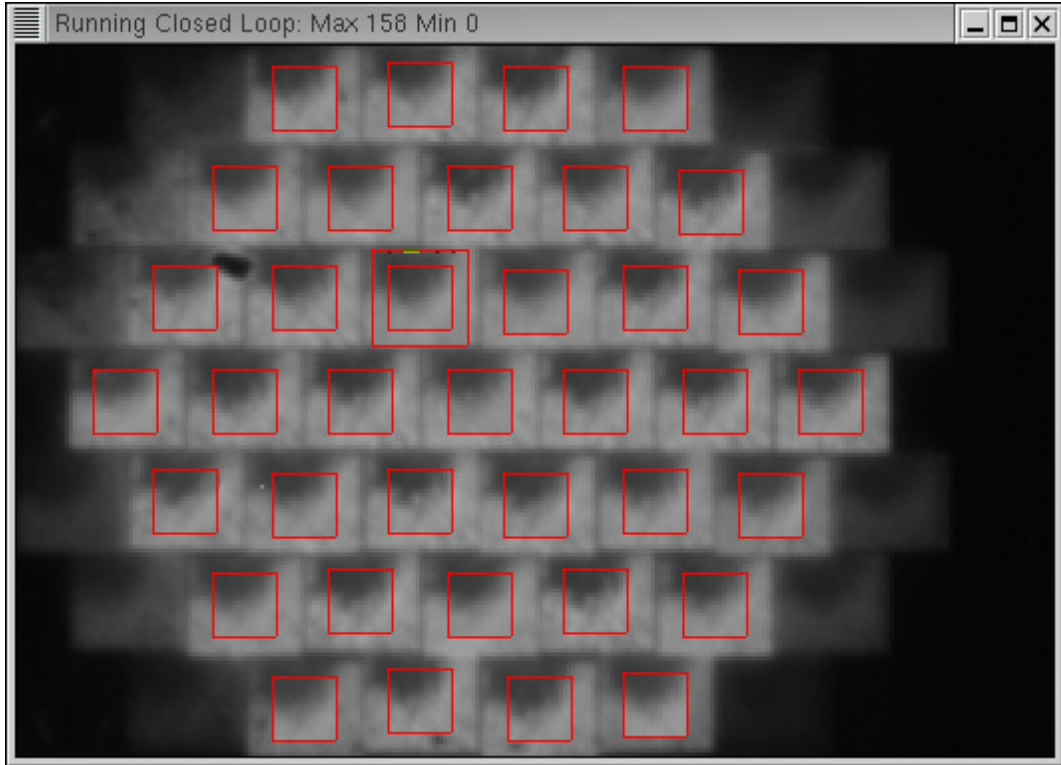


Figure 7.6: The multiple images of the Shack-Hartmann micro lenses as seen in the Swedish 1 meter Solar Telescope.

that can be placed as near in the sky to the object of interest as required. Guide stars at lower altitudes and at other wavelengths can be produced through back scattering by air molecules of a laser beam. Two difficulties with this technique are the *cone problem* due the geometry of the laser setup compared with the telescope and the fact that the laser light also must pass *up* through the atmosphere and therefore the guide star moves with respect to the object. Use of real stars to separately compensate tip-tilt, and the use of two or several guide stars can eliminate some or parts of this problem.

Wave front sensing. The wave front sensor detects the residual and changing distortions in the wave front provided by the sampler after reflection from the correcting mirror. The Shack-Hartmann sensor is a two dimensional array of small lenses (figure 7.5). Each lens produces an image that is sensed by an array detector. In the absence of wave front distortions, each image will be centered on each detector. Distortion will displace the images from the centers of the detectors, and the degree of displacement and its direction is used to generate the error signal.

Wave front correction. The correction of the wave front is achieved by distorting a subsidiary mirror. Since the atmosphere changes on a time scale of 10 ms or so, the sampling, sensing and correction have to occur in 1 ms or less. In the simplest systems only the tip and tilt of the wave front introduced by the atmosphere is corrected. That is accomplished by suitably inclining a plane or segmented mirror placed in the light beam from the telescope in the opposite direction.

More sophisticated approaches provide better corrections; either just of the relative dis-

placements within the distorted wave front, or of both displacement and fine scale tilt. Displacement correction typically uses a thin mirror capable of being distorted by up to 100 piezoelectric or other actuators placed underneath. The error signal from the sensor is used to distort the mirror in the opposite manner to the distortions in the incoming wave front. The reflected wave front is therefore almost flat.

Plans for future 50 m and 100 m telescopes include adaptive secondary or tertiary mirrors up to 8 m in diameter, requiring up to 500 000 actuators to compensate the atmospheric distortions of the wave front.

7.5 Exercises

1. Why is $\Delta\phi \approx \frac{kx'^2}{2z}$ in Eq. 7.1?
2. Check that the transition to a double integral in Eq. 7.1 is correct.
3. Derive a formula for the intensity diffraction pattern $F(x)$ of a slit with width a , as a function of distance x from the center of the slit, in terms of Fresnel integrals.
4. Recreate figure 7.2 using IDL. The following fragments of code might be useful

Listing 7.1: Useful code I

```
function fresnel_cos , xi
;
fcos=fltarr( n_elements( xi ) )
for i=0,n_elements( xi )-1 do begin
    npt=10000
    s=findgen( npt )/npt*xi[ i ]
    fcos[ i ]=trapez( s , cos( ! pi*s*s /2. ) )
endfor
return , fcos
;
end
```

and equivalent for `fsin`, which both call the function

Listing 7.2: Useful code II

```
function trapez , x0 , y0
;
n=n_elements( x0 )
x=fltarr( n )+x0
y=fltarr( n )+y0
integrand=(y+shift( y ,-1 ))*( shift( x ,-1 )-x )
return , total( integrand ( 0:n-2 ))*0.5
;
end
```

(I am sure that this integral can be done in a **much** better way using calls to the error function $\text{erf}(x) = \frac{2}{\sqrt{\pi}} \int_0^x e^{-t^2} dt$, but this will work.)

5. Using IDL and the routines above, plot the one-dimensional intensity diffraction pattern $|\psi|^2$ produced by a slit, $t(x) = 1$ for $|x| < a/2$ and $t(x) = 0$ for $|x| > a/2$, for the values $r_F/a = 0.05, 0.5, 1, 2$.
6. Explain why the focal length of a zone plate is $f = kA/2\pi^2$.
7. An opaque, perfectly circular disk of diameter D is placed perpendicular to an incoming plane wave. Show that, at distances r such that $r_F \ll D$, the disk casts a rather sharp shadow, but at the precise center of the shadow there should be a bright spot. How bright?

Use Section 7.4.1 to answer the questions below.

8. Explain why $\Delta\theta \sim (\lambda/a)\Delta\phi$.
9. Show that the Fresnel length in the screen is $\sim \sqrt{ab}$.
10. Use the information given above to estimate r_F , the atmospheric fluctuation scale a , and the rms phase variation $\Delta\phi$.

Chapter 8

Radio, EUV and X-ray telescopes

8.1 Radio and microwave detection

Karl Jansky was the first person who observed the galaxy with radio waves in 1931, thereby discovering Sagittarius A, which marks the massive black hole at the center of the Milky Way¹. Thus, radio astronomy is the oldest of the ‘new’ astronomies. The reason that radio astronomy was early is in part because radio waves easily penetrate to ground level; for wavelengths from about 10 mm to 10 m the atmosphere is almost completely transparent. The absorption becomes almost total at 0.5 mm and between 0.5 mm and 10 mm there are a number of absorption bands that are mainly due to oxygen and water vapor. The scale height for H₂O in the atmosphere is about 2000 m so that observing from high altitudes reduces the short wave absorption considerably. Radiation with $\lambda > 50$ m does not penetrate to the ground, because of reflection by the ionosphere.

The unit of intensity that is commonly used in radio astronomy is the jansky (Jy)

$$1 \text{ Jy} = 10^{-26} \text{ Wm}^{-2}\text{Hz}^{-1}$$

and detectable radio sources vary from about 10^{-3} to 10^6 Jy. Most radio sources generate their flux as thermal radiation, which by the Rayleigh-Jeans law gives a spectrum

$$F_\nu = \frac{2\pi k}{c^2} T \nu^2,$$

or by synchrotron radiation from energetic electrons spiralling around in magnetic fields, where the spectrum is in the form

$$F_\nu \propto \nu^{-\alpha},$$

where α is called the spectral index of the source, and is related to the energy distribution of the electrons. For most sources it is in the range $0.2 \leq \alpha \leq 1.2$.

¹Jansky was actually hired by Bell Telephone Laboratories to study the effects of thunderstorms on radio frequency communication. He designed an antenna that responded to waves at 14.6 m. He found signals from thunderstorms but also “... a steady hiss type static of unknown origin”. The source appeared 4 minutes earlier every day, and Jansky concluded that it must have a origin outside the solar system, finally identifying the source as Milky Way in 1933.

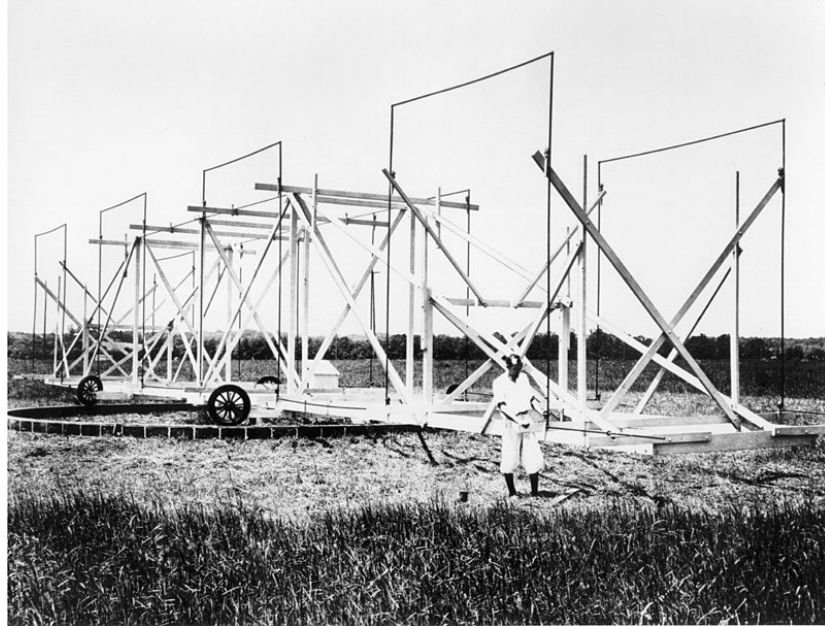


Figure 8.1: Karl Jansky and his antenna.

8.2 Detectors and receivers

The detection of radio signals is a two-stage process in which the sensor produces an electrical signal that then has to be processed until it is in a usable form. In the MHz radio region, the sensor is normally a dipole placed at the focus of a telescope, such as a half-wave dipole. The two halves of such a dipole are each a quarter of a wavelength long.

In the GHz and higher frequencies a horn antenna is normally used to collect the radiation, usually with waveguides for the connection to the rest of the system, though plastic and quartz lenses may be used at very high frequencies. The sensor at the higher frequencies is normally a superconductor-insulator-superconductor (SIS) device. In an SIS detector, an electron in one superconducting film absorbs a photon, giving the electron enough energy to tunnel through the insulating barrier into the other superconducting film. This process, known as photon-assisted tunneling, produces one electron for every absorbed photon. Devices are based upon two niobium layers separated by an insulating region of aluminium oxide around 1 nm thick and the whole cooled to 4 K or less.

The signal from the sensor is carried to the receiver whose purpose is to convert the high frequency electrical currents into a convenient form. The behaviour of the receiver is governed by five parameters: sensitivity, amplification, bandwidth, receiver noise level, and integration time. The sensitivity and the other parameters are very closely linked, for the minimum detectable brightness, B_{\min} , is given by

$$B_{\min} = \frac{2k\nu^2KT_s}{c^2\sqrt{t\Delta\nu}}$$

where T_s is the noise temperature of the system, t is the integration time, $\Delta\nu$ is the frequency bandwidth and K is a constant close to unity that is a function of the type of receiver. The receiver noise originates as thermal noise within the electrical components of the receiver, and

may also be called Johnson or Nyquist noise. It is usually necessary to cool the initial stages of the receiver with liquid helium in order to reduce T_s to an acceptable level.

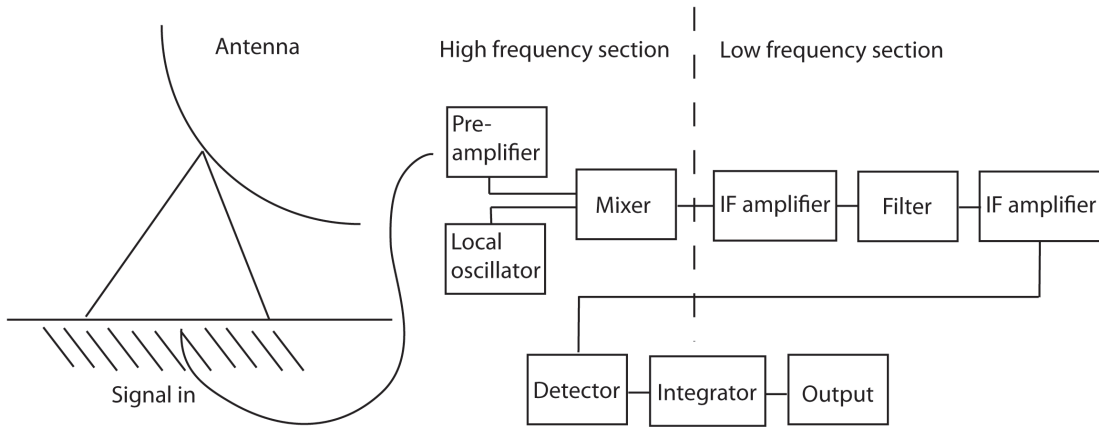


Figure 8.2: Block diagram of a basic heterodyne receiver (figure adapted from Kitchin *Astrophysical Techniques*).

8.2.1 Heterodyne receiver

In figure 8.2 we show schematically the set up for a heterodyne receiver. The pre-amplifier operates at the signal frequency and will typically have a gain of 10 to 1000. The local oscillator produces a signal that is close to but different from the main signal in its frequency. Thus when the mixer combines the main signal and the local oscillator, the beat frequency between them (intermediate frequency or IF) is at a much lower frequency than that of the original. The relationship between them is

$$\nu_{\text{signal}} = \nu_{\text{LO}} \pm \nu_{\text{IF}}.$$

Normally, at lower frequencies only one of the two possible frequencies will be picked up by the feed antenna or passed by the pre-amplifier. The power of the IF emerging from the mixer is directly proportional to the power of the original signal. The IF amplifiers and filter determine the pre-detector bandwidth of the signal and further amplify it by a factor 10^6 to 10^9 . In the final stages of the receiver, the signal from the detector is integrated, usually for a few seconds, to reduce the noise level. Then it is fed to an output device, usually analogue-to-digital input to a computer for further processing.

The basic heterodyne system has a high system temperature and unstable gain. The temperature can be lowered by applying an equal and opposite voltage in the later stages of the receiver, and the stability of the gain can be improved by switching rapidly from the antenna to a calibration noise source and back again, with a phase sensitive detector to correlate the changes. Such a system is called a Dicke radiometer. The radiometer work optimally if the calibration noise source has the same temperature as the signal. The value of T_s varies from 10 K at 1 m to 10 000 K at 1 mm. At long wavelengths diodes can be used as noise sources, while at short wavelenghts gas discharge tubes can be used.

Receivers are generally sky background limited. The Earth's atmosphere radiates at 100 K and higher temperatures below a wavelength of about 3 mm. Only between 30 and 100 mm

does its temperature fall as low as 2 K. At longer wavelengths, the galactic emission becomes important, rising to 10^5 K at wavelengths of 30 m.

Spectrographs at radio frequencies can be obtained in several different ways. Today, most radio spectroscopy is carried out by auto-correlation. Successive delays are fed into the signal that is then cross-correlated with the original signal in a computer. The spectrum is obtained from the Fourier transform of the result. Note that this technique is very similar to the Fourier transform spectrometers to be discussed later.

Alternately the radio signal may be converted into a different type of wave, and the variations in this secondary wave studied instead. This is the principle behind the *acousto-optical radio spectrometer* (AOS).

A major problem at all frequencies in radio astronomy is interference from artificial sources. In theory, certain regions of the spectrum are reserved partially or exclusively for use by radio astronomers, but leakage from devices such as microwave ovens, incorrectly tuned receivers, and illegal transmissions often overlap these bands. For example the Russian GLONASS satellite navigation system overlaps into the band reserved for interstellar OH lines at 1.61 GHz.

8.3 Radio telescopes

The nature of electro-magnetic radiation is the same whether it be radio waves or optical light that is discussed. On the other hand, the image in an optical telescope is discussed in terms of its diffraction structure, while that of a radio telescope is discussed in terms of its polar diagram. However, these are just two different approaches to the presentation of the same information. The polar diagram is a plot, in polar coordinates, of the sensitivity or voltage output of the telescope, with the angle of the source from the optical axis (note that we are discussing sources that are far from the receiver). The polar diagram may be physically realized by sweeping the telescope past a point source, or by using the telescope as a transmitter and measuring the signal strength around it.

The polar diagram, and hence the performance of the antenna, may be described by four parameters: the beam width at half-power points (BWHP), the beam width at first nulls (BWFN), the gain, and the effective area. The first nulls are the positions on either side of the optical axis where the sensitivity of the antenna first decreases to zero. Thus, the value of the BWFN for the half-wave dipole is 180° . The first nulls are the direct equivalent of the first fringe minima in the diffraction pattern of an optical image, and for a dish antenna type of radio telescope, their position is given by

$$\text{BWFN} = 2 \times \frac{1.22\lambda}{D}$$

The half power points may be best understood by regarding the radio telescope as a transmitter; they are then the directions in which the broadcast power has fallen to one half of its peak value. The maximum gain or directivity is also best understood in terms of a transmitter. It is the ratio of the peak value of the output power to the average power. The effective area of an antenna is the ratio of its output power to the strength of the incoming flux of the radiation that is correctly polarized to be detected by the antenna

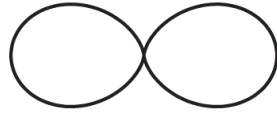
$$A_e = \frac{P_\nu}{F_\nu}$$

where A_e is the effective area, P_ν is the power output by the antenna at frequency ν and F_ν is the correctly polarized flux from the source at the antenna at frequency ν . The effective area and maximum gain g are related by

$$g = \frac{4\pi}{c^2} \nu^2 A_e.$$

For the half-wave dipole, the maximum gain is about 1.6, and so there is very little advantage over an isotropic receiver.

Half-wave dipole Collinear array with two half wave dipoles



Collinear array with four half wave dipoles



Isotropic receiver



Figure 8.3: Polar plots for a single half-wave dipole, collinear arrays with two and four dipoles and an isotropic receiver.

The performance of a simple dipole may be improved by combining the outputs from several dipoles that are arranged in an array. In a co-linear array, the dipoles are lined up along their axes and spaced at intervals of half a wavelength. The arrangement is equivalent to a diffraction grating and so the sensitivity at an angle θ to the Long axis of the array $s(\theta)$ is given by

$$s(\theta) = s_0 \left(\frac{\sin(n\pi \sin \theta)}{\sin(\pi \sin \theta)} \right)$$

where n is the number of half-wave dipoles and s_0 is the gain of a single half wave dipole which is $\propto \cos^2 \theta$. Examples of polar diagrams are shown in figure 8.3. The resolution along the axis of the array, measured to the first null is

$$\alpha = \sin^{-1} \left(\frac{1}{n} \right).$$

Although the resolution of an array is improved over that of a simple dipole along its optical axis, it will still accept radiation from any point perpendicular to the array axis. The use of a *broadside array* in which the dipoles are perpendicular to the array axis and spaced at half wavelength intervals can limit the acceptance angle.

Even so there is a twofold ambiguity in direction of a source that has been detected. This can be removed by placing a reflector behind the dipole. This is simply a conducting rod

about 5% longer than the dipole and unconnected electrically with it. It is placed parallel to the dipole and about one eighth of a wavelength behind it. For an array, the reflector may be a similarly placed electrically conducting screen. Such a reflector is termed a *parasitic element* since it is not part of the electrical circuit of the antenna. Similar parasitic elements may be added in front the dipole to act as directors.

With a reflector and several directors we obtain the parasitic or *Yagi* antenna, perhaps familiar from its appearance on rooftops as a television antenna. The main use of parasitic antenna in radio astronomy is as the receiving element of a larger reflector such as a parabolic dish.

The use of a single dipole, or even several dipoles in an array, is the radio astronomy equivalent of naked-eye observation. The most usual method of concentrating the signal is to construct large parabolic dishes. These are directly equivalent to an optical reflecting telescope. They are usually used at the prime focus or at the Cassegrain focus. The gain may be found roughly by substituting the dishes' area for the effective area. The size of telescopes is so large because of the length of the wavelength being observed. The requirement on surface accuracy is the same as that for an optical telescope: deviations from the paraboloid must be less than $\lambda/8$ if the Rayleigh resolution is not to be degraded, in practice a limit of $\lambda/20$ is often used. Note also that the surface of the "mirror" need not be solid, a wire mesh with spacings less than $\lambda/20$ will function equally well as a reflector. This has large implications for the weight and wind resistance of the dish. The dishes are usually of very small focal ratios (f0.5 or so) and the reason is so that the dish acts as a screen against unwanted radiation. Fully steerable dishes up to 100 m across have been built, while the Arecibo telescope is a fixed dish 300 m across. In the microwave region the largest dishes are currently the 30 m IRAM instrument on Pico Veleta in Spain and the 45 m telescope at Nobeyama in Japan.

With a single feed, the radio telescope is a point source detector only. Images have to be built up by scanning or by interferometry.

True imaging can be achieved by the use of cluster or array feeds. These are simply multiple individual feeds arranged in a suitable array at the telescope's focus. Each feed is then the equivalent of a pixel in a CCD. The number of elements in such cluster feeds currently remains small compared to their optical equivalents; for example the 64 m Parkes radio telescope uses a 13-beam receiver for 21 cm radiation.

Very many other systems have been designed to fulfill the same function as a steerable paraboloid but which are easier to construct.

Another approach is used in the Mills Cross type telescope. This uses two perpendicularly oriented collinear arrays, *e.g.* north–south and east–west. The first provides a narrow fan beam along the north–south direction while the second provides a similar beam in the east–west direction. Their intersection is a narrow vertical pencil beam, typically 1° across. This beam can be isolated from the contributions of the remainder of the fan beams by comparing the outputs when the beams are added in phase and when they are added out of phase. This pencil beam can be displaced an angle θ from the vertical by introducing a phase shift between each dipole.

Yet another approach is based on refraction. The Luneburg lens is a solid sphere within which the refractive index increases linearly inward from unity at the surface. With a central refractive index of 2, the focus is on the surface of the lens. Since there is no axis of symmetry, the lens can be used to observe in many directions simultaneously, simply by having many feeds distributed around it. The Luneburg lens has yet to find application in radio astronomy, but may be used in the Square Kilometer Array.

8.3.1 Spacecraft

A number of spacecraft carrying microwave detectors have been launched. These include COBE, MAP and Planck which all are designed to measure anisotropies in the cosmic microwave background radiation.

8.3.2 Construction

Largest problem is wind: *e.g.* up to 1.5×10^6 N for a 50 m dish facing directly into a gale-force wind. There are only two solutions to the wind problem: to enclose the dish, or to cease using it when the wind load becomes too great. Some smaller dishes are therefor enclosed in *radomes*, which are space-enclosing structures built from non-conducting materials.

8.4 X-ray and gamma-ray detection

This third region of the spectrum to be discussed is the most recent area to be explored. None of the radiation penetrates to ground level, so its study had to await the availability of observing platforms in space, or near the top of the Earth's atmosphere. The high energy spectrum can be divided into

- extreme ultraviolet (EUV): 10 to 100 nm (12 to 120 eV)
- soft x-rays: 1 to 10 nm (120 to 1200 eV)
- x-rays: 0.01 nm 1 nm (1.2 to 120 keV)
- soft gamma-rays: 0.001 to 0.01 nm (120 to 1200 keV)
- gamma-rays: less than 0.001 nm (greater than 1.2 MeV)

The main production mechanisms for high-energy radiation include electron synchrotron radiation, the inverse Compton effect, free-free radiation, and pion decay, while the sources include the Sun, supernova remnants, pulsars, bursters, binary systems, cosmic rays, the intergalactic medium, galaxies, Seyfert galaxies, and quasars. The interstellar absorption in this region varies roughly with the cube of the wavelength, so that the highest energy radiation can easily pass through the whole galaxy with little chance of being intercepted. The flux of radiation varies enormously with wavelength. The solar emission alone at the lower energies is sufficient to produce the ionosphere and thermosphere on the Earth. At 1 nm wavelength, for example, the solar flux is 5×10^9 photons $\text{m}^{-2}\text{s}^{-1}$, while the total flux from all sources above 10^9 eV is only a few photons per square meter per day.

8.4.1 Detectors

Geiger counters

Two electrodes inside an enclosure are held at such a potential difference that a discharge in the medium filling the enclosure is on the point of occurring. The medium inside the tube is typically argon at a low pressure with a small amount of organic gas, such as alcohol vapour added. The entry of ionizing radiation triggers this discharge, resulting in pulse of current between the electrodes that then may be amplified and detected. The electrons produced in

the initial ionization are accelerated towards the central electrode by the applied potential; as these electrons gain energy they cause further ionization, producing more electrons, and so on. Gain of some 10^8 electrons for every one in the initial ionizing trail. The avalanche of electrons rapidly saturates, so that the detected pulse is independent of the original energy of the photon. Another disadvantage of Geiger counters, shared by many of the detectors described below is that a response to one event leaves the detector inoperative for a short interval, known as the dead time, caused by the reduction in the potential between the electrodes. The length of the dead time for this type of detector is of order $200\ \mu\text{s}$.

Proportional counters

Geiger counters run at a lower voltage, so that saturation is avoided and the strength of the signal is proportional to the original signal. The gain is reduced to 10^4 , 10^5 . Provided all the energy of the ionizing radiation is absorbed within the detector, its original total energy may be obtained from the strength of the pulse. At high photon energies the detector is limited by the requirement that all the energy of the radiation be contained within the detector. To this end, proportional counters for high-energy detection may have to be made quite large. About 30 eV is required to produce one ion-electron pair, so that a 1 keV photon produces about 36 electrons, and a 10 keV photon 360 electrons. The spectral energy resolution to two and a half standard deviations is thus about 40% at 1 keV and 12% at 10 keV. The quantum efficiencies of the proportional counter approach 100% for energies up to 50 keV. The position of interaction of the x-ray along the counter may be obtained through the use of a resistive anode. The pulse is measured at both ends of the anode and a comparison of the strength and shape leads to a leads to the position of the discharge along the anode. The anode wires are typically very thin, $20\ \mu\text{m}$ across, so the electric field is most intense very close to the wire, limiting its spread, and giving a precise position. This concept can be extended to a 2D grid of anodes to allow imaging. Spatial resolutions of 0.1 nm are currently possible and this allows the building of *position-sensitive proportional counters*. Many gases can be used to fill the detector: argon, methane, xenon, carbon dioxide, and mixtures thereof. Inert gases are preferred as there is then no possibility of the loss of energy into the rotation or vibration of the molecules.

Scintillation detectors

The ionizing photons do not necessarily knock out only the outermost electrons from the atom or molecule with which they interact. Electrons in lower energy levels may also be removed. When this happens a ‘hole’ is left behind into which one of the higher electrons may drop, with a consequent emission of radiation. This photon can be observed with a photomultiplier. The noise level is high since only about 3% of the original x-ray energy is converted into detectable radiation. Sodium iodide or caesium iodide are useful for x-ray energies up to several hundred keV, organic scintillators such as stilbene ($\text{C}_{14}\text{H}_{14}\text{N}_2$) can be used up to 10 MeV and bismuth germanate ($\text{Bi}_4\text{Ge}_3\text{O}_{12}$) for energies up to 30 MeV or more. Organically doped plastics are also used. Both sodium iodide and bismuth germanate are used on the burst monitor on board the Fermi Gamma-ray Space Telescope (formerly GLAST) launched during the spring of 2008, to provide continuous detection from some few keV to 25 MeV.

Discrimination of the x-ray’s arrival direction can be obtained by using sodium iodide and caesium iodide in two superposed layers. The decay time of the pulses differ between the

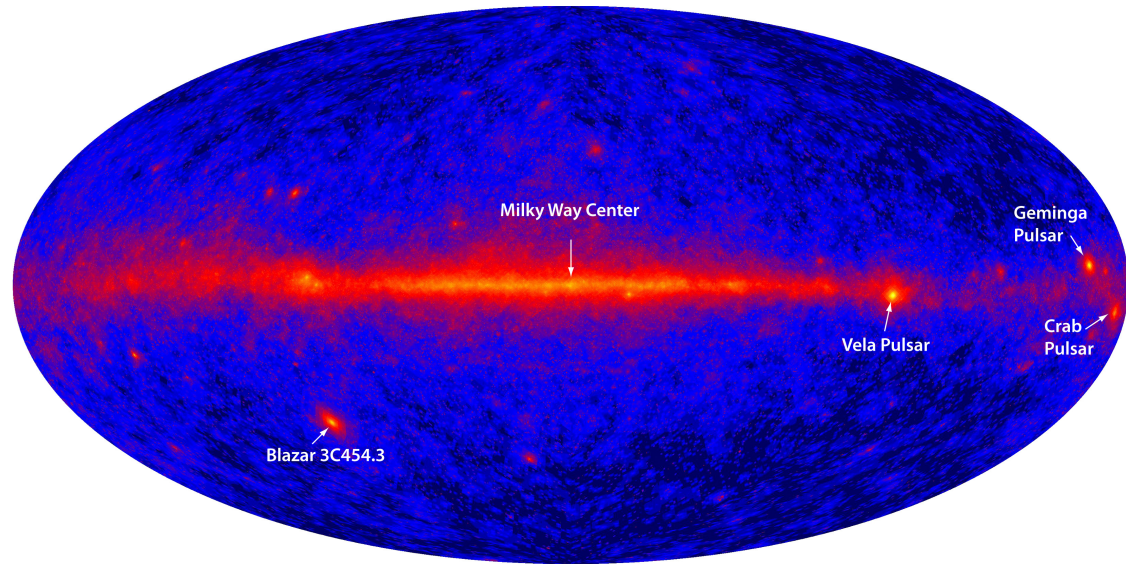


Figure 8.4: First light on the Large Area Telescope on board the Fermi Gamma-ray Space Telescope. The photons that have made this image have an energy greater than 1 GeV.

two compounds so that they may be separately identified, and the direction of travel of the photon inferred. Several gases such as argon, xenon, nitrogen and their mixtures can also be used as scintillators, and combined with an optical system to produce another imaging device.

Gas scintillation proportional counters

A combination of the two above types leads to a significant improvement in the low-energy spectral resolution. Resolution as good as 6% at 6 keV has been achieved in practice. The x-ray radiation produces ion-electron pairs in an argon- or xenon-filled chamber. The electrons are then gently accelerated until they cause scintillation of their own in the gas. These scintillations can then be observed by a conventional scintillation counter system.

Charge-coupled devices (CCDs)

CCDs are becoming increasingly widely used as primary detectors at EUV and x-ray wavelengths. The Chandra spacecraft uses CCDs with a $24 \mu\text{m}$ pixel size, giving 0.5 arcsec resolution. CCDs become insensitive to radiation in the blue and ultraviolet because of the absorption in the electrode structure on their surfaces. They regain sensitivity at shorter wavelengths as radiation is able to penetrate the structure (at $\lambda < 10 \text{ nm}$ or so).

Cherenkov detectors

X-Ray and gamma radiation interest lies in the detection of particles produced by the Compton interaction of very high energy photons. These particles can achieve velocities greater than that of light in the local medium producing Cerenkov radiation. For example, such particles can be produced high in the atmosphere and observed from the ground with telescopes such as CANGAROO-II in Australia or MAGIC on La Palma.



Figure 8.5: One of the two (almost) identical MAGIC telescopes on Roque de los Muchachos Observatory on La Palma.

Solid-state detectors

Solid state detectors have several advantages that suit them particularly for use in satellite-borne instrumentation; a wide range of photon energies detected (from 1 keV to 1 MeV), simplicity, reliability, low power consumption, high stopping power for radiation, room temperature operation, no entrance window needed, high counting rates, etc. They also have intrinsic spectral sensitivity since, provided the photon is absorbed completely, the number of electrons-hole pairs produced is proportional to the photon's energy. The main disadvantage is that their size is small, so that their collecting area is also small, and that unless the photon is stopped within the detector's volume the total energy cannot be determined.

INTEGRAL, launched in 2002, carries a spectrometer that uses germanium detectors. In these a cylinder germanium (cooled by liquid nitrogen) is surrounded by a cylindrical cathode and has a central anode. A gamma ray scatters off electrons in the atoms until its energy has been consumed in electron-hole pair production. The number of released electrons is proportional to the energy of the gamma ray, and these are attracted to the anode where they may be detected. The spectral resolution is high (0.2% at 1 MeV) so that detectors of this type are especially suitable for line spectroscopy. Other materials that may replace germanium include germanium doped with lithium, cadmium telluride and mercury-iodine. At lower energies (0.4 – 4 keV) silicon based solid-state detectors may be used similarly. Their energy resolution ranges from 4 – 30%.

Microchannel plates

Microchannel plates are a variant of the photomultiplier. The devices are also known as Multi-Anode Micro-channel Arrays (MAMAs). A thin plate is pierced by numerous tiny holes, each perhaps only about $10\ \mu\text{m}$ across or less. Its top surface is an electrode with

a negative potential of some 1000 V with respect to the base. The top is coated with a photoelectron emitter for the x-ray energies of interest. An impinging photon releases one or more electrons that are then accelerated down the tubes. Collisions with the tube walls will release further electrons, which are in turn accelerated down the tube walls and so on. As many as 10^4 electrons can be produced by for a single photon, and this may increased to 10^6 electrons in future devices. The quantum efficiency can be up to 20%. The electrons spray out of the bottom of each tube, where they may be detected.

An example is the high resolution x-ray camera aboard Chandra that uses a 93 mm square chevron microchannel plate detector, with 69 million 10 μm holes, and can provide a resolution of 0.5 arcsec.

Microchannel plates can also be used in the optical and near ultraviolet.

8.4.2 Imaging

Collimation

A collimator is a device that physically restricts the field of view of the detector without contributing further any further to the formation of an image. The image is obtained by scanning the system across the object.

The simplest arrangement is a series of baffles that may be formed into a variety of configurations. These are generally known as honeycomb collimators, even though the cells are usually square rather than hexagonal. At high energies, the baffles may be formed from a crystal scintillator and pulses from there used to reject detections of radiation from high inclinations. At the low energies the glancing reflection of the radiation can be used to produce a truly imaging collimator. This is called a ‘lobster eye’ focusing collimator, and is essentially a honeycomb collimator curved into a portion of a sphere with a position sensitive detector at its focal surface.

Another system is known as a modulation collimator or *Fourier transform telescope* uses two or more parallel gratings that are separated by a short distance. Since the bars of the gratings alternately obscure the radiation and allow it to pass through, the output as the system scans a point source is a sine wave. To obtain unambiguous positions for the sources, or for the study of multiple or extended sources, several such gratings of different resolutions are combined. The image may then be retrieved from the Fourier components of the output. Two such grating systems can be combined at right angles to give a two-dimensional image.

A third type of system is a simple pinhole camera. A position-sensitive detector is placed behind a small aperture. A better system replaces the pinhole with a mask formed from clear and opaque regions. The pattern of the mask is known, so that when sources cast shadows of it on the detector, their position and structure can be reconstituted in a similar manner to that used for the modulation collimator. The technique is known as *coded mask imaging*, and resolutions of 10 arcmin or better can be reached.

Coincidence detectors

A telescope, in the sense of being a device with directional sensitivity, may be constructed for use at any energy and with any resolution, by using two or more detectors in a line, and by rejecting all detections except those which occur in both detectors and separated by the correct flight time. Two separated arrays of detectors can similarly provide a two-dimensional imaging system.

Occultation

The occultation of a source by the Moon or other object can be used to give very precise positional and structural information.

Reflecting telescopes

At energies below about 100 keV photons may be reflected with up to 50% efficiency off metal surfaces, when their angle of incidence approaches 90°.

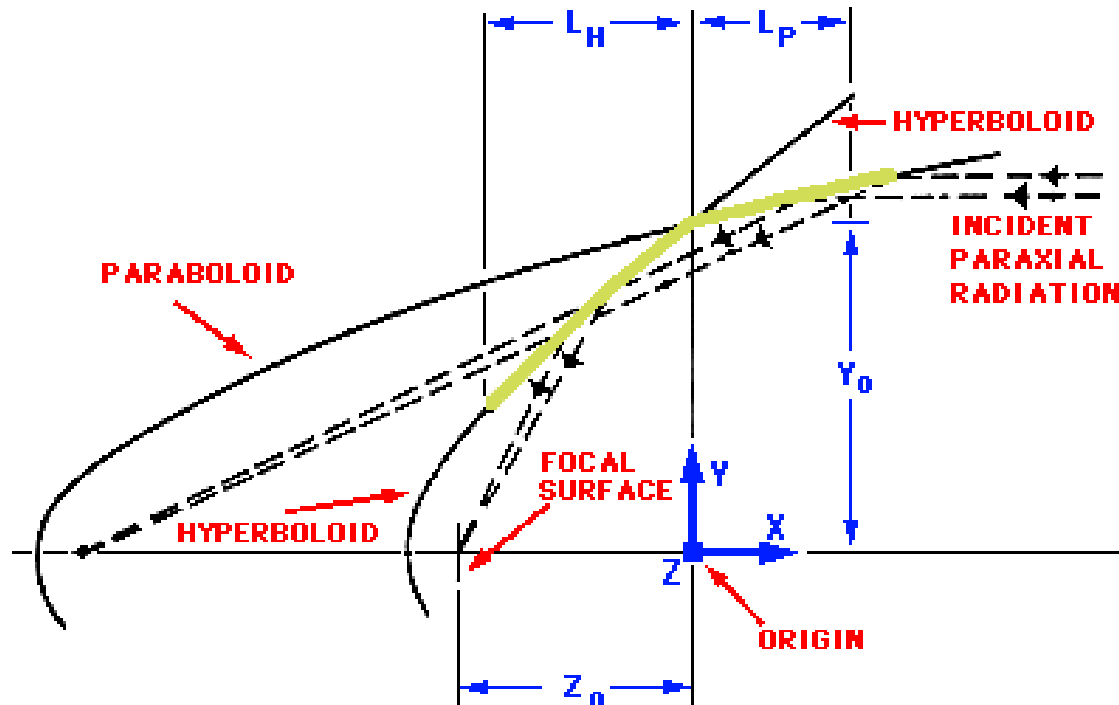


Figure 8.6: Wolter telescope of type I.

Several systems have been devised, but the one which has achieved most practical use is the is formed from the combination of annular sections of very deep paraboloidal and hyperboloidal surfaces known as Wolter telescopes. The aperture of such telescopes is a thin ring, since only the radiation incident on the paraboloid annulus is brought to focus. To increase the effective aperture, and hence sensitivity, several such confocal systems of differing radii may be nested inside each other. For the XMM–Newton spacecraft a total of 58 such nested telescope shells gave a total correcting area of 0.5 m². A schematic of a Wolter type I telescope is shown in figure 8.6.

At lower energies, in the EUV and soft x-ray region, near normal incidence reflection with efficiencies of up to 20% is possible using multilayer coatings. These are formed from tens, hundreds, or even thousands of alternate layers of for example tungsten and carbon, aluminium and gold or magnesium and gold, each about 1 nm thick. The reflection is essentially monochromatic, with the wavelength depending on the orientation of the crystalline structure of the layers and on their thickness. Reflection of several wavelengths can be achieved by changing the thickness of the layers through the stack. The thickest layers are on the top

and reflect the longest, least penetrating wavelengths. Telescopes or relatively conventional design are used with these mirrors, and direct images of the Sun at wavelengths down to 4 nm can be obtained.

8.4.3 Spectroscopy

Many of the detectors described above are intrinsically capable of separating photons of different energies. At photon energies above 10 keV it is only this inherent spectral resolution which can provide information on the energy spectrum. Devices akin to the more conventional idea of a spectroscope, however, can only be used at the low end of the energy spectrum.

Grating spectrometers

Gratings may be either transmission or grazing incidence reflection. The theoretical background for x-ray gratings is identical to that for optical gratings (discussed later). Typical transmission gratings have around 10^3 lines per mm. The theoretical resolution is between 10^3 and 10^4 , but is generally limited in practice to 50 – 100 by other aberrations.

Reflection gratings are also similar in design to their optical counterparts. Their dispersion differs because of the grazing incidence. If the separation of the rulings is d then the path difference ΔP of two rays that are incident on to adjacent rulings is

$$\Delta P = d[\cos \theta - \cos(\theta + \phi)]$$

Expanding this to second order we find

$$\Delta P = \frac{1}{2}d(\phi^2 - 2\theta\phi).$$

In the m th order spectrum, constructive interference occurs for radiation of wavelength λ if

$$m\lambda = \Delta P$$

so that

$$\phi = \left(\frac{2m\lambda}{d} + \theta^2 \right) - \theta$$

and

$$\frac{d\phi}{d\lambda} = \left(\frac{m}{2d} \right)^{1/2}$$

where θ^2 is neglected due to the small size of θ . The dispersion for a glancing incidence reflection grating is therefore inversely proportional to the square root of λ , unlike the case for normal incidence, when the dispersion is independent of wavelength.

Bragg spectrometers

Planes of atoms in a crystal are separated by 0.1 to 10 nm, which is comparable to the wavelength of x-rays. Thus, a beam of x-rays interacts with a crystal in a complex manner. The details of this interaction was first described by the Braggs. Given a distance d between crystal planes and an angle of incidence θ the path difference for rays are multiples of the path difference for two adjacent layers

$$\Delta P = 2d \sin \theta$$

There will be constructive interference for path differences that are whole numbers of wavelengths. So the reflected beam will consist of just those wavelengths, λ , for which this is true

$$m\lambda = 2d \sin \theta.$$

A Bragg spectrometer uses a crystal to produce monochromatic radiation of known wavelength. When a crystal is illuminated by x-rays of mixed wavelengths, only those fulfilling the requirement above will be reflected. The first order, $m = 1$, reflection is by far the strongest. The whole spectrum can be scanned by tilting the crystal at different angles θ . An improved version of the instrument uses a bent crystal and a collimated beam of x-rays so that the approach angle varies over the crystal. The reflected beam then consists of the spectrum at all wavelengths which can be detected in a single observation with a position sensitive detector. Spectral resolutions of up to 10^3 are possible at 1 keV, but large crystal areas are necessary for good sensitivity. Among common crystals in use are lithium fluoride, lithium hydride, tungsten disulphide, graphite, and potassium acid phthalate.

Chapter 9

Imaging

9.1 The inverse problem

A problem that occurs throughout astronomy is how best to interpret noisy data so that the resulting deduced quantities are real and not artifacts of the noise. This problem is termed the inverse problem.

Spurious features may be removed from the image if the effects of the imperfections are known. But since there is uncertainty in both the data and the measurements of the imperfections, there can remain the possibility that features in the final image are artifacts of the noise, or are incompletely removed.

Even a faultlessly constructed telescope will spread the image of a true point source into the Airy diffraction pattern. If the effect of the instrument and other sources of blurring on a point source or its equivalent is known, *i.e.* the PSF as defined below, then an attempt may be made to remove its effect from the data. If we consider a single linear optical device, then we can relate the output field ψ_2 at z_2 to the input ψ_1 at z_1 using a *Greens' function* denoted $P_{21}(\mathbf{x}_2, \mathbf{x}_1)$:

$$\psi_2(\mathbf{x}_2) = \int P_{21}(\mathbf{x}_2, \mathbf{x}_1) d^2x_1 \psi_1$$

If ψ_1 were a δ -function, then the output would be simply given by the function P_{21} , up to a normalization. Thus, P_{21} is known as the *Point Spread Function* or PSF. The process of removing instrumental effects from data can be necessary for any type of measurement, but is perhaps best studied in relation to imaging, when the process is generally known as de-convolution.

9.1.1 De-convolution

The true image *convolves* with the PSF to give the observed image. Inversion of this effect is thus deconvolution. This is most easily illustrated by considering a one-dimensional case.

A one dimensional image, such as a spectrum, may be completely represented by a plot of its intensity against the distance along the image. The PSF may be similarly plotted and may be found, in the case of a spectrum by observing the effect of the spectroscope on a monochromatic source.

If we regard the true spectrum as a collection adjoining monochromatic intensities, then the effect of the spectroscope will be to broaden each monochromatic intensity into the PSF. At a given point in the observed spectrum, some of the original energy will have been

displaced out to nearby wavelengths, while energy will have been added from the spreading out of nearby wavelengths. This process can be written mathematically as the convolution

$$O(\lambda_1) = \int_0^\infty T(\lambda_2)I(\lambda_1 - \lambda_2)d\lambda_2 = T \otimes I \quad (9.1)$$

Where $O(\lambda_1)$ is the intensity in the observed spectrum at λ_1 , $T(\lambda_2)$ is the intensity of the true spectrum at λ_2 , and $I(\lambda_1 - \lambda_2)$ is the response of the instrument at a distance $(\lambda_1 - \lambda_2)$ from the center.

To invert equation 9.1 we take its Fourier transform $\mathcal{F}(O)$ such that

$$\mathcal{F}(O) = \mathcal{F}(T \otimes I) = \mathcal{F}(T) \times \mathcal{F}(I). \quad (9.2)$$

The true spectrum (image or other observable) may be found by taking by inverting equation 9.2 and then taking the inverse Fourier transform

$$T = \mathcal{F}^{-1} \left[\frac{\mathcal{F}(O)}{\mathcal{F}(I)} \right].$$

In practice, there are two difficulties in following this process. First data is sampled at discrete intervals and so is not the continuous function required to complete the Fourier transform, and also it is not available over the complete range from $-\infty$ to $+\infty$. Second the presence of noise will produce ambiguities in the calculated values of T .

The first problem can be overcome by using the discrete versions of the the Fourier transforms as shown in lecture notes 4 on Fourier transforms. Remember that a that has a maximum frequency of f is completely determined by sampling at $2f$ according to the sampling theorem. Thus, the use of the discrete form of the Fourier transform involves no loss of information providing that the sampling frequency $(1/\Delta)$ is twice the highest frequency in the source function. If the source function contains frequencies higher than the Nyquist frequency $(1/2\Delta)$, then these will not be determined by the measurements and the finer detail in the source function will be lost. More seriously, the higher frequency components may beat with the measuring frequency to produce spurious components of frequencies lower than the Nyquist frequency. This phenomenon is known as aliasing.

Some reduction in the noise in the data may be achieved by operating on its Fourier transform. For example, random noise may be reduced by using the optimal (or Wiener) filter defined by

$$W = \frac{[\mathcal{F}(O)]^2}{[\mathcal{F}(O)]^2 + [\mathcal{F}(N)]^2}$$

where $\mathcal{F}(O)$ is the Fourier transform of the observations, without the effect of noise, and $\mathcal{F}(N)$ is the Fourier transform of the random noise. The noise and the noise free signal are separated by assuming the high frequency tail of the power spectrum to be just noise, and then extrapolating linearly back to the lower frequencies. Equation 9.2 becomes

$$T = \mathcal{F}^{-1} \left[\frac{\mathcal{F}(O)W}{\mathcal{F}(I)} \right].$$

9.2 Photography

Photography is hardly used at all in professional astronomy — the last photograph on the AAT was taken in 1999, for example. CCDs now dominate imaging from the ultraviolet to the near infrared. However, photography is perhaps not totally dead, Kitchin's *Astrophysical Techniques* contains good descriptions of photographic process.

9.3 Scanning

Scanning is a quite obvious way of building up a two dimensional image which may be built up by using a point source detector, if the detector is scanned over the image or vice versa. Scanning patterns are normally raster or spiral. Other patterns may also be encountered. Many Earth observation satellites use *push-broom* scanning, in which a linear array of detectors is aligned at right angles to the spacecraft's ground track. The image is built up at the spacecraft's motion move the array to look at successive slices of the swathe of ground over which the satellite is passing.

A more sophisticated technique is to modulate the output of the detector by interposing a mask of some type in the light beam, as previously discussed in the lecture 8 notes on high energy astrophysics where we described modulation collimators and the coded array mask used in x-ray imaging. An improved method is known as Hadamard mask imaging. Its principles can be illustrated by considering one-dimensional images. The mask is placed in the image plane of the telescope, and a lens directs all the light from to a single detector. Thus the output from the system consists of a simple measurement of the intensity passed by the mask. If a different mask is substituted for the first, then a new and in general different reading will be obtained. If the image is to be resolved into N elements, then N such different masks must be used, and N intensity readings determined. If \mathbf{D} is the vector formed from the detector output, \mathbf{I} is the vector of intensities of the elements of the image, and \mathbf{M} the $N \times N$ matrix whose columns each represent one of the masks, then ignoring noise we have

$$\mathbf{D} = \mathbf{IM}$$

and so

$$\mathbf{I} = \mathbf{DM}^{-1}.$$

Thus the original image is obtained by inverting the matrix representing the mask. The improvement over this method over a simple scan lies in its multiplex advantage. The masks usually comprise segments that either transmit or obscure the radiation completely

$$m_{ij} = 0 \quad \text{or} \quad 1.$$

and, on average, about half the total image is obscured by a mask. Thus $N/2$ image segments contribute to the intensity falling on the detector at any one time. Hence, if a given signal to noise ratio is reached in a time T , when the detector observes a single image element, then the total time required to detect the whole image with simple scans is $N \times T$ and is only $\sqrt{2N}T$ for the Hadamard masking system. Thus, the multiplex advantage is approximately $\sqrt{N/2}$ improvement in the exposure length.

One method of finding suitable matrices to reduce construction costs and noise is based on a group of matrices known as the Hadamard matrices (hence the name of the method).

These are matrices whose elements are ± 1 and which have the property

$$\mathbf{H}\mathbf{H}^T = N\mathbf{I}$$

where \mathbf{H} is the Hadamard matrix and \mathbf{I} is the identity matrix.

9.4 Interferometry

The simplest example of interference is given by Young's slits. Suppose two long, narrow, parallel slits are illuminated coherently by monochromatic light from a distant source that lies on the perpendicular axis between the two slits (the optic axis) so that the incident wavefront reaches the slits simultaneously. The waves from the slits fall onto a screen in the distant, Fraunhofer region, and there they interfere. The Fraunhofer interference pattern observed at a point \mathcal{P} , at position r, θ , is proportional to the spatial Fourier transform of the transmission function. If the slits are narrow, we can regard the transmission function as two δ -functions, separated by the slit spacing a , and its Fourier transform will be

$$\psi_{\mathcal{P}} \propto e^{-ika\theta/2} + e^{ika\theta/2} \propto \cos\left(\frac{ka\theta}{2}\right).$$

The energy flux at point \mathcal{P} is the square of this

$$F_{\mathcal{P}} \propto |\psi|^2 c \propto \cos^2(ka\theta/2).$$

The alternating bright and dark illumination in this flux distribution are known as *interference fringes*.

Let us now consider an extended source: Keep the incoming waves perfectly coherent and perfectly planar, but change their incoming direction so that it makes a small angle α to the optic axis. Then the distribution of the energy flux in the Fraunhofer diffraction pattern on the screen will be modified to

$$\begin{aligned} F_{\mathcal{P}} &\propto |e^{-ika(\theta-\alpha)/2} + e^{ika(\theta-\alpha)/2}|^2 \propto \cos^2\left[\frac{ka(\theta-\alpha)}{2}\right] \\ &\propto \{1 + \cos[ka(\theta-\alpha)]\}. \end{aligned}$$

Notice that as the direction α of the incoming wave changes, the locations θ of the bright and dark fringes change. Thus the positions of the fringes carry information about the direction to the source.

An extended source is one whose radiation comes from a finite range of angles α , let us assume $\alpha \ll 1$. Assume further that the source is monochromatic (this can be achieved by filters if necessary), but we will allow the source to have a randomly fluctuating phase $\delta\phi(t)$ in keeping with all realistic monochromatic sources, and shall require that the time-scale on which the phase wanders (the waves coherence time) be very long compared to the waves' period $2\pi/\omega_0$. It is also assumed that, as for most realistic sources, the fluctuating phases in the waves from different directions are completely uncorrelated. The field is then written in the form

$$\psi = e^{ik(kz-\omega_0 t)} \int \psi(\alpha, t) e^{ik\alpha x} d\alpha$$

where $\psi(\alpha, t) = Ae^{-i\delta\phi}$ is the slowly wandering complex amplitude of the waves from direction α . When considering the total flux arriving at a given point (x, z) from two different directions α_1 and α_2 and average it over times long compared to the waves' coherence time, all interference between the two contributions and they superpose incoherently which means that their intensities averaged over time add linearly.

Thus the angularly incoherent light from our extended source is sent through two Young's slits and produces fringes on a screen. Assuming that the coherence time for the light from each source point is very long compared to the difference in light travel time to the screen via the two different slits. Then the light from each source point in the extended source forms sharp interference fringes. However, because contributions from the different directions add incoherently, the flux distribution on the screen is a linear sum of the fluxes from all the source points

$$F_P \propto \int d\alpha I(\alpha) \{1 + \cos[ka(\theta - \alpha)]\}$$

where $I(\alpha)d\alpha \propto |\psi(\alpha, t)|^2 d\alpha$ is the flux incident on the plane of the slits form the infinitesimal range $d\alpha$ of directions. Presume that the range of angles present in the wave, $\Delta\alpha$, is large compared to their bandwidth $\Delta\alpha \gg \Delta\omega/\omega_0$ so whereas the finite but tiny bandwidth produced negligible smearing out of the interference fringes, the finite but small range of directions may produce significant smearing and the minima of F_P might not be very sharp. The fringes non-sharpness and their locations can be quantified by writing the slit produced flux distribution as

$$F_P = F_S [1 + \mathcal{R}\{\gamma_{\perp}(ka)e^{-ika\theta}\}]$$

with

$$F_S \equiv \int d\alpha I(\alpha)$$

is the total flux arriving at the slits from the source, and

$$\gamma_{\perp}(ka) \equiv \frac{\int d\alpha I(\alpha) e^{ika\alpha}}{F_S} \quad (9.3)$$

is known as the radiation's *degree of spatial coherence*. The phase of γ_{\perp} determines the angular locations of the fringes; its modulus determines their depth.

Equation 9.3 says that the degree of spatial coherence from an extended, angularly incoherent source is the Fourier transform of the source's angular intensity pattern. Correspondingly, if one knows the degree of spatial coherence as a function of the distance ka , from it one can reconstruct the source's angular intensity pattern by Fourier inversion:

$$I(\alpha) = F_S \int \frac{d(ka)}{2\pi} \gamma_{\perp}(ka) e^{-ika\alpha}. \quad (9.4)$$

For a given choice of ka , *i.e* a given distance between the slits, γ_{\perp} is a complex number that one can read off the interference fringes as follows: Its modulus is

$$|\gamma_{\perp}| \equiv V = \frac{F_{\max} - F_{\min}}{F_{\max} + F_{\min}}$$

where F_{\max} and F_{\min} are the maximum and minimum values of the flux F_P on the screen; and its phase $\arg(\gamma_{\perp})$ is ka times the displacement $\Delta\theta$ of the centers of the bright fringes from the optic axis. The modulus is called the fringe *visibility* because of it measuring the fractional contrast in the fringes.

9.4.1 Michelson stellar interferometer

Michelson's stellar interferometer implements Young's slits for measuring spatial coherence which Michelson used for measuring the angular diameters of Jupiter's moons and some bright stars in 1920 and a bit earlier. The light is sampled at two small mirrors separated by a variable distance a and then reflected onto a telescope to form interference fringes. It is found that as the separation a between the mirrors is increased, the fringe visibility decreases. If we model a star as circular disk of uniform brightness, then the degree of spatial coherence of the light from it is given as

$$\gamma_{\perp} = 2 \text{jinc}(ka\alpha_r)$$

where α_r is the angular resolution of the star and $\text{jinc}(\xi) = J_1(\xi)/\xi$. Michelson found that for the star Betelgeuse observed at a wavelength $\lambda = 570$ nm, the fringes disappeared when $a \sim 3$ m. Associating this with the first zero of the function $\text{jinc}(x)$, Michelson inferred that the angular radius of Betelgeuse is ~ 0.02 arcsec, which at Betelgeuse's distance 200 pc corresponds to a physical radius $\sim 300 R_S$.

In practice this type of interferometer uses the outputs from many telescopes. However, this is only to reduce the time taken for observations, and it is actually the outputs from pairs of telescopes that are combined to produce the interference effects. Let us compare the resolution achieved with a telescope of diameter D with an interferometer: For a telescope of diameter D two sources are separable if their angular separation is larger than the Rayleigh criterion of

$$\alpha' = \frac{1.22\lambda}{D}.$$

On the other hand the fringe pattern given by two sources separated by

$$\alpha'' = \frac{\lambda}{2d},$$

where d is the separation between the two Young's apertures, will disappear. The fringe pattern will reappear again for an angle $2\alpha''$ and disappear again for $3\alpha''$. Thus the resolution of two apertures is given by the separation of the sources for which the two fringe systems are mutually displaced by half a fringe width. This is given by the angle α'' and the comparison between the telescope and interferometer gives

$$\frac{\alpha''}{\alpha'} = \frac{D}{2.44d}$$

The resolution of the interferometer is almost 2.5 times that of a telescope with the same diameter for point sources!

In order to produce fringes with maximum clarity, the path difference must be close to zero. This is because radiation is never completely monochromatic; any signal will have a certain bandwidth $\Delta\lambda$. For zero path difference at the apertures, all wavelengths will be in phase, and they will interfere constructively. If the path difference is not zero, some wavelengths will be in phase but others will be out of phase since the path difference will equal different numbers of cycles or fractions of cycles at different wavelengths. There will therefore be a mix of constructive and destructive interference, and the observed fringes will have reduced contrast. The path difference for which the contrast in the fringes reduces to zero (*i.e.* no fringes) is called the coherence length, l , given by

$$l = \frac{c}{\Delta\nu} = \frac{\lambda^2}{\Delta\lambda}$$



The VLT Array on the Paranal Mountain

ESO PR Photo 14a/00 (24 Mar. 2000)

©European Southern Observatory



Figure 9.1: The VLT Array on the Paranal Mountain which can be used as a stellar interferometer.

For $\lambda = 500$ nm and $\Delta\lambda = 1$ nm, we have a coherence length of 0.25 mm, for white light $\lambda = 300$ nm this reduces to less than a μm , but in the radio region it can be large; at $\nu = 1.5$ GHz and $\Delta\nu = 10$ MHz it is fully 30 m. The path difference to the apertures, or their equivalent, must be kept to a small fraction of the coherence length. Michelson achieved this by the use of adjustable glass wedges in his interferometer where the path difference was small. However, modern telescopes can be over 100 m apart for optical telescopes and up to thousands of kilometers for very-long-baseline radio interferometry, and a complex system of delay lines must be built in order to achieve coherence, or alternately afterwards during data processing in the case of radio observations where also the phase can be recorded.

Very stringent requirements on the stability and accuracy are required in order for this technique to work. The path difference of the slits must not be greater than a small fraction of the coherence length. Vibrations and scintillation are additional limiting factors.

A proposal for the future is to use *nulling interferometry* based in space. This would use destructive interference to suppress the bright central object in order to look for the much dimmer companions such as Earth-like planets. To achieve this around stars 10 pc or more

away one would need baselines of order 50 m and observations taking a few hours with a four element array of telescopes.

9.4.2 Michelson radio interferometer

There is no difference in principle between a radio and an optical interferometer when they are used to measure the separation of double source, or the diameters of uniform objects. However, the output from a radio telescope contains both the amplitude and the phase of the signal, so that complete imaging of the source is possible. This is achieved by using equation 9.4 to perform the Fourier inversion of the lateral degree of coherence $\gamma_{\perp}(\mathbf{a})$, which must be measured for a variety of values of the relative separation vector \mathbf{a} of the telescopes perpendicular to the direction of the source. As the earth rotates, this vector will trace out half an ellipse in the two-dimensional \mathbf{a} plane every twelve hours. Since the source intensity is real equation 9.4 implies that $\gamma_{\perp}(-\mathbf{a}) = \gamma_{\perp}^*(\mathbf{a})$. By changing the spacing between the telescopes the degree of coherence can be well sampled. In practice a modern interferometer has many more than two telescopes. The Very Large Array (VLA) in New Mexico has 27 individual telescopes arranged in a ‘Y’ pattern and operating simultaneously. The degree of coherence can thus be measured simultaneously over $27 \times 26/2 = 351$ different relative separations. The maximum baseline of the VLA is 36 km.

9.4.3 Speckle interferometry

Speckle interferometry works by obtaining images of the object sufficiently rapidly to freeze the blurring of the image that arises from atmospheric scintillations. The total image then consists of a large number of small dots or speckles, each of which is a diffraction-limited image for some objective diameter up to and including the diameter of the actual objective.

Consider the effect of seeing upon the wavefront of the object. Assume that the wavefront is initially planar and coherent, then the main effect of scintillation is to introduce differential phase delays across it. A typical cell size is 0.1 m and the scintillation frequency is in the range 1 – 100 Hz. Thus some 100 atmospheric cells will affect an average image from a 1 m telescope at any given instant. These will be rapidly changing. An exposure of a few milliseconds will freeze the image motion, and the observed image is then just the resultant of the contributions from the atmospheric cells across the telescope objective at the moment. The large number of cells renders it highly probable that some of the phase delays will be similar and so some of the contributions to the image will be in phase with each other. These particular contributions will have been distributed over the objective in a random manner. Considering two such contributions, we have a simple interferometer, and the two beams of radiation will combine in the image plane to produce results identical with those of an interferometer whose baseline is equal to the separations of the contribution on the objective. The smallest speckles in the total image therefore have the diffraction limited resolution of the whole objective.

Chapter 10

Spectroscopy

Practical telescopes are usually based upon one or other of two quite separate optical principles — interference and differential refraction. In reality, the author has never seen a prism based spectrograph professionally used . . . There are also some hybrid designs according to Kitchin's *Astrophysical Techniques*.

10.1 Diffraction gratings

The operating principle of diffraction gratings relies on the effects of diffraction and interference of light waves.

A diffraction grating can be modeled as a finite series of alternating transparent and opaque, long, parallel stripes. Let there be N transparent and opaque stripes each of width $a \gg \lambda$. We can idealize them as infinitely long so their diffraction pattern is one-dimensional.

The idealized N -slit grating can be considered as an infinite series of δ -functions with separation $2a$ convolved with the transmission function for a single slit,

$$\int_{-\infty}^{\infty} \left[\sum_{n=-\infty}^{\infty} \delta(y - 2an) \right] t_1(x - y) dy,$$

that is multiplied by the global aperture function of the size of the grating

$$\begin{aligned} H(x) &= 1 & |x| < Na \\ &= 0 & |x| > Na. \end{aligned}$$

In total this gives an aperture function for the entire grating

$$t(x) = \left(\int_{-\infty}^{\infty} \left[\sum_{n=-\infty}^{\infty} \delta(y - 2an) \right] t_1(x - y) dy \right) H(x)$$

The final pattern is then given by remembering that $\psi_{\mathcal{P}}$ is given by the Fourier transform of $t(x)$

$$\psi_{\mathcal{P}}(\theta) \propto \int e^{-ikx\theta} t(x) dx.$$

The convolution theorem says that the Fourier transform of two functions is the product of the functions' Fourier transforms, and conversely. The diffraction pattern of the infinite

series of δ -functions with spacing $2a$ is itself an infinite series of δ -functions, but with the reciprocal spacing $2\pi/(2ka) = \lambda/2a$. This is multiplied by the Fourier transform of the single slit, and then convolved with the Fourier transform of $H(x)$, $\bar{H}(\theta) \propto \text{sinc}(Nka\theta)$. The diffracted energy flux is $|\psi_{\mathcal{P}}|^2$: what the grating does is channel the incident radiation into a few equally spaced beams with directions $\theta = \pi m/ka$, where m is an integer known as the *order* of the beam. Each of these beams has the shape given by $|\bar{H}(\theta)|^2$: a sharp centered peak with a half width (distance from the center of the peak to the first null of the intensity) $\lambda/2Na$, followed by a set of *side lobes* whose intensities are $\propto N^{-1}$.

A spectrograph can therefore be built based on the fact that the deviation angle $\theta = \pi m/ka$ of these beams are proportional to $k^{-1} = \lambda/2\pi$. We can find the wavelength resolution of this (idealized) grating by focusing attention the m 'th order beams at two wavelengths λ and $\delta\lambda$ located at $\theta = m\lambda/2a$ and $m(\lambda + \delta\lambda)/2a$. We can distinguish the beams from each other when their separation $\delta\theta = m\delta\lambda/2a$ is at least as large as the angular distance $\lambda/2Na$ between the maximum of each beam's diffraction pattern and its first minimum:

$$\frac{\lambda}{\delta\lambda} \lesssim \mathcal{R} \equiv Nm$$

\mathcal{R} is called the gratings *chromatic resolving power*.

In Kitchin's *Astrophysical Techniques* the small angle approximation ($\theta \approx \sin\theta$) is not used, and therefore a slightly different expression for the fringe pattern arises

$$I(\theta) \propto \left[\frac{\sin^2(\pi D \sin\theta/\lambda)}{(\pi D \sin\theta/\lambda)^2} \right] \left[\frac{\sin^2(N\pi d \sin\theta/\lambda)}{\sin^2(\pi d \sin\theta/\lambda)} \right]$$

where now D is the size of an aperture and d is the distance between the apertures. The angular positions of the principal maxima are given by

$$\sin\theta = (m\lambda/d)$$

and the zero intensities are found at

$$\sin\theta = (m'\lambda/Nd)$$

excluding those positions $m' = mN$ that are the positions of the principle maxima. The angular width of a principal maximum is therefore (since

$$\frac{d\theta}{dm'} = \frac{\lambda}{Nd \cos\theta}$$

and the change in m' is 2) given by

$$W = \frac{2\lambda}{Nd \cos\theta}.$$

Thus, the width of a fringe is proportional to N^{-1} , while its peak intensity is proportional to N^2 . The distance from the peak to the first zero W' is half of this and the spectral resolution is then

$$\begin{aligned} W_{\lambda} &= W' \frac{d\lambda}{d\theta} = \frac{\lambda}{Nd \cos\theta} \frac{d \cos\theta}{m} \\ &= \frac{\lambda}{Nm} \end{aligned}$$

The spectral resolution improves with the order. The chromatic resolving power is again

$$\mathcal{R} = \frac{\lambda}{W_\lambda} = Nm.$$

Note that it is independent of the width and the spacing of the apertures. Note that at high order the spectra are overlapping. The difference in wavelength between two superimposed wavelengths from adjacent spectral orders is called the free spectral range, Σ . If λ_1 and λ_2 are two such superimposed wavelengths then

$$\sin^{-1} \left[\frac{m\lambda_1}{d} \right] = \sin^{-1} \left[\frac{(m+1)\lambda_2}{d} \right],$$

or for small angles

$$\Sigma = \lambda_1 - \lambda_2 \approx \frac{\lambda_2}{m}.$$

For small m , σ is large.

Some spectrometers, such as those based on Fabry-Perot etalons and echelle gratings, operate at very high spectral order and both of the overlapping wavelengths may be desired. Then it is necessary to use a cross disperser so that the final spectrum consists of a two-dimensional array of short sections of the spectrum.

Typical gratings for astronomical use have between 1000 and 50 000 grooves in total. They are used at order ranging from one up to two hundred or so. Thus the spectral resolutions range from 10^3 to 10^5 . Diffraction gratings can be used in either reflection or transmission modes, most astronomical spectrometers are based on reflection gratings. Often, the grating is inclined to the incoming beam of light, in which case a constant term, $d \sin i$, is added to the path differences, where i is the angle made by the incoming beam to the normal of the grating. Thus we find

$$\theta = \sin^{-1} \left[\left(\frac{m\lambda}{d} \right) - \sin i \right]$$

often called the grating equation.

The basic setup of a spectrometer is that the grating is illuminated by parallel light that is usually obtained by placing a slit at the focus of a collimating lens (but sometimes by allowing light from a very distant object to fall directly on the grating). After reflection from the grating, the light is focused by the imaging lens (camera lens) to form the required spectrum. The collimator and imaging lens may be simple lenses or they may be achromats or mirrors.

If x is the linear distance along the spectrum from some reference point, then we have for an achromatic imaging element of focal length f_2

$$\frac{dx}{d\lambda} = f_2 \frac{d\theta}{d\lambda}$$

where θ is small. Thus, the linear dispersion within each spectrum is given by

$$\frac{dx}{d\lambda} = \pm \frac{mf_2}{d \cos \theta},$$

or, since θ varies little over an individual spectrum

$$\frac{dx}{d\lambda} \approx \text{constant.}$$

More commonly, the reciprocal linear dispersion, $d\lambda/dx$, is used. It usually has values in the range 10^{-7} to 10^{-5} .

The resolving power of a spectroscope is limited by the spectral resolution of the grating, the resolving power of the optics, and by the projected slit width. The spectrum is formed from an infinite number of monochromatic images of the entrance slit. The width of these images, S , is given by

$$S = s \frac{f_2}{f_1}$$

where s is the slit width, f_1 is the collimator's focal length and f_2 is the imaging element's focal length. The entrance slit must have a physical width of s_{\max} or less, if it is not to degrade the spectral resolution, where

$$s_{\max} = \frac{\lambda f_1}{Nd \cos \theta}.$$

When the grating is fully illuminated, the imaging element will intercept a rectangular beam of light. The width of the beam, D , is given by $D = L \cos \theta$ where L is the length of the grating and θ is the angle of the exit beam to the normal of the plane of the grating. The diffraction limit is just that of a rectangular slit of width D : the Rayleigh limit W'' is then given by

$$W'' = \frac{f_2 \lambda}{D} = \frac{f_2 \lambda}{L \cos \theta}.$$

Optimum resolution occurs when $S = W''$, i.e. when

$$s = \frac{f_1 \lambda}{D} = \frac{f_1 \lambda}{L \cos \theta}.$$

10.1.1 Blazing

It is common to design a grating so that light is concentrated into a smaller number of orders. In this technique, called blazing, the individual mirrors that comprise the grating are angled so that they concentrate into a narrow solid angle. For instruments based on gratings at low orders, the angle of the mirrors is arranged so that the light is concentrated into the spectrum to be used, and by this means 90% efficiency can be achieved.

10.1.2 Shadowing

If the incident and/or reflected light makes a large angle to the normal of the grating, then the step-like nature of the surface will cause a significant fraction of the light to be intercepted by the vertical portions of the grooves, and so lost to the final spectrum.

10.1.3 Rowland circle

Curved reflection gratings are often used. By making the curve that of an optical surface, the grating itself can be made to fulfill the function of the collimator and/or the imaging element of the spectroscope, thus reducing light losses. The simplest optical principle employing a curved is due to Rowland. The slit, grating and spectrum all lie on a single circle called the Rowland circle. This has a diameter equal to the radius of the curvature of the grating.

10.1.4 Echelle gratings

By increasing the angle of a blazed grating, we obtain an echelle grating. This is illuminated more or less normally to the groove surfaces and therefore at a very large angle to the normal to the grating. It is usually a very coarse grating — ten lines per millimeter or so — so that the separation of the apertures d is very large. The reciprocal linear dispersion

$$\frac{d\lambda}{dx} = \pm \frac{d \cos \theta}{mf_2}$$

is therefore also very large. Such gratings concentrate the light into many overlapping high-order spectra, and the resolution is very high. An echelle grating requires second low dispersion grating or prism whose dispersion is perpendicular to that of the echelle and is called a cross disperser in order to separate the orders. Alternately, one can use filters to remove unwanted orders.

10.1.5 Littrow spectrosopes

A type of arrangement often used for long focus spectrosopes in laboratory and solar work, is called the Littrow or auto-collimating spectroscope. A single lens, or occasionally a mirror, acts as both the collimator and imaging element.

10.1.6 Ghosts and other anomalies

A grating spectrum generally suffers from unwanted additional features superimposed upon the desired spectrum. Such features are usually much fainter than the main spectrum and are called ghosts. They arise from a variety of causes. They may be due to overlapping spectra from higher or lower orders, or to the secondary maxima associated with each principal maximum. The first of these can be eliminated by the use of filters since the overlapping ghosts are of different wavelengths. The second source is usually unimportant since the secondary maxima are very weak when more than a few tens of apertures are used, though they will contribute to the wings of the PSF. Of more general importance are the ghosts that arise through errors in the grating. Such errors most commonly take the form of periodic variations in the groove spacing. A variation with a single period gives rise to *Rowland ghosts* that appear as faint lines close to and on either side strong spectral lines. Their intensity is proportional to the square of the order of the spectrum. If the error is multi-periodic, then *Lyman ghosts* of strong lines may appear. These are similar to Rowland ghosts, except that they can be formed at large distances from the line that is producing them.

Woods anomalies also sometimes occur, these are due to light that should go into spectral orders behind the grating reappearing with lower order spectra. They are rarely important in efficiently blazed gratings.

10.2 Prisms

Pure prism-based spectrosopes are rarely encountered today. However, they are used in conjunction with gratings in some modern instruments. Prisms are often used as cross-dispersers for high spectral order telescopes based upon echelle gratings or etalons, and may also be used non-spectroscopically for folding light beams.

When monochromatic light passes through an interface between two transparent isotropic media at a fixed temperature, then we can apply Snell's law relating the angle of incidence, i , to the angle of refraction r at that interface

$$\mu_1 \sin i = \mu_2 \sin r$$

where μ_1 and μ_2 are constants that are characteristic of the two media. When $\mu_1 = 1$, i.e. in a vacuum (but close enough in most gases including air), we have

$$\frac{\sin i}{\sin r} = \mu_2$$

and μ_2 is known as the refracting index of the second medium. Thus with a proper second medium formed as a prism we can separate light into a spectrum. This is explained in great detail in Kitchin's *Astrophysical Techniques*.

10.3 Interferometers

10.3.1 Michelson interferometer

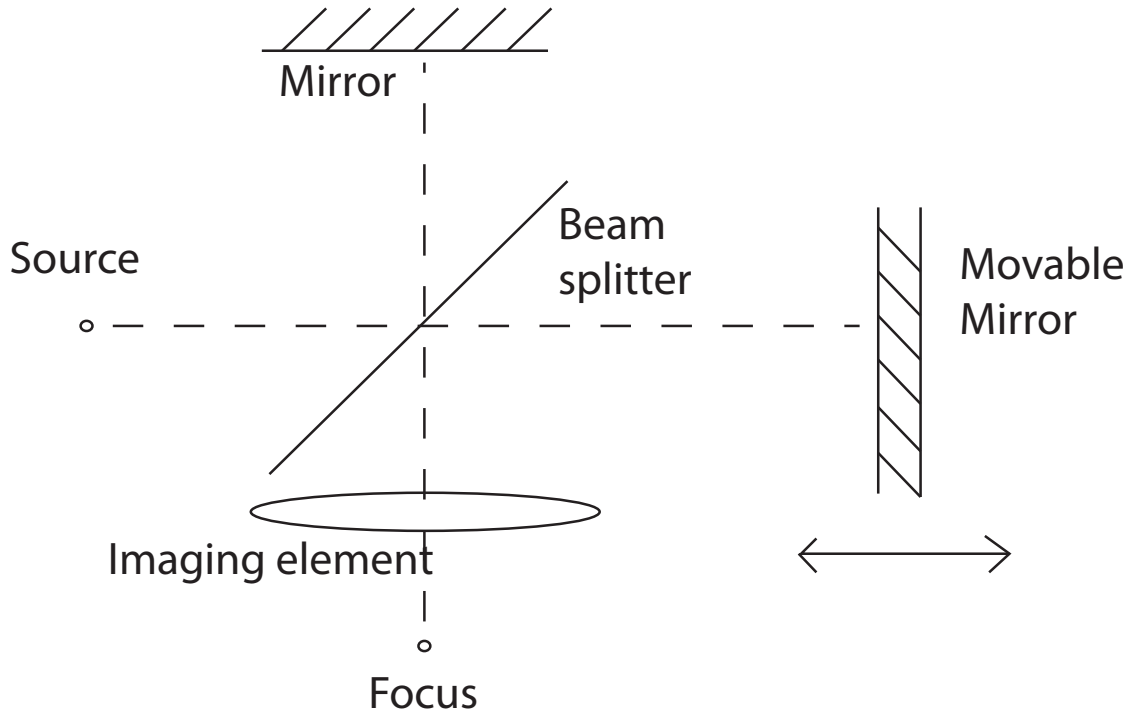


Figure 10.1: Optical pathway of a Michelson interferometer

The Michelson interferometer is similar to the device used by Michelson and Morley to try to detect the Earth's motion through the aether. The light from a source is split into two beams by the beam splitter, and then recombined as shown in figure 10.1. For a particular position of the movable mirror and with a monochromatic source, there will be a path difference ΔP between the two beams at focus. The flux at focus is then

$$F_{\Delta P} = F_m [1 + \cos(k\Delta P)]$$

where F_m is the maximum flux. When the mirror is moved the path difference will change and the final flux will pass through a series of maxima and minima. The change of the interference of the beam with itself is giving information on the wavelength of the beam $\lambda = 2\pi/k$. This will also be true for chromatic sources.

Consider a Michelson interferometer in which the path difference is ΔP observing a source whose flux at wavelength λ is F_λ . The total flux for a given path difference is then

$$\begin{aligned} F_{\Delta P} &= \int_0^\infty F_{\Delta P}(\lambda) d\lambda \\ &\propto \int_0^\infty F(\lambda) d\lambda + \int_0^\infty F(\lambda) \cos\left(\frac{2\pi\Delta P}{\lambda}\right) d\lambda \end{aligned}$$

The first term on the right hand side is independent of the path length and is just proportional to the average flux of the image. We will therefore disregard it and only consider the deviations from the average level. Thus

$$\begin{aligned} F(\Delta P) &\propto \int_0^\infty F(\lambda) \cos\left(\frac{2\pi\Delta P}{\lambda}\right) d\lambda \\ &\propto \int_0^\infty F(\nu) \cos\left(\frac{2\pi\Delta P\nu}{c}\right) d\nu, \end{aligned}$$

the latter in terms of frequency. Notice that this is very similar to the real part of the Fourier transform

$$\begin{aligned} \mathcal{F}[f(t)] &= F(u) = \int_{-\infty}^\infty f(t) e^{-i2\pi ut} dt \\ &= \int_{-\infty}^\infty f(t) \cos(2\pi ut) dt - i \int_{-\infty}^\infty f(t) \sin(2\pi ut) dt \end{aligned}$$

so when we define $F(-\nu) = F(\nu)$ we can write the observed flux as the Fourier transform of the desired spectral signal $F(\nu)$

$$\begin{aligned} F(\Delta P) &\propto \frac{1}{2} \int_{-\infty}^\infty F(\nu) \cos\left(\frac{2\pi\Delta P\nu}{c}\right) d\nu \\ &\propto \operatorname{Re} \left\{ \int_{-\infty}^\infty F(\nu) \exp\left[-i\left(\frac{2\pi\Delta P}{c}\right)\nu\right] d\nu \right\} \end{aligned}$$

In other words, to recover $F(\nu)$, we need only to take the real part of the inverse transform

$$\operatorname{Re} \{ \mathcal{F}^{-1}[F(\Delta P)] \} = F(\nu)$$

or more specifically

$$F(\nu) \propto \int_{-\infty}^\infty F\left(\frac{2\pi\Delta P}{c}\right) \cos\left(\frac{2\pi\Delta P}{c}\right) d\Delta P$$

If we define $F(-2\pi\Delta P/c) = F(2\pi\Delta P/c)$, we can do the integral from 0 to ∞ and thus recover the spectrum.

In practice it is not possible to scan over path differences from 0 to ∞ and, in addition, measurement are made at discrete locations rather than continuously. These limitations are

reflected in a reduction in the resolving power of the instrument. To obtain an expression for the resolving power, consider the Michelson interferometer as equivalent Young's slits (see lecture 9) since its image is the result of two interfering beams of light. Since the order is given by $m = \Delta P/\lambda$ and $N = 2$ we find

$$W_\lambda = \frac{\lambda}{Nm} = \frac{\lambda^2}{2\Delta P}.$$

When the movable mirror moves a distance x , ΔP ranges from 0 to $2x$, and we must take the average value of ΔP . Thus the spectral resolution is

$$W_\lambda = \frac{\lambda^2}{2x}$$

and the chromatic resolving power is

$$\mathcal{R} = \frac{\lambda}{W_\lambda} = \frac{2x}{\lambda}$$

Since x can be as much as 2 m, we obtain resolutions of up to 4×10^6 for the visible region.

The sampling intervals must be sufficiently frequent to preserve the resolution, but not more frequent. If the final spectrum extends from λ_1 to λ_2 then the number of useful intervals is given by

$$n = \frac{\lambda_1 - \lambda_2}{W_\lambda}$$

so that if λ_1 and λ_2 are not too different we have

$$n \approx \frac{8x(\lambda_1 - \lambda_2)}{(\lambda_1 + \lambda_2)^2}$$

However, since the inverse Fourier transform gives both $F(\nu)$ and $F(-\nu)$, the total number of disparate intervals in the final transform is $2n$. Thus, the interval between successive positions of the movable mirror, Δx , where the flux is measured is

$$\Delta x = \frac{(\lambda_1 + \lambda_2)^2}{16(\lambda_1 - \lambda_2)}.$$

10.3.2 Fabry-Pérot interferometer

Fabry-Pérot interferometry is based on trapping monochromatic light between two highly reflecting surfaces. Let us consider the situation sketched in figure 10.2 where we have drawn two reflecting surfaces that are parallel and a distance d apart. In between these plates there is a transparent medium with an index of refraction n , while outside the plates it is n' . Such a device is called an *étalon*. One example is a glass slab in air, another is a vacuum maintained between two glass mirrors. Suppose a plane wave with circular frequency ω is incident on one of the reflecting surfaces, where it is partially reflected and partially transmitted. The transmitted wave will propagate through to the second surface where it will be partially reflected and partially transmitted. The reflected portion will return to the first surface to be split, and so on. The resulting total fields in the slab and beyond could be computed by summing the series of sequential reflections and transmission. Alternately one can proceed as below:

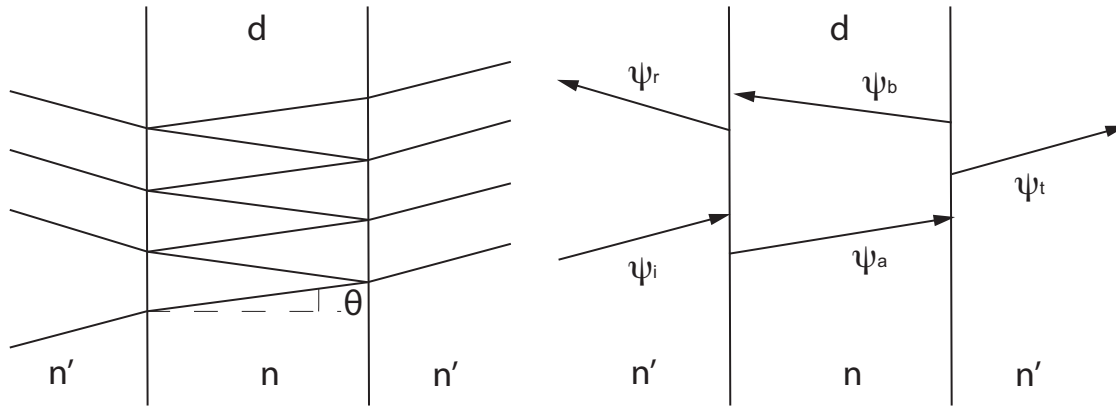


Figure 10.2: Schematic form of a Fabry-Pérot interferometer. The light enters from the left and exits to the right (and left).

The series if summed will lead to five waves shown in the right panel of figure 10.2: an incident wave (ψ_i), a reflected wave (ψ_r), a transmitted wave (ψ_t), and two internal waves (ψ_a, ψ_b) with fields measured at the first surface.

Introduce further reflection and transmission coefficients r and t for waves incident on the slab from outside. Likewise, introduce r' and t' for waves incident on the slab from inside. These coefficients are functions of the angles of incidence and the polarization. They can be computed using electromagnetic theory, but we need not do so here.

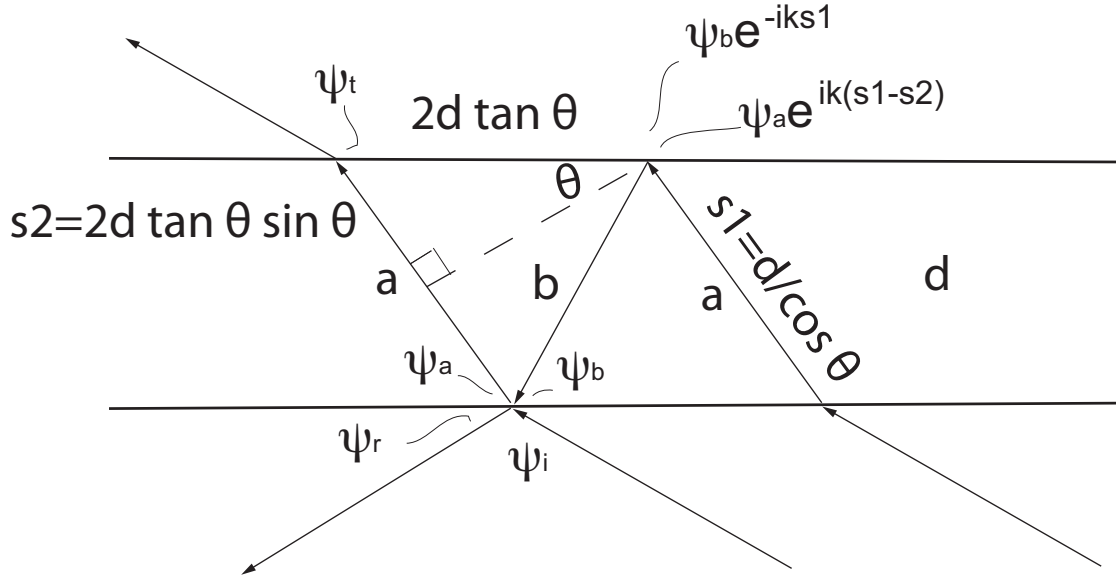


Figure 10.3: Construction for calculating the phase differences across each slab for the two internal waves in an etalon.

At the first surface we can write

$$\begin{aligned}\psi_r &= r\psi_i + t'\psi_b \\ \psi_a &= t\psi_i + r'\psi_b\end{aligned}\tag{10.1}$$

Geometry shows the the waves on the second surface are as in figure 10.3, and correspondingly the relationships between the ingoing and outgoing waves are

$$\begin{aligned}\psi_b e^{-iks_1} &= r' \psi_a e^{ik(s_1 - s_2)} \\ \psi_t &= t' \psi_a e^{iks_1}\end{aligned}\quad (10.2)$$

where $k = n\omega/c$ is the wave number in the slab and

$$s_1 = d/\cos\theta, \quad s_2 = 2d\tan\theta\sin\theta$$

with d the thickness of the slab and θ the angle that the wave fronts inside the slab make to the slab's faces.

In solving for ψ_t and ψ_r as functions of ψ_i we will need relations between the reflection and transmission coefficients. Consider the limit in which the slab thickness $d \rightarrow 0$. In this limit $s_1 = s_2 = 0$ and the slab must become transparent so

$$\psi_r = 0, \quad \psi_t = \psi_i.$$

From the equations above we can then arrive at

$$r' = -r, \quad tt' - rr' = 1. \quad (10.3)$$

Since there is no mechanism to produce a phase shift as the waves propagate across a perfectly sharp boundary, we can also expect that r , r' , t , and t' are real.

Returning to the case of $d \neq 0$, we find that by solving the equations 10.1 and 10.2, as well as the reciprocity relations 10.3 we can derive

$$\psi_r = \frac{r(1 - e^{i\phi})}{1 - r^2 e^{i\phi}} \psi_i, \quad \psi_t = \frac{(1 - r^2)e^{i\phi}}{1 - r^2 e^{i\phi}} \psi_i$$

where

$$\phi = 2n\omega d \cos\theta/c$$

It is very interesting to find the total reflection and transmission coefficients for the flux:

$$\begin{aligned}R &= \frac{|\psi_r|^2}{|\psi_i|^2} = \frac{2r^2(1 - \cos\phi)}{1 - 2r^2\cos\phi + r^4} \\ T &= \frac{|\psi_t|^2}{|\psi_i|^2} = \frac{(1 - r^2)^2}{1 - 2r^2\cos\phi + r^4}\end{aligned}\quad (10.4)$$

From these expressions it is clear that

$$R + T = 1$$

which says that the energy flux reflected from the slab plus that transmitted is equal to that impinging on the slab. It is actually the reciprocity relations that have enforced this energy conservation.

Let us now introduce the finesse

$$\mathcal{F} \equiv \pi r / (1 - r^2),$$

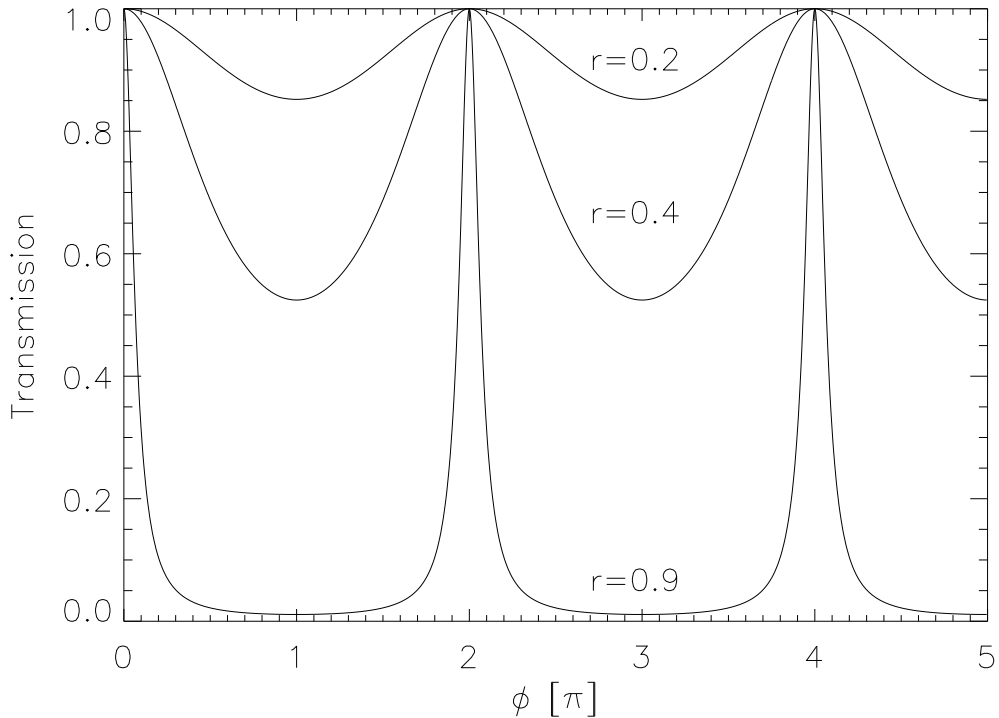


Figure 10.4: Transmission coefficient for an etalon as a function of the phase ϕ for reflectivities of $r = 0.2$, $r = 0.4$, and $r = 0.9$.

in terms of which

$$T = \frac{1}{1 + (2\mathcal{F}/\pi)^2 \sin^2 \frac{1}{2}\phi}$$

Suppose that the etalon is highly reflecting, so $r \simeq 1$. Then \mathcal{F} is very large and the transmissivity T exhibits resonances. Unless $\sin \frac{1}{2}\phi$ is small, almost all the incident light is reflected by the etalon. The exception is when $\sin \frac{1}{2}\phi$ is small, then the total transmission can be large, even unity in the limit $\sin \frac{1}{2}\phi \rightarrow 0$. Notice that for large finesse, the half width of the resonance (the value of $\delta\phi \equiv \phi - \phi_{\text{resonance}}$ where T falls to 1/2) is $\delta\phi_{1/2} = \pi/\mathcal{F}$. The separation between the resonances, the free spectral range, is $\delta\phi = \pi$, so the finesse is the ratio of the free spectral range to the resonance half width.

The etalon can be tuned to a particular frequency by varying either the slab width d or the angle of incidence of the radiation (and thus θ inside the etalon). Either way very good chromatic resolving power can be achieved. One can say that waves with nearly the same frequencies are resolved by an etalon when the half power point of the transmission coefficient of one wave coincides with the half power point of the transmission coefficient of the other. *I.e.* using equation 10.4 the phases for the two frequencies must differ by $d\phi \sim 2\pi/\mathcal{F}$; and since $\phi = 2n\omega d \cos \theta/c$, the chromatic resolving power is

$$\mathcal{R} = \frac{\lambda}{\delta\lambda} = \frac{2\pi nd}{\lambda_{\text{vac}} \delta\phi} = \frac{2nd\mathcal{F}}{\lambda_{\text{vac}}}$$

where λ_{vac} is the wavelength in vacuum — *i.e.* outside the etalon. The finesse \mathcal{F} can be

regarded as a quality factor for the resonator. It is roughly the number of times a typical photon traverses the etalon before escaping.

10.4 Exercises

1. The overlapping of multiple orders means that some method — a blocking filter or a detector of limited spectral sensitivity — must be used to eliminate unwanted orders. Suppose we limit the response of a detector to wavelengths shorter than some λ_{\max} . If we attempt to observe the spectrum in order m with this detector, the spectrum from order $m + 1$ overlaps λ_{\max} so that photons of wavelength

$$\lambda_{m+1} = \frac{m}{(m+1)} \lambda_{\max}$$

are deposited at the same θ location. We therefore would insert a filter to block all light with wavelengths shorter than λ_{\max} to eliminate the overlap. What is the free spectral range at λ_{\max} ? Explain why the free spectral for a particular order, m , and maximum wavelength λ_{\max} is not restricted by overlapping light from order $m - 1$.

2. Compute the free spectral range of grating orders 50, 100, and 101 if $\lambda_{\max} = 600$ nm in each case.
3. Make a sketch of a spectroscope, indicating the focal lengths of the collimator, f_1 , and imaging (camera) lens, f_2 , the position of the entrance slit, the grating and the detector. Also make a sketch of the expected input and output images of the spectrograph, both parallel and perpendicular to the plane of the sketch.
4. Show, or explain, why the width of a monochromatic image of the entrance slit is given by $S = sf_2/f_1$ where s is the width of the entrance slit.
5. What is the step size needed in case one looks for the spectrum in the range 500–550 nm? or in the range 2000 – 2050 nm? Assume that the movable mirror moves 2 m. What are the resolving powers \mathcal{R} for these examples?
6. Derive the relations for ψ_r and ψ_t as functions of r , the incident field ψ_i and the ‘angle’ $\phi = 2n\omega d \cos \theta/c$.
7. Compute the reflection R and transmission T flux coefficients.
8. Find the expression for the transmission coefficient in terms of the finesse. Using IDL plot T as a function of ϕ with $r = 0.2, 0.4, 0.9$.

Chapter 11

Polarimetry

The discovery of polarized light from astronomical sources goes back to the early 1800's when Arago detected its presence in moonlight. However, polarization is quite technically difficult to detect and the lack of any expectation of finding polarized light from stars meant that the field developed quite slowly. On the other hand, many phenomena contribute to the polarization of radiation and its observation can accordingly give information on a wide range of basic causes.

11.1 Stokes parameters

Polarization of radiation is simply the non-random angular distribution of the electric vectors of the photons in a beam of photons. Two cases are distinguished; linear and circular polarization. In the former the electric vectors are all parallel and their direction is constant, in the latter the angle of the electric vector rotates with time at the frequency of the radiation. These are not really physically distinct phenomena however, and all types of radiation may be considered different aspects of partially elliptically polarized radiation. This also has two components, one of which is unpolarized, the other being elliptically polarized. Elliptically polarized light is similar to circularly polarized light in that the electric vector traces out an ellipse.

The properties of partially elliptically polarized light are completely described by the four *Stokes parameters*. These fix the intensity of unpolarized light, the degree of ellipticity, the direction of the major axis of the ellipse, and the sense (left- or right-handed) of the elliptically polarized light. We can decompose the electric vector of elliptically polarized light travelling along the z -axis onto the x and y axes

$$\begin{aligned} E_x(t) &= e_1 \cos(2\pi\nu t) \\ E_y(t) &= e_2 \cos(2\pi\nu t + \delta) \end{aligned}$$

where ν is the frequency of the radiation, δ is the phase difference between the x and y components and e_1 and e_2 are the amplitudes of the x and y components. It is tedious but straightforward to show that

$$a = \left(\frac{(e_1^2 + e_2^2)}{1 + \tan^2[\frac{1}{2} \sin^{-1} \{ [2e_1 e_2 / (e_1^2 + e_2^2)] \sin \delta \}]} \right)^{1/2}$$

$$b = a \tan \left[\frac{1}{2} \sin^{-1} \left\{ \left[\frac{2e_1 e_2}{e_1^2 + e_2^2} \right] \sin \delta \right\} \right]$$

$$a^2 + b^2 = e_1^2 + e_2^2$$

$$\psi = \frac{1}{2} \tan^{-1} \left\{ \left[\frac{2e_1 e_2}{e_1^2 - e_2^2} \right] \cos \delta \right\}$$

where a and b are the semi-major and semi-minor axes of the polarization ellipse and ψ is the angle between the x axis and the major axis of the polarization ellipse. The Stokes parameters are then defined by

$$Q = e_1^2 - e_2^2 = \frac{a^2 - b^2}{a^2 + b^2} \cos(2\psi) I_p$$

$$U = 2e_1 e_2 \cos \delta = \frac{a^2 - b^2}{a^2 + b^2} \sin(2\psi) I_p$$

$$V = 2e_1 e_2 \sin \delta = \frac{2ab}{a^2 + b^2} I_p$$

where I_p is the intensity of the polarized component of the light. From the equations above we have

$$I_p = (Q^2 + U^2 + V^2)^{1/2}$$

The fourth Stokes parameter, I , is the total intensity of the partially polarized light

$$I = I_u + I_p.$$

The degree of polarization, π , of the radiation is given by

$$\pi = \frac{(Q^2 + U^2 + V^2)^{1/2}}{I} = \frac{I_p}{I}$$

while the degree of linear polarization, π_L , and the degree of ellipticity, π_e , are

$$\pi_L = \frac{(Q^2 + U^2)^{1/2}}{I}$$

$$\pi_e = \frac{V}{I}.$$

When $V = 0$ we have linearly polarized radiation. The degree of polarization is then equal to the degree of linear polarization, and is the quantity that is commonly determined experimentally

$$\pi = \pi_L = \frac{I_{\max} - I_{\min}}{I_{\max} + I_{\min}}$$

where I_{\max} and I_{\min} are the maximum and minimum intensities that are observed through a polarizer as it is rotated. The value of π_e is positive for right-handed and negative for left-handed radiation.

11.2 Optical components for polarimetry

Polarimeters can contain a number of components that are optically active in the sense that they alter the state of polarization of the radiation. They may be grouped under three headings: polarizers, converters, and depolarizers. The first produces linearly polarized light, the second converts elliptically polarized light into linearly polarized light, or vice versa, while the last eliminates polarization.

11.2.1 Birefringence

In a *birefringent material* the velocity of propagation of light will depend on the polarization of the light and it will also depend on the orientation of the light ray with respect to the structure of the material. In some materials it is possible to find a linearly polarized direction in which the light propagates at uniform velocity. This ray is termed the ordinary ray. The ray that is polarized orthogonally to the ordinary ray is termed the extraordinary ray and it propagates with differing speed depending on direction. The direction in the material in which the ordinary and extraordinary rays propagate with the same speed is called the optical axis of the material. When the velocity of the extraordinary ray is greater than the ordinary ray, then the birefringence is negative. The degree of birefringence may be obtained from the principal extraordinary refractive index μ_E . This is the refractive index corresponding to the maximum velocity of the extraordinary ray for negative materials and the minimum velocity for positive materials. It will be obtained for rays travelling perpendicularly to the optic axis of the material. The degree of birefringence is often denoted by J , and is simply the difference between the principal extraordinary refractive index for the ordinary ray, μ_O

$$J = \mu_E - \mu_O.$$

Most crystals exhibit natural birefringence, and this can be introduced into many more and into amorphous substances such as glass by the presence of strain in the material. One of the most common birefringent materials is calcite where $\mu_O = 1.658$ and $\mu_E = 1.486$.

Some crystals such as quartz that are birefringent ($J = 0.009$) are in addition *optically active* in the sense that the plane of polarization of a beam of radiation is rotated as it passes through the material. Looking down a beam of light, against the motion of the photons, a substance is called *dextro-rotatory* or right handed if the rotation of the plane of vibration is clockwise. The other case is called *laevo-rotary* or left handed.

11.2.2 Polarizers (or analysers)

These are devices that only allow the passage of light that is linearly polarized in some specified direction. There are several varieties that are based on birefringence, of which the *Nicol prism* is the best known.

Polarizing sunglasses are based upon another type of polarizer. They employ *dichroic crystals* that have nearly 100% absorption for one plane of polarization and less than 100% for the other. Generally the dichroism varies with wavelength so that these polarizers are not achromatic. Usually, however, they are sufficiently uniform in their spectral behavior to be usable over quite wide wavebands. The use of microscopic crystals and the existence of a large commercial market means that dichroic are far cheaper than birefringent polarizers, and so they may be used even when their performance is poorer than that of the birefringent polarizers.

Polarization by reflection can be used to produce a polarizer. A glass plane inclined at the *Brewster angle* (also known as the polarization angle, is an angle of incidence at which light with a particular polarization is perfectly transmitted through a surface, with no reflection) will reflect a totally polarized beam. However, only a small percentage (about 7.5% for crown glass) of the incident energy is reflected. Thus, reflection from a secondary surface will reinforce the first reflection and several plates may be stacked together to provide further reflections). The transmitted beam is only partially polarized, but as the number of plates is

increased the total intensity of the reflected beams will approach half of the incident intensity. Hence the transmitted beam will approach complete polarization.

11.2.3 Converters (retarders or phase plates)

These are devices that alter the type of polarization and/or its orientation. They are also known as retarders or phase plates. Elliptically polarized light may be resolved into two orthogonal linear components with a phase difference. Altering the phase difference will alter the degree of ellipticity. The velocities of mutually orthogonal linearly polarized light will in general differ when the beams pass through a birefringent material. When the optic axis is perpendicular to the incident radiation, the ordinary and extraordinary rays will travel in the same direction. They will recombine upon emergence, but with an altered phase delay due to their differing velocities. The phase delay, δ' , is given to first approximation by

$$\delta' = \frac{2\pi d}{\lambda} J$$

where d is the thickness of the material and J is the birefringence of the material. If we now define the x axis to be the polarization direction of the extraordinary ray, and note that δ is the intrinsic phase difference between the components of the incident radiation. Then, the ellipse for the emergent radiation has a minor axis given by

$$b' = a' \tan \left[\frac{1}{2} \sin^{-1} \left\{ \left[\frac{2e_1 e_2}{e_1^2 + e_2^2} \right] \sin(\delta + \delta') \right\} \right]$$

where the primed quantities are for the emergent beam. So

$$\begin{aligned} b' &= 0 && \text{for } \delta + \delta' = 0 \\ b' &= a && \text{for } \delta + \delta' = \sin^{-1} \left[\frac{e_1^2 + e_2^2}{2e_1 e_2} \right] \end{aligned}$$

and also

$$\psi' = \frac{1}{2} \tan^{-1} \left\{ \left[\frac{2e_1 e_2}{e_1^2 - e_2^2} \right] \cos(\delta + \delta') \right\}.$$

Thus

$$\psi' = -\psi \quad \text{for } \delta' = \pi$$

and

$$a' = a, \quad b' = b.$$

Thus we see that elliptically polarized radiation may have its degree of ellipticity altered and its inclination changed by passage through a converter. In particular it may be converted into linearly polarized or circularly polarized radiation, or its orientation may be reflected about the fast axis of the converter.

In real devices the value of δ' is chosen to be $\pi/2$ or π and the resulting converters are called *quarter-wave plates* or *half-wave plates* respectively, since one beam is delayed with respect to the other by a quarter or a half of a wavelength. The quarter wave plate is used to convert elliptically or circularly polarized light into linearly polarized light or vice versa, while the half wave plate is used to rotate the plane of linearly polarized light.

11.2.4 Depolarizers

The ideal depolarizer accepts any form of polarized radiation and produces unpolarized radiation. No such device exists, but pseudo-depolarizers can be made. These convert the polarized radiation into radiation that is unpolarized when averaged over wavelength, time, or area.

A monochromatic depolarizer can be formed from a rotating quarter-wave plate that is in line with a half-wave plate rotating at twice its rate. The emerging beam at any given instant will have some form of elliptical polarization, but this will change rapidly with time, and the output will average to zero polarization over several rotations of the plates.

The Lyot depolarizer averages over wavelength. It consists of two retarders with phase differences very much greater than 2π . The second plate has twice the thickness of the first and optic axis that is rotated by $\pi/4$ with respect to that of the first. The emergent beam will be polarized at any given wavelength, but the polarization will vary very rapidly with wavelength. In the optical, averaging over a waveband a few tens of nanometers wide is then sufficient to reduce the net polarization to one per cent of its initial value.

If a retarder is left with a rough surface and immersed in a liquid whose refractive index is the average refractive index of the retarder, then a beam of light will be undisturbed by the roughness of the surface because the hollows of will be filled by the liquid. The retarder will vary on the scale of its roughness in its effect. Thus the polarization of the emerging beam will vary on the same scale, and a suitable choice for the parameters of the system can lead to an average polarization of zero over the whole beam.

11.3 Polarimeters

A polarimeter is an instrument that measures the state of polarization or some aspect thereof, of a beam of radiation. Ideally all four Stokes parameters should be measured. Most of the time only the degree of linear polarization and its direction are found.

11.4 Spectropolarimetry

Spectropolarimetry that provides information on the variation of polarization with wavelength can be realized by several methods.

11.5 Data reduction and analysis

The output of a polarimeter is usually in the form of a series of intensity measurements for varying angles of the polarizer. These must be corrected for instrumental polarization. The atmospheric contribution to the polarization must be removed by comparison of the observations of the object and its background.

11.6 Exercises

1. Obtain the equation

$$\psi = \frac{1}{2} \tan^{-1} \left\{ \left[\frac{2e_1 e_2}{e_1^2 - e_2^2} \right] \cos \delta \right\}$$

from the equations

$$E_x(t) = e_1 \cos(2\pi\nu t)$$

and

$$E_y(t) = e_2 \cos(2\pi\nu t + \delta)$$

(This is exercise 5.2.1 from Kitchin's *Astrophysical Techniques*.)

2. Show, using the Mueller calculus, that the effect of two ideal half-wave plates upon a beam of radiation of any form of polarization is zero. The Mueller matrix for the half wave plate is given by

$$\mathbf{M} = \begin{bmatrix} 1 & 0 & 0 & 0 \\ 0 & \cos^2 2\psi - \sin^2 2\psi & 2 \cos 2\psi \sin 2\psi & 0 \\ 0 & 2 \cos 2\psi \sin 2\psi & \sin^2 2\psi - \cos^2 2\psi & 0 \\ 0 & 0 & 0 & -1 \end{bmatrix}$$

(This is exercise 5.2.2 from Kitchin's *Astrophysical Techniques*.)

3. A Lyot filter is built up of several elements which each consist of a crystal of birefringent material such as quartz and a polarizer. The optical axis of the crystal is oriented such that the ordinary and extraordinary rays propagate in the same direction. The electric vector of the light that comes out of such an element can be written

$$E_{45} = \frac{a}{\sqrt{2}} [\cos(2\pi\nu t) + \cos(2\pi\nu t + \delta)] \quad (11.1)$$

The degree of birefringence is $J = \mu_e - \mu_o$, where μ_e and μ_o are the indices of refraction for the extraordinary 'e' and ordinary 'o' rays respectively.

- (a) Show that the difference in phase between the two rays

$$\delta = \frac{2\pi c \Delta t}{\lambda} \quad (11.2)$$

where c is the speed of light in vacuum, λ is the wavelength and Δt is the time delay, can be written

$$\delta = \frac{2\pi T J}{\lambda} \quad (11.3)$$

where T is the thickness of the material.

- (b) Find the wavelengths λ_{\max} and λ_{\min} where the emerging ray has maximum and minimum intensity.
- (c) Sketch what the emergent intensity from this element looks like a function of wavelength and explain how and why one need several elements in order to construct a Lyot filter.
4. Calculate the maximum and minimum thickness of the elements required for an H α birefringent filter based upon calcite, if its whole bandwidth is to be 0.05 nm, and it is to be used in conjunction with an interference filter whose whole bandwidth is 3 nm. The birefringence of calcite is -0.172 . (This is exercise 5.3.1 of Kitchin's *Astrophysical Techniques*.)

Chapter 12

Photometry

The brightness of stars has, along with their locations, been studied by astronomers since ancient times. Prior to the 1860's observers necessarily estimated brightness using their eyes expressing the result in the *magnitude system* that Ptolemy introduced in the second century.

12.1 A short history

Modern instruments show that early measurements such as those made by Ptolemy and Tycho Brahe (who were both more interested in the position of objects) have an internal precision of about 0.5^m. Even a very skilled observer can do little better; al Sufi in the ninth century spent great effort on this problem and achieved a precision of some 0.4^m. With a telescope several observers, such as the Herschels, were able to produce results of 0.1 – 0.3^m by using comparisons with known *sequences* of standard brightness stars.

Francois Arago suggested an optical/mechanical system by which adjusts the brightness of a comparison star until it matches the unknown star or dims the telescopic brightness of a star until it disappears. These systems are called *visual photometers*. Between 1879 and 1902 Harvard visual photometrists had measured the magnitudes of some 47 000 stars with a precision of about 0.08^m and an accuracy of better than 0.25^m. At this time in history (1900) the Pogson normal scale

$$\Delta m = -2.5 \log(b_1/b_2)$$

where b_1 and b_2 are the brightness of objects 1 and 2 was standard amongst all astronomers.

In the same period photography progressed and astronomers were able to record the light of stars too faint to be seen by eye in any telescope. An international collaboration, the *Carte du Ciel* project, was started with the goal of photographing the entire sky and measuring the brightness of every star below 11.0^m. However, photographic plates do not measure light linearly and it took several years, until 1900–1910, before a reliable *photographic magnitude* system was established. The introduction of physical photometers in the period 1910–1920 to objectively measure images on photographic plates eventually led to magnitudes being measured with uncertainties in the range 0.015 – 0.03^m.

Experiments with photoelectric work began in the early part of the 20th century and in the 1930's with the introduction of vacuum-tube amplifiers detection limits on a 0.5 m telescope improved from 11.0^m to 13.0^m. Photomultiplier tubes, introduced during World War II, improved the situation greatly and quickly became the instrument of choice for measuring brightness, with uncertainties of 0.005^m in relative brightness. During the 1950 period to

1980 the RCA 1P21 photomultipliers were used by Harold Johnson to define the UBV system, which later was extended by the use of red sensitive photomultipliers into the infrared.

At present CCDs and other modern solid-state detectors have mostly superseded photomultipliers. In the optical CCDs have superior efficiency, better stability, and a large multiplex advantage.

From space, for example the Kepler mission for detecting occultations by extrasolar planets, achieves uncertainties below $10 \mu\text{m}$ over time scales of several weeks.

12.2 The response function

A photometric device is sensitive over a restricted range of wavelengths called a bandpass. There are three types of bandpass photometry in astronomy.

12.2.1 Types of photometry

Single-band photometry

For applications such as finding planets via occultations where one is only interested in measuring the fraction of light from the star blocked by a planet one needs only a single band. In this case one would generally want to construct a sequence of observations into a time series, *i.e.* a tabulation of brightness as a function of time, choosing a wide band to maximize signal and minimize the required exposure time and telescope size. An example of this is the Super Wasp telescope arrays placed on La Palma and in South Africa.

Broadband multi-color photometry

Broadband multi-color photometry measures a very low resolution spectrum by sampling the brightness in several different bands. Broad band in this sense means that the spectroscopic resolving power $R = \lambda_c/\Delta\lambda < 10 - 15$. These systems attempt to choose bands that admit the maximum amount of light while still providing astrophysical information. The most typical example of such a system is the optical *UBVRI* system which uses bandwidths in the range $65 - 160 \text{ nm}$ ($R = 4 - 7$). This system can provide information on surface temperature, as well as (more limited) information on luminosity, metal content, and interstellar reddening for a wide variety of stars.

Each band in a system such as this is known as a *color*, so “two-color photometry” measures magnitudes in two separate bands. Usually one reports the results of n -color photometric measurements by giving one magnitude and $(n - 1)$ color indices. The magnitude tells the apparent brightness, and the indices tell about other astrophysical variables such as the surface temperature. Color can also have a second meaning: the difference between two magnitudes. For example, the results of two-color photometry in B and V will be reported as a V magnitude and *one* ($B - V$) color.

Narrow and intermediate-band photometry

The intent of narrow band photometry ($R > 50$) is usually to isolate a specific line, molecular band, or other spectral feature. Common applications include the measurement of the strength of absorption features like Balmer- α or sodium D, or the ratio of the intensities of emission lines in gaseous nebulae. Intermediate-band photometry ($15 < R < 50$) measures

spectroscopic features that cannot be resolved by broad bands but avoids the severe light loss of narrow-band photometry. Examples of such features include discontinuities in spectra, such as the Balmer discontinuity at 364.6 nm or very broad absorption features due to blended lines or molecular bands such as the band due to TiO in the spectra of M stars extending from 705 to 730 nm.

12.3 Magnitudes

We can write the *apparent magnitude* of the source as

$$m_P = -2.5 \log (F_P) + C_P = -2.5 \log \int_0^\infty R_P(\lambda) f_\lambda d\lambda + C_P.$$

Where m_P is the bandpass magnitude, F_P is the energy flux (irradiance) within the band, f_λ is the monochromatic flux. The constant C_P is chosen to conform to some standard scale (*e.g.* the magnitude of Vega is zero in the visual system). The function $R_P(\lambda)$ is called the *response function* of the entire observing system to the incident flux, it is the fraction of the energy of wavelength λ that will register on the photometer.

Note that photometers count photons and therefore do not measure the energy directly. Thus we write the *monochromatic photon flux*

$$\phi(\lambda) = \frac{\lambda}{hc} f_\lambda$$

and the quantity measured by photon detectors is the *photon flux within the band*

$$\Phi_P = \int_0^\infty R_{PP}(\lambda) \phi(\lambda) d\lambda = \frac{1}{hc} \int_0^\infty R_P f_\lambda d\lambda$$

where R_{PP} is the *photon response*: the fraction of photons of wavelength λ detected by the system. It is also possible to define the *monochromatic magnitude* defined from the monochromatic flux:

$$m_\lambda = -2.5 \log (f_\lambda) + C'(\lambda) = -2.5 \log \frac{hc\phi(\lambda)}{\lambda} + C'(\lambda)$$

$C'(\lambda)$ is arbitrary, and is often chosen so that the monochromatic magnitude of Vega or some other standard is a constant at every wavelength. In which case $C'(\lambda)$ is a strong function of λ . On the other hand $C'(\lambda)$ can also be chosen as a constant function and at the monochromatic magnitude reflects the spectrum in energy units.

12.3.1 Response function implementation

Both practical limits and intentional controls can determine the functional form of the response functions R_P and R_{PP} . The *sensitivity of the detector* limits the wavelength accessible. In some cases detector response alone sets the bandpass, in other cases the detector response defines only one edge of a given band.

A *filter* is the usual method for intentionally delimiting the band by blocking all wavelengths except for those in a specific range. Filters can also serve as *high-pass* or *low-pass* elements to only defining the lower or upper cutoff of a band.

It is also possible to use a dispersing element to create a spectrum and then sampling discrete segments of the spectrum with one or more photometers. Such instruments are called *spectrophotometers*. These generally define bandpasses by using apertures, slots, or detectors of the proper size to select the desired segment of the spectrum.

For ground based observations *atmospheric transmission*, $S_{\text{atm}}(\lambda)$, limits the wavelength that are accessible, and may define all or parts of a response function.

Normally magnitudes are defined outside the Earth's atmosphere, and astronomers must remove atmospheric effects during data reduction.¹

12.3.2 Response function description

There are a whole host of terms used to describe the response function $R(\lambda)$.

There is a single maximum value R_{\max} which occurs at the *peak wavelength* λ_{peak} . There are also two half-maximum points, often taken as specification of where the transmission band begin and ends, λ_{low} and λ_{high}

$$\begin{aligned} R(\lambda_{\text{peak}}) &= R_{\max} \\ R(\lambda_{\text{low}}) = R(\lambda_{\text{high}}) &= R_{\max}/2 \end{aligned}$$

Given the maxima, the width of the response can be characterized by the *full width half maximum*

$$\text{FWHM} = \lambda_{\text{high}} - \lambda_{\text{low}},$$

which in turn determines the *central wavelength* of the band

$$\lambda_{\text{cen}} = (\lambda_{\text{low}} + \lambda_{\text{high}})/2$$

A perhaps more useful measure of the width of $R(\lambda)$ is provided by the *bandwidth*

$$W_0 = \frac{1}{R_{\max}} \int R(\lambda) d\lambda$$

which in turn suggest the definition of the *mean wavelength*

$$\lambda_0 = \frac{\int \lambda R(\lambda) d\lambda}{\int R(\lambda) d\lambda}$$

For a symmetric $R(\lambda)$ we have

$$\lambda_{\text{peak}} = \lambda_{\text{cen}} = \lambda_0$$

Quite informative is the *effective wavelength* of the response $R(\lambda)$ to a particular source. This is the weighted mean wavelength and indicates which photons influence a particular measurement:

$$\lambda_0 = \frac{\int f_\lambda \lambda R(\lambda) d\lambda}{\int f_\lambda R(\lambda) d\lambda}$$

A bandpass measurement is nearly equivalent to a measurement of the monochromatic flux at the wavelength λ_{eff} multiplied by the bandwidth W_0 . Which is nearly correct in practice, and for broadband photometry of stars with sufficiently smoothed spectra using this equivalence only gives errors on the order of a few percent or less. But, to be strictly accurate

¹See Exercise 3.

with such an equivalence, another definition must be made of the middle of the band: the *isophotal wavelength* given by

$$W_0 f_{\text{iph}} = \frac{1}{R_{\max}} \int f_\lambda R(\lambda) d\lambda$$

As for the effective wavelength the exact value of the isophotal wavelength will depend on the spectrum of the source.

12.3.3 Color indices

Multi band photometry can measure the shape of an object's spectrum. It is convenient to think of the bands as sampling the monochromatic flux of a smoothed spectrum at their isophotal wavelength. Figure 12.1 shows several blackbodies whose temperatures range from 1600 K to 16 000 K. The vertical scale of the figure shows the monochromatic magnitude in a system in which the constant C is set to be a constant independent of temperature. Remember that this is not usually the case in astronomical photometry, where the spectrum of some standard object (*e.g.* Vega, which is similar to a blackbody of temperature 9500 K) would be a horizontal line in a plot of m_λ as a function of λ .

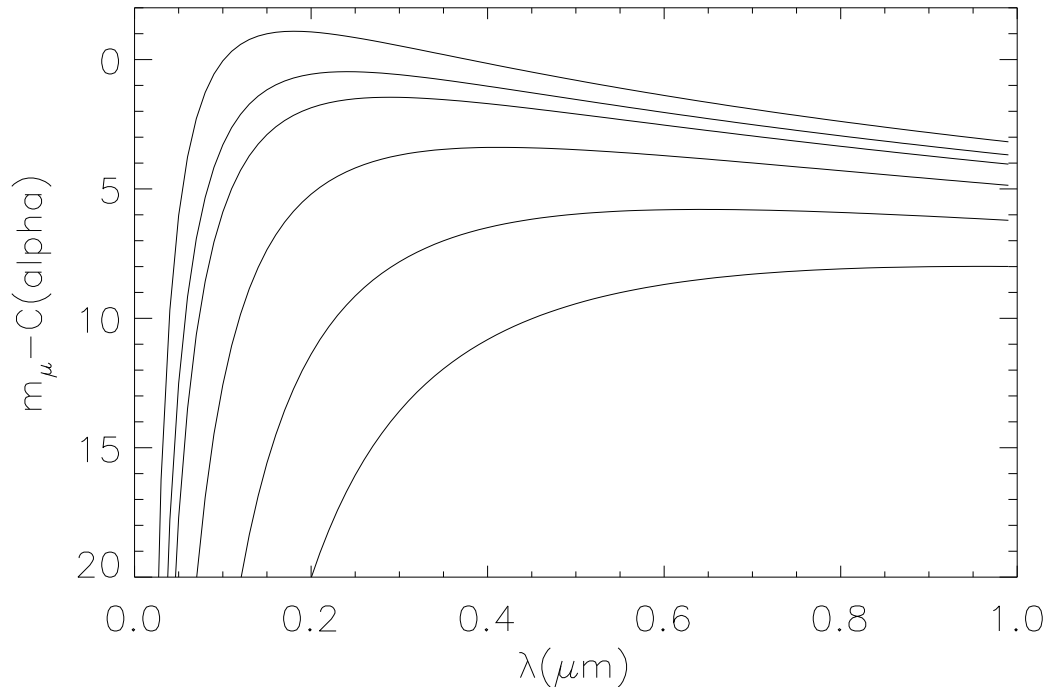


Figure 12.1: Blackbody curves for stars of temperature between 1600 K to 16 000 K. $C(\alpha)$ is set arbitrarily to $C(\alpha) = -15$.

For two (broad) bands centered at $0.4\text{ }\mu\text{m}$ and at $0.8\text{ }\mu\text{m}$ is clear that the arithmetical difference between these two magnitudes for a particular spectrum depends on the average slope of the spectrum, which in turn depends on the source's temperature. The convention

is to speak of the difference between any two bandpass magnitudes used to sample the slope of the spectrum as a *color index*. By convention one computes the index in the sense

$$\text{index} = m(\text{shorter } \lambda) - m(\text{longer } \lambda)$$

The behavior of the color index at the long and short wavelength extremes of the Planck function are informative. In the Rayleigh-Jeans region (where $\lambda kT \gg hc$) we have

$$m_\lambda = \log T + C(\lambda)$$

so the color index is

$$(m_{\lambda_1} - m_{\lambda_2}) = C(\lambda_1) - C(\lambda_2) = \Delta C \quad (12.1)$$

which is a constant independent of temperature. At short wavelengths the *Wien approximation* applies and the surface brightness can be given by

$$B(\lambda, T) \approx \frac{2hc^2}{\lambda^5} \exp\left(-\frac{hc}{\lambda kT}\right).$$

The color index is then

$$(m_{\lambda_1} - m_{\lambda_2}) = \frac{a}{T} \left(\frac{1}{\lambda_1} - \frac{1}{\lambda_2} \right) + C(\lambda_1) - C(\lambda_2) \quad (12.2)$$

Thus, at very low temperature or short wavelengths the index is a linear function of $1/T$.

12.3.4 Line and feature index

Real objects such as stars will of course have more complex spectra than blackbodies with features of astrophysical significance such as absorption and emission lines, bands, and various discontinuities. Multi-band photometry can measure the strength of such features.

Two bands are often sufficient to measure the size of a discontinuity or the strength of a line.

The positioning of bands is important. The sensitivity of the index to the size of the break will diminish if either the bandpass response includes light from the opposite side of the break. Likewise, if a band is located too far away from the break, unrelated features can affect the index.

An alternative way of characterizing a line is to use two bands — one broad, one narrow — both centered on the line in question. While the broad band is relatively insensitive, the narrow band is quite sensitive. The index

$$\text{line index} = m_{\text{narrow}} - m_{\text{wide}}$$

tracks the strength of the absorption, in the sense that it becomes more positive with stronger absorption. One widely used index of this sort is the β index, which measures the strength of the Balmer beta line of hydrogen, usually useful for luminosity or temperature classification of stars.

Finally, note that three bands can be used to measure the *curvature* or second derivative of a spectrum. Curvature can arise on relatively short scale because of sharp absorption or emission lines, or on long scales because of broad or diffuse features such as molecular bands. A curvature index is defined by the differences

$$\text{curvature} = (m_S - m_C) - (m_C - m_L)$$

where S , C and L indicate the short, central, and long wavelength bands respectively.

12.4 Photometric systems

Photometric systems are defined by at least two specifications:

1. The wavelength response of each band — that is, the shape of $R_P(\lambda)$.
2. Some method for standardizing measurements made in those bands.
 - Each observer needs to know the value of the constant C that will assure agreement of his magnitudes with those of all other observers.
 - The different hardware produces some variety in the response functions in practice, so a method for standardization must allow correction of the inevitable systematic effects due to imperfect matching.

The first specification, $R_P(\lambda)$, determines the *instrumental* or *natural system*. The first and second together determine the *standard system*.

Almost all standard systems rely on some network of constant-brightness standard objects distributed around the sky. It is important to define a set of standards that include a wide variety of spectral types.

A *closed photometric system* is one in which a small group of observers carefully controls the instruments and data reduction, maximizing the internal consistency. Examples include the space borne HIPPARCOS data and the Sloane Digital Sky Survey. An *open photometric system* is one in which all astronomers are encouraged to duplicate the defined natural system as best they can, and through references to a published list of standard stars add to the pool of observations in the system.

12.4.1 Common photometric systems

Visual and photographic systems

The dark-adapted human eye determines the band of the *visual photometric system*. The introduction of optical/mechanical visual photometers led to the establishment of *standard sequences* of stars, including initially the *north polar sequence* and later many secondary sequences: amongst them importantly the 48 Harvard standard regions and the 115 Kapteyn selected areas.

In the early twentieth century, astronomers defined two bands based on the properties of photographic emulsion. The poor properties of emulsion as a photometric detector, and lack of very specific definitions, limited the success of this system. The *international photographic system* is sensitive in the near ultraviolet-blue region. The response of the *international photographic photovisual band* roughly corresponds to that of the visual band (*i.e.* the human eye, sensitive to green-yellow). The IAU in 1922 set the zero point of both magnitudes so that the 6^m magnitude A0 V stars in the north polar sequence would have (roughly) the same values as on the old Harvard visual system.

The *UBVRI* system

The most widely used photometric system prior to the present has been the Johnson-Cousins *UBVRI* system. This system was originally based on the RCA 1P21 photomultiplier, a set of colored glass filters, and a list of magnitudes for a relatively small number of stars scattered

on the celestial sphere. The V band is very close to the international photovisual band and its zero point was set so that $V = mpv$ for standards in the north polar sequence. The U and B correspond to the short- and long-wavelength bands of the photographic band, and their zero points are set so that the colors $U - B$ and $B - V$ are zero for A0 V stars.

In the period 1960–1965 the system was extended to include bands in the red R_J and near infrared I_J , as well as the longer wavelength bands ($JHKLMNQ$) discussed below. Modern work with CCDs has tended to replace the original R_J and I_J with the R_C and I_C bands.

This multi band system was designed with the rough spectral classification of stars in mind. The $U - B$ index is sensitive to the Balmer discontinuity (very obvious in A stars at 370 nm, much reduced for G stars). The discontinuity depends on luminosity for hot stars. The other indices are primarily sensitive to temperature. The $B - V$ index is more sensitive to metal abundance than $V - R$ or $R - I$. The $V - I$ index is the most purely temperature sensitive index in this system.

The broadband infrared system: $JHKLMNQ$

This broadband system might be regarded as an extension of the $UBVRI$ system, it shares a common zero point so that the colors of an unreddened A0 V star are zero. Detectors in this region cannot be silicon CCDs but must be infrared arrays or single-channel infrared devices.

A large complication for these bands for ground based observations bandpass definitions can depend critically on atmospheric conditions (due to water vapor along the line of sight). Different observatories with identical hardware can experience different infrared window sizes and shapes if they are at different altitudes. The same observatory can experience similar bandpass variations due to changing humidity.

The IAU in 2000 recommended a preferred natural system — the Mauna Kea Observatory near-infrared system (MKO).

The intermediate band Strömgren system: $uvby\beta$

Bengt Strömgren designed this intermediate-band system in the late 1950s. The system avoids many of the shortcomings of the UBV system and aims to classify stars according to three characteristics: temperature, luminosity, and metal abundance. This works well for stars of spectral types B, A, F, and G provided the photometry is sufficiently accurate. The four intermediate band colors $uvby$ are supplemented with a narrow band β index which tracks the strength of the Balmer beta line. This greatly improves the luminosity classification for hotter stars, and is a good temperature indicator for cooler stars.

Emission in the u and v bands is depressed by the presence of metals in a star's atmosphere. Also the u band is depressed by the Balmer discontinuity.

12.5 From source to telescope

At least four different effects can alter the photons on their way to the telescope:

- Wavelength shifts
- Extragalactic absorption
- Galactic and Solar System absorption

- Atmospheric absorption

12.5.1 Wavelength shifts

The photons that leave the source is written $\phi_E(\lambda_E d\lambda_E)$, where the subscript ‘E’ stands for “emitted”.

Because of the Doppler effect, or because of the expansion of the Universe, or because of other relativistic effects, the wavelength of the observed photon will differ from its original value. The new value is given by

$$\lambda_o = (1 + z)\lambda_E$$

where z is the redshift parameter $z = (\lambda_o - \lambda_E)/\lambda_E$ of the source. The number of photons is conserved in these processes so

$$\phi(\lambda)d\lambda = \phi_E(\lambda_E d\lambda_E)$$

Thus, the observed and emitted monochromatic photon flux are related by

$$\phi(\lambda) = \frac{1}{1+z}\phi_E\left(\frac{\lambda}{1+z}\right) = f_\lambda \frac{\lambda}{hc}$$

and the monochromatic flux density is then

$$f_E(\lambda_E) = f_E\left(\frac{\lambda}{1+z}\right) = \frac{hc\phi_E(\lambda_E)}{\lambda_E} = (1+z)^2 f_\lambda$$

Note that the monochromatic flux density is *not* conserved.

An observer who uses a bandpass with photon response $R(\lambda)$ will measure the magnitude

$$\begin{aligned} m_R &= -2.5 \log \int R(\lambda) \frac{\phi(\lambda)}{\lambda} d\lambda + C_R \\ C_R &= -2.5 \log \int R(\lambda) \frac{g_\lambda}{hc} d\lambda \end{aligned}$$

where g_λ is the spectrum of a photometric standard magnitude zero. We need to find how m_R relates to a magnitude measured for these same photons before their wavelength shift. Call the unshifted band the photons began their journey in Q , different from R .

$$\begin{aligned} m_Q &= -2.5 \log \int Q(\lambda) \frac{\phi_E(\lambda)}{\lambda} d\lambda + C_Q \\ &= -2.5 \log \left[(1+z) \int Q(\lambda) \frac{\phi(\lambda(1+z))}{\lambda} d\lambda \right] + C_Q \\ C_Q &= -2.5 \log \int Q(\lambda) \frac{g_\lambda}{hc} d\lambda \end{aligned}$$

We must consider the difference

$$m_R - m_Q = 2.5 \log(1+z) + C_R - C_Q + 2.5 \log \left[\frac{\int Q(\lambda) \frac{\phi(\lambda(1+z))}{\lambda} d\lambda}{\int R(\lambda) \frac{\phi(\lambda)}{\lambda} d\lambda} \right]$$

For objects in our galaxy, z is small, and one can use $R(\lambda) = Q(\lambda)$, $C_R = C_Q$, in which case the first three terms add up to zero. The last term describes the effect of photons shifting

into and out of the band. In the case of narrow bands near sharp spectral features, even small Doppler shifts can produce large differences between $\phi((1+z)\lambda)$ and $\phi(\lambda)$.

For distant objects z becomes large because of the expansion of the Universe. Given knowledge of $\phi(\lambda)$ and z it is possible to use an observed bandpass magnitude to compute the magnitude that would be observed if the source had a redshift $z = 0$. Hubble called this kind of correction the *K correction*.

12.5.2 Absorption outside the atmosphere

Interstellar gas and dust absorb and scatter light. It is common to refer to both processes as “absorption”. Absorption not only reduces the number of photons arriving at the telescope, *extinction*, but also alters the shape of the spectrum.

Diffuse gas absorbs photons to produce *interstellar absorption lines and bands*. In the optical sodium D is usually the strongest interstellar line, in the UV the Lyman-alpha line is usually strongest. At short wavelengths gas will also produce continuous absorption and absorption edges due to ionization *e.g.* at 91.2 nm due to the Lyman continuum. Absorption by dust will generally alter the overall shape of the spectrum. In the region $0.22 - 5.0 \mu\text{m}$, dust scatters short wavelength photons more than long wavelength photons, so the resulting change in shape of the spectrum is called *interstellar reddening*.

Now define $S_{\text{ism}}(\lambda)$ as the fraction of photons of wavelength λ that are transmitted by the interstellar medium within our galaxy and $S_{\text{exg}}(\lambda)$ as the fraction of photons arriving at λ that are transmitted by the interstellar medium outside our galaxy. Note that because of cosmological redshift, absorption described by $S_{\text{exg}}(\lambda)$ involve photons that had wavelength $\lambda/(1+z')$ when they were absorbed by material with redshift parameter z' . (This produces the phenomenon of the *Lyman-alpha forest* in the spectra of distant objects: multiple absorption lines due to Ly α at multiple red-shifts.) The photon flux that reaches the top of the Earth’s atmosphere is

$$\phi(\lambda) = S_{\text{ism}}(\lambda)S_{\text{exg}}(\lambda)\phi_0(\lambda) = S_{\text{ism}}(\lambda)S_{\text{exg}}(\lambda)\frac{1}{1+z}\phi_E((1+z)\lambda) = f_\lambda \frac{\lambda}{hc}$$

where $\phi(\lambda)$ is the photon flux outside the atmosphere and $\phi_0(\lambda)$ is the photon flux outside the atmosphere corrected for interstellar absorption.

12.5.3 Absorption by the atmosphere

Extinction in the Earth’s atmosphere is a strong function of wavelength. At sea level, three opaque regions define two transmitting windows. Rayleigh scattering and absorption by atoms and molecules cause a complete loss of transparency at all wavelengths shorter than about 300 nm. This sets the short end of the *optical infrared window*. The second opaque region, from absorption in molecular bands — primarily due to H_2O and CO_2 — begins at roughly $0.94 \mu\text{m}$, has a few breaks in the infrared and mid infrared, and extends from 30 mm to the start of the *microwave radio window* at around 0.6 cm. The radio window ends at around 20 m because of ionospheric absorption and reflection.

Qualitatively we can set up an atmospheric transmission function $S_{\text{atm}}(\lambda, t, e, a)$ as the fraction of photons of wavelength λ that are transmitted by the Earth’s atmosphere at time t , elevation angle e and azimuth a . The photon flux that reaches the telescope is then

$$\phi_A(\lambda) = S_{\text{atm}}(\lambda, t, e, a)S_{\text{ism}}(\lambda)S_{\text{exg}}(\lambda)\frac{1}{1+z}\phi_E((1+z)\lambda) = f_\lambda^A \frac{\lambda}{hc}$$

and the rate at which energy gets detected in an infinitesimal band is

$$dE_{\text{sig}} = aT'_P(\lambda)f_\lambda^A d\lambda = aT'_P(\lambda)\frac{\phi_A(\lambda)}{\lambda}d\lambda$$

Where a here is the effective collecting area of the telescope, and $T'_P(\lambda)$ is a function of the overall wavelength dependent efficiency of the instrument. Integrating this equation gives us the *instrumental magnitude*

$$\begin{aligned} m_P^A &= -2.5 \log \int T'_P S_{\text{atm}}(\lambda) \frac{\phi(\lambda)}{\lambda} d\lambda + C'_P \\ &= m_P^O + A_{\text{atm}} + A_{\text{ism}} + A_{\text{exg}} + C_P^z \\ &= m_P + A_{\text{atm}} \end{aligned}$$

Here the A parameters represent the atmospheric, Galactic, and extragalactic absorption, in magnitudes; C_P^z is the correction for wavelength shift; and C'_P is the constant that sets the zero point of the instrumental magnitude scale. The quantity m_P , the *instrumental magnitude outside the atmosphere*, depends on the telescope and photometer but is independent of the atmosphere. The quantity m_P^O is the instrumental magnitude in the emitted frame corrected for all absorption effects. m_P can be written as

$$m_P = -2.5 \log \int T_P \frac{\phi(\lambda)}{\lambda} d\lambda + C_P$$

where $T_P(\lambda)$ and C_P characterize the instrumental system located outside the atmosphere.

12.6 Exercises

1. The faintest stars visible to the naked eye, from the definition of the scale, are magnitude six. For point sources the brightness is increased by the use of a telescope by a factor G , called the light grasp. If the dark adapted human eye has a diameter of 7 mm, show that

$$G \approx 2 \times 10^4 d^2$$

where d is the telescope diameter in meters. Show further that the limiting magnitude through a visually used telescope, m_L is

$$m_L = 16.8 + 5 \log d.$$

2. Find a plot of the Earth's atmospheric transmission as a function of wavelength λ .
3. Give reasons as to why it is better to define the response function $R(\lambda)$ *outside* the Earth's atmosphere. What are the advantages and disadvantages of doing this?
4. Reproduce figure 12.1 using *e.g* IDL.
5. Show that equations 12.1 and 12.2 are correct.